Autophagy

Volume 11 - Issue 11 - November 2015

Editor-in-Chief
Daniel J. Klionsky
University of Michigan

Taylor & Francis
Taylor & Francis Group

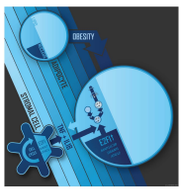

Autophagy

ISSN: 1554-8627 (Print) 1554-8635 (Online) Journal homepage: http://www.tandfonline.com/loi/kaup20

Developmentally regulated autophagy is required for eye formation in *Drosophila*

Viktor Billes, Tibor Kovács, Anna Manzéger, Péter Lőrincz, Sára Szincsák, Ágnes Regős, Péter István Kulcsár, Tamás Korcsmáros, Tamás Lukácsovich, Gyula Hoffmann, Miklós Erdélyi, József Mihály, Krisztina Takács-Vellai, Miklós Sass & Tibor Vellai

To cite this article: Viktor Billes, Tibor Kovács, Anna Manzéger, Péter Lőrincz, Sára Szincsák, Ágnes Regős, Péter István Kulcsár, Tamás Korcsmáros, Tamás Lukácsovich, Gyula Hoffmann, Miklós Erdélyi, József Mihály, Krisztina Takács-Vellai, Miklós Sass & Tibor Vellai (2018): Developmentally regulated autophagy is required for eye formation in *Drosophila*, Autophagy, DOI: 10.1080/15548627.2018.1454569

To link to this article: https://doi.org/10.1080/15548627.2018.1454569

Publisher: Taylor & Francis & Taylor and Francis Group, LLC

Journal: *Autophagy*

DOI: 10.1080/15548627.2018.1454569

Developmentally regulated autophagy is required for eye formation in *Drosophila*

Viktor Billes[1,*], Tibor Kovács[1,*], Anna Manzéger[1], Péter Lőrincz[2], Sára Szincsák[1], Ágnes Regős[1], Péter István Kulcsár[3], Tamás Korcsmáros[1,4,5], Tamás Lukácsovich[6], Gyula Hoffmann[7], Miklós Erdélyi[8], József Mihály[8], Krisztina Takács-Vellai[9], Miklós Sass[2,#], Tibor Vellai[1,#]

[1]Department of Genetics and [2]Department of Anatomy, Cell and Developmental Biology, Eötvös Loránd University, Budapest, Hungary; [3]Institute of Enzymology, Research Centre for Natural Sciences of the Hungarian Academy of Sciences, Budapest, Hungary; [4]Earlham Institute, Norwich Research Park, Norwich, UK; [5]Gut Health and Food Safety Programme, Institute of Food Research, Norwich Research Park, Norwich, UK; [6]Department of Developmental and Cell Biology; University of California, Irvine, CA, USA; [7]Department of Anatomy and Developmental Biology, University of Pécs, Pécs, Hungary; [8]Institute of Genetics, Biological Research Centre, Szeged, Hungary; [9]Department of Biological Anthropology, Eötvös Loránd University, Budapest, Hungary

*These authors contributed equally to the work.

[#]Corresponding authors: T.V. (vellai@falco.elte.hu) or M.S. (msass@elte.hu)

Address: Department of Genetics, Eötvös Loránd University, Budapest, Pázmány Péter stny. 1/C, Hungary, H-1117; Tel.: +36-1-372-2500 Ext: 8684; Fax: +36-1-372-2641; E-mail: vellai@falco.elte.hu

Competing financial interest: The authors declare no competing financial interest.

Author contribution: V.B., T.Kov., A.M., P.L., S.Sz., Á.R., P.I.K., T.L., G.H., M.E., J.M., K.T-V., T.V., and M.S. performed experiments; V.B., T.Kov., A.M., M.E., T.Kor., J.M., K.T-V., T.V., and M.S. designed experiments and analyzed data; V.B., T.Kov., A.M., J.M., K.T-V., T.V. and M.S. wrote the manuscript.

Key words: autophagy, cell death, differentiation, *Drosophila*, eye development, genetic compensation, HOX, *labial*, pattern formation, transcriptional control

Abbreviations: αTub84B, α-Tubulin at 84B; *Act5C*, *Actin5C*; AO, acridine orange; Atg, autophagy-related; Ato, Atonal; CASP3, caspase 3; Dcr-2; Dicer-2; Dfd, Deformed; DZ, differentiation zone; eGFP, enhanced green fluorescent protein; EM, electron microscopy; *exd*, *extradenticle*; *ey*, *eyeless*; FLP, flippase recombinase; FRT, FLP recognition target; *Gal4*, gene encoding the yeast transcription activator protein GAL4; GFP, green fluorescent protein; GMR, Glass multimer reporter; Hox, homeobox; *hth*, *homothorax*; *lab*, *labial*; L3F, L3 feeding larval stage; L3W, L3 wandering larval stage; lf, loss-of-function; MAP1LC3,

microtubule-associated protein 1 light chain 3; MF, morphogenetic furrow; PE, phosphatidylethanolamine; PBS, phosphate-buffered saline; PI3K/PtdIns3K, class III phosphatidylinositol 3-kinase; PZ, proliferation zone; Ref(2)P, refractory to sigma P, RFP, red fluorescent protein; RNAi, RNA interference; RpL32, Ribosomal protein L32; RT-PCR, reverse transcription-coupled polymerase chain reaction; S.D., standard deviation; SQSTM1, Sequestosome-1, Tor, Target of rapamycin; TUNEL, terminal deoxynucleotidyl transferase mediated dUTP nick end labeling assay; UAS, upstream activation sequence; qPCR, quantitative real-time polymerase chain reaction; *w*, *white*

The number of words in the abstract: 226

The number of Figures: 10 (multipanel, colored)

Supplementary Materials contain Genotype list, Suppl. Tables (S1, S2), and Suppl. Figures and Figure Legends (S1 to S31).

Abstract

The compound eye of the fruit fly *Drosophila melanogaster* is one of the most intensively studied and best understood model organs in the field of developmental genetics. Herein we demonstrate that autophagy, an evolutionarily conserved selfdegradation process of eukaryotic cells, is essential for eye development in this organism. Autophagic structures accumulate in a specific pattern in the developing eye disc, predominantly in the morphogenetic furrow (MF) and differentiation zone. Silencing of several autophagy genes (*Atg*) in the eye primordium severely affects the morphology of the adult eye through triggering ectopic cell death. In *Atg* mutant genetic backgrounds however genetic compensatory mechanisms largely rescue autophagic activity in, and thereby normal morphogenesis of, this organ. We also show that in the eye disc the expression of a key autophagy gene, *Atg8a*, is controlled in a complex manner by the anterior Hox paralog lab (labial), a master regulator of early development. *Atg8a* transcription is repressed in front of, while activated along, the MF by lab. The amount of autophagic structures then remains elevated behind the moving MF. These results indicate that eye development in *Drosophila* depends on the cell death-suppressing and differentiating effects of the autophagic process. This novel, developmentally regulated function of autophagy in the morphogenesis of the compound eye may shed light on a more fundamental role for cellular self-digestion in differentiation and organ formation than previously thought.

Introduction

Autophagy (cellular "self-eating") is a lysosome-mediated self-degradation process of eukaryotic cells. As a main route of eliminating superfluous and damaged cytoplasmic constituents and ensuring macromolecule turnover, autophagy is required for maintaining cellular homeostasis. It also provides energy for the survival of cells under starvation. Although autophagy primarily functions as a prosurvival mechanism in terminally differentiated cells, under certain physiological and pathological settings it can also promote cell death [1-3]. In mammals, defects in autophagy can lead to accelerated aging and the development of various age-dependent pathologies including neurodegenerative diseases, cancer, diabetes, tissue atrophy and fibrosis, immune deficiency, compromised lipid metabolism, and infection by intracellular microbes [4-10].

During autophagy, parts of the cytoplasm are delivered into the lysosomal compartment for degradation by acidic hydrolases. Depending on the mechanism of delivery, 3 major types of autophagy can be distinguished: macroautophagy, microautophagy and chaperone-mediated autophagy. Macroautophagy (hereafter referred to as autophagy) involves the formation of a double membrane-bound compartment called the phagophore that sequesters the cytoplasmic material destined for degradation. The phagophore matures into an autophagosome, which then fuses with a lysosome, thereby generating a structure called autolysosome where degradation takes place [11-14].

The core mechanism of autophagy involves more than 30 autophagy-related (Atg) proteins, which are evolutionarily conserved from yeast to mammals [15]. Atg proteins are organized into functionally distinct complexes: i) the Atg1 kinase complex for inducing phagophore formation; ii) a class III phosphatidylinositol 3-kinase (PtdIns3K/Vps34) complex for vesicle nucleation; iii) a ubiquitin-like conjugation system for vesicle expansion; and iv) a

recycling complex for recovering utility materials. The ubiquitin-like conjugation system mediates the transient conjugation of Atg8 (whose mammalian orthologs include the MAP1LC3/microtubule-associated protein 1 light chain 3 and the GABARAP/GABA typeA receptor-associated protein families) to a phagophore membrane component, phosphatidylethanolamine (PE).

To date, 2 major developmental functions of autophagy have been uncovered [16,17]. First, it can lead to cell death via, or independently of, apoptosis, thereby removing, for example, larval tissues during metamorphosis in *Drosophila* [18]. Second, autophagy can selectively degrade specific proteins and organelles to mediate cellular differentiation [17]. However, exploring the function of autophagy in particular developmental events is still in the initial phase. For example, the process plays an important role in spore and fruiting body formation in fungi, and in the life cycle transition of pathogenic protozoans [19-22]. In the nematode *Caenorhabditis elegans*, autophagic degradation is required for the elimination of paternally distributed mitochondria from [23], and soma-germline separation in, early-stage embryos [24], elongation of the mid-stage embryo [25,26], as well as dauer larva formation [27]. In *Drosophila*, the process is critical for normal development by degrading larval tissues such as the fat body, salivary gland and midgut [18,28-30], and the removal of paternally delivered mitochondria from the zygote [31]. In chicken, autophagy is necessary for ear development [32]. In mammals, the elimination of maternally distributed gene products from early-stage embryos [33-35] and the embryo-to-neonate transition [36] are mediated by the autophagic process. It is also important in cellular differentiation, such as adipocyte, erythrocyte and lymphocyte maturation [37-39].

The compound eye of *Drosophila*, together with antenna, ocelli, head cuticle and palpus, develops from a larval primordium called eye-antennal imaginal disc (**Fig. 1**) [40,41]. This organ is an epithelial bilayer; one layer is the disc proper, which is built up from

columnar cells and gives rise to the retina, and the other layer called peripodial membrane that is involved in modulating columnar cell fates through emitting signaling cues [42]. Cells of the disc proper divide, grow, and then undergo differentiation into photoreceptors and accessory cells [43]. The border between the proliferating and differentiating cells is marked by the morphogenetic furrow (MF), which migrates from the posterior to anterior direction within the disc [44].

Tor (Target of rapamycin) kinase functions as a main upstream negative regulator of autophagy. Hyperactivation of Tor in the eye primordium leads to a massive reduction in the size of the adult organ and interferes with ommatidial patterning (ommatidia become fused or pitted) [45]. This intervention also delays the progression of MF, and causes disorganization or massive loss of photoreceptor cells [45,46]. Tor inactivation similarly compromises eye development by decreasing the rate of proliferation [47]. These data raise the possibility that autophagy is implicated in normal growth and morphogenesis of this organ. Indeed, silencing of *Atg7* behind the MF by a *GMR-Gal4* driver was reported to result in a rough eye phenotype with fused and enlarged ommatidia [48]. Conversely, *Atg7* loss-of-function (lf) mutant animals are characterized by normal eye morphology [49], and, also using *GMR-Gal4*, knockdown of the *Atg1*, *Atg4a*, *Atg5*, *Atg8a*, *Atg9*, *Atg12* or *Atg18a* genes has no effect on ommatidial structure [48,50]. Furthermore, depletion of Atg1, Atg7, Atg8a and Atg12 proteins, performed at 25°C and without coexpressing Dcr-2 (Dicer-2) that would make gene silencing more efficient, also does not interfere with eye development [51]. Eye morphology likewise remains unaffected by overexpressing a dominant-negative mutant allele of *Atg1* [52]. Due to these contradictory data, the role of autophagy in *Drosophila* eye development remains to be elucidated.

In this study we examined the eye disc-specific accumulation of Atg5 and Atg8a proteins, as well as autophagic structures, and found that while the proteins are detectable

nearly ubiquitously in each part of the organ, but most abundantly in the area of the anteriorly located prospective head cuticle, autophagic compartments display a specific distribution pattern, predominantly accumulating within and behind the MF (the latter corresponds to the differentiation zone; DZ). We further demonstrated that RNA interference (RNAi)-mediated depletion of Atg proteins in the developing eye disc by drivers being active in the MF can severely compromise eye formation. In the affected animals, eye development was completely or partially inhibited as a consequence of ectopic cell death. However, the effect of lf mutations in *Atg* genes on eye development was largely rescued by genetic compensatory mechanisms involving the action of alternative transcripts, paralogs or maternally deposited factors. We also found that the *Hox* gene *lab* (*labial*) is expressed in front of and along the MF, and that *Atg8a* expression is strongly influenced in these regions by lab deficiency. These data reveal a novel, developmentally regulated role for autophagy; its cell death-suppressing function is essential for columnar cells in the *Drosophila* eye primordium to survive, thereby acting as a prerequisite for eye morphogenesis. Since this live-or-die cell fate decision is likely to occur in several cell types during development, autophagy may play a more fundamental role in tissue formation than previously thought.

Results

Autophagic structures accumulate in a specific pattern in the eye primordium

Under normal conditions, autophagy operates at basal levels in terminally differentiated cells to maintain normal macromolecule turnover. During differentiation however when cellular constituents are largely reorganized, the process may exhibit an increased activity in the affected cells. To investigate the potential role of autophagy in *Drosophila* eye development, we first examined the accumulation pattern of 2 key autophagy proteins, Atg5 and Atg8a, as

well as Atg5- and Atg8a-positive autophagic structures in the eye primordium of wandering L3 stage (L3W) larvae. At this stage the eye disc is divided into 2 major regions by the MF, the anteriorly located proliferation zone (PZ) and the posteriorly located DZ (**Fig. 1**) [40]. We used an Atg5-specific antibody (**Fig. S1**) to label Atg5 accumulation in this organ. Atg5 is known to localize to the growing phagophore and remain there until recycling eventually from the autophagosome [53]. Using conventional fluorescent microscopy, the antibody staining revealed abundant Atg5 accumulation in each part of the eye disc, but most obviously in the regions of the prospective head cuticle (indicated by yellow arrows in **Figs. 2A** and **S2**). Semiconfocal and confocal microscopy resolutions however uncovered a relatively large amount of Atg5-positive foci labelling early autophagosomal structures in the MF and DZ, as compared with other areas of the organ (**Figs. 2B** to **B'''**, **C** to **C''''** and **S7A**). Consistent with these data, anti-Atg8a antibody staining performed with confocal microscopy also revealed basal levels of autophagic activity in the antennal field and PZ, but much higher levels in the MF and DZ (**Figs. 2D** to **D'''** and **S3A** to **A'''**, **S4**, **S7B**). It is worth to note that anti-Atg8a antibody staining was also highly specific as the expression of *Atg8a*-specific double-stranded RNA (dsRNA) almost completely abolished protein accumulation in the eye disc (**Fig. S4**), and that Atg8a protein, similar to Atg5, was distributed nearly ubiquitously in the eye primordium, most evidently in the prospective head cuticle and MF (see later in this study). Thus, the intensity of Atg5 and Atg8a accumulation did not coincide with the distribution of autophagic structures; while the proteins accumulated nearly ubiquitously in the entire antennal-eye disc, the presence of Atg5- and Atg8a-positive foci (autophagic structures) was mainly concentrated to the regions of MF and DZ. A similar punctuated pattern was detected in these regions when the expression of an *UAS-mCherry-Atg8a* reporter, which marks phagophores, autophagosomes and autolysosomes, was driven by *ey-Gal4(II)* in the entire eye disc (**Figs. 2E** to **E'''** and **S3B** to **B'''**, **S5B**, **S7C**). Staining by LysoTracker

Red, which marks acidic compartments including autolysosomes, lysosomes and multivesicular bodies, also revealed a punctuated pattern predominantly behind the MF (**Figs. S6** and **S7D**). Together, these results point to an unequal distribution for autophagic activity in different parts of the developing eye tissue; autophagic structures predominantly accumulate in the MF and DZ (**Figs. 2**, **S3**, and **S6**, **S7**). The other parts of the eye field, together with the antennal field, exhibit only basal levels of autophagy. These data suggest that the autophagic process is involved in the differentiation and/or survival of retinal precursor cells.

Downregulation of* Atg *genes in the eye disc impairs the development of the organ

Next, we monitored whether silencing of *Atg* genes in the eye primordium affects the development of this organ. In previous studies, *GMR-Gal4* was used to control the expression of *UAS-Atg* RNAi constructs in the eye disc [48,50]. However, the activity of this driver was only detectable behind the MF (*i.e.* within the DZ; **Figs. 1A** and **S5A**), and even its own expression disturbs eye development [54]. In addition, the expression of *GMR-Gal4* is not restricted exclusively to the eye field [55]. Hence, we used 2 *ey-Gal4* drivers, *ey-Gal4(II)* and *ey-Gal4(III)*, to target gene silencing to a broader area of the eye primordium, including regions in front of, along, and behind the MF (**Figs. 1A** and **S5B**, **C**). Importantly, these drivers *per se* did not affect eye formation (**Table S1** and **Fig. 3A**, **D**, **F**). *ey-Gal4(II)*- or *ey-Gal4(III)*-driven silencing of *Atg* genes led to aberrant eye disc and adult eye morphology ranging from small size through abnormal shape to the complete absence of the organ (**Table S1** and **Figs. 3B**, **C**, **E**, **F** and **S8**). Each of the major Atg protein complexes was represented in this set of silencing experiments (**Fig. 3F**). For example, depletion of *Atg101* (induction complex) and *Atg14* (PtdIns3K complex) with the *ey-Gal4(II)* driver resulted in aberrant eye morphology with penetrance of 96.67% and 78.26%, respectively. In addition, we silenced

Atg3 (conjugation system) by *ey-Gal4(III)* (note that Atg3 depletion with *ey-Gal4(II)* caused the lack of the entire eye disc and pupal lethality; **Fig. S8D**). *Atg3* RNAi*/ey-Gal4(III)* animals displayed aberrant eye phenotype with penetrance of 93.1% in males and 82.4% in females. Downregulation of *Atg* genes by *so7-Gal4* driver being active in almost the entire eye field (**Fig. S5D**) similarly affected eye formation (**Fig. S9**). These results suggest that the function of *Atg* genes in front of and/or within the MF is critical for normal eye development, while depletion of Atg proteins in the DZ alone is not sufficient to compromise the morphogenesis of this organ.

Knockdown of certain *Atg* genes, *e.g. Atg3*, *Atg14* and *Atg101*, was manifested as abnormal eye development with a relatively high (over 50%) penetrance while silencing of other *Atg* genes, such as *Atg5* and *Atg13*, did not influence or only slightly affected normal eye formation (**Table S1** and **Fig. 3F**). This may have resulted from the different effectiveness of RNAi constructs we assayed. Indeed, assessing mRNA or protein levels in the eye disc of *Atg* RNAi animals showed a significant reduction in the level of a given mRNA in those cases where the majority of individuals expressed an aberrant eye phenotype, but no change in samples without an obvious phenotype (**Figs. S10** and **S11**). For example, the corresponding Atg protein levels were not significantly changed in *Atg5* RNAi and *Atg13* RNAi female samples showing no phenotype in response to knockdown (**Table S2** and **Fig. S11**). This phenomenon was particularly obvious in case of *Atg8a*, which was targeted by different RNAi constructs (**Fig. S12A**). The construct without effect [*Atg8a* RNAi*(V20)*] was not capable of lowering the accumulation of Atg8a isoforms, whereas the constructs leading to phenotype [*Atg8a* RNAi*(GD)* and *Atg8a* RNAi*(TRiP-1)*] considerably reduced their amount, as compared with control (**Fig. S12B**, **C**). Consistent with these results, the number of autophagic structures was also significantly reduced in *Atg* RNAi animals with compromised eye morphology, but not altered in those RNAi samples displaying normal eye

development, as compared with their corresponding *ey-Gal4* controls (**Figs. 3A'** to **A'''**, **B'** to **B'''**, **C'** to **C'''**, **D'** to **D'''**, **E'** to **E'''**, **G** and **S13**).

To further demonstrate the specificity of eye phenotypes caused by *Atg* gene knockdowns, we could largely rescue normal eye development in *Atg* RNAi animals by introducing a wild-type copy of the corresponding *Atg* gene. First, the eye phenotype of *Atg8a* RNAi and *Atg14* RNAi animals was considerably suppressed by an *Atg8a* reporter transgene (*eGFP-Atg8a*; see later in the manuscript) and a genomic fragment covering *Atg14* (*g-Atg14*) [56], respectively (**Figs. S12D** and **S14**). Then, an extra copy of a genomic fragment (*DC352*) that covers *Atg101* was introduced into *Atg101* RNAi animals. *DC352* represents a transgenic duplication specific to *Atg101* (http://flybase.org/reports/FBab0046578.html), and in a genetic background containing *DC352*, *Atg101* RNAi animals characteristically had normal eye morphology (**Fig. S15A**). The presence of *DC352* also restored autophagic activity to nearly normal levels in *Atg101* RNAi eye samples (**Fig. S15B**).

Some eye selector genes including *ey* (*eyeless*), *Optix* and *eya* (*eyes absent*) are expressed in the peripodial membrane, yet with unknown function [57], and *ey-Gal4(II)* is also active in this part of the eye disc [42]. To examine the possible contribution of autophagy in the peripodial membrane to eye development, we inactivated *Atg* genes exclusively in this tissue by using *c311-Gal4* driver [42], and found no alteration in the eye structure of animals tested (**Table S2** and **Fig. S16**). Thus, autophagy influences eye development in the disc proper only. Together, we conclude that decreasing the activity of *Atg* genes in front of and within the MF severely interferes with *Drosophila* eye development.

Genetic compensatory mechanisms largely rescue autophagic activity and normal eye development in* Atg *loss-of-function mutant animals

We also assessed eye development in *Atg* lf mutant animals to further confirm the importance of the autophagic process in the formation of the organ. Since mutations in certain *Atg* genes are known to cause lethality during early development, we analyzed genetic mosaics to determine the size and morphology of adult eye clonally deficient in an Atg protein. Alternatively, homozygous mutant larvae resulted from the cross of heterozygous parents were monitored. Contrary to previous data reporting almost no effect for mutations in *Atg* genes on *Drosophila* eye formation [49], we found that mutational inactivation of *Atg17* and *Atg1* can seriously affect normal eye morphology. $Atg17^{d130}$ mutant larvae for instance could exhibit even the complete absence of the eye field, *i.e.* a phenotype without eyes (**Fig. S17A**), while *Atg17* and *Atg1* lf mutant adults occasionally displayed a small eye phenotype (**Fig. S17B**, **F**). However, defects in eye development were detectable at much lower penetrance in these autophagy-defective mutant systems—only in a few animals among many hundreds we examined—than in *Atg* RNAi animals, in some of which the manifestation of the eye phenotype was almost fully penetrant (**Table S1** and **Fig. 3F**). However, the specificity of eye phenotypes seen in $Atg17^{d130}$ mutant larvae is supported by the fact that normal morphogenesis of the larval eye disc could be significantly rescued by introducing a transgene that contains the wild-type copy of the gene (**Fig. S17C**). The fully penetrant lethality of $Atg17^{d130}$ mutant pupae was also highly suppressed by this transgene; almost half of the transgenic mutants remained alive (**Fig. S17D**). Furthermore, we observed that in $Atg17^{d130}$ mutant larvae, unlike control, the *htt* (*huntingtin*) gene became strongly overexpressed (**Fig. S17E**). Because *htt* codes for a protein functioning as a scaffold for selective autophagy [58], its hyperactivation in the $Atg17^{d130}$ mutant background may explain why mutant larvae exhibit defects in eye development with a low penetrance only (Atg17 also acts as a scaffold to recruit other Atg proteins to the phagophore assembly site).

It has been recently revealed that genetic compensation induced by deleterious mutations but not gene knockdowns results in a much milder phenotypic effect in mutant animals, as compared with the corresponding RNAi backgrounds [59]. This prompted us to investigate the mechanisms rescuing normal autophagic functions in *Atg* mutant systems. We first measured the level of the newly identified 3 *Atg8a* mRNA isoforms (splice variants), *A*, *B* and *C*, in the eye disc of L3W larvae by semi-quantitative RT-PCR, and found that *A* is expressed abundantly, *B* is present only at very low levels, while *C* is not detectable (**Figs. 4A**, **A'** and **S18**). We further showed that an *Atg8a* mutant allele, *KG07569*, interferes with isoform *A* only in this organ (**Fig. 4A**, **B**), and in the $Atg8a^{KG07569}$ mutant background, the expression of *Atg8a-A* ceased, while isoform *B* became highly activated, as compared with the control (w^{1118}) genetic background (**Figs. 4B** and **S18**). In addition, a weak induction of *Atg8a-C* transcription was also detectable (**Figs. 4B** and **S18**). Next, we monitored transcript levels of *Atg8b*, the sole paralog of *Atg8a* [60,61], in control versus $Atg8a^{KG07569}$ mutant samples. The analysis demonstrated the transcriptional activation of *Atg8b* in response to Atg8a-A deficiency (in control samples *Atg8b* was not expressed) (**Fig. 4C**). Another *Atg8a-A* mutant allele, *d4*, represents a deletion covering the first exonic sequences, that is present only in splice variant *A* (**Fig. 4A**) [62]. Using a primer pair, one member of which is specific to the region that overlaps with deletion *d4* and hence expected to produce no amplification product, we could detect *Atg8a-A* transcript in $Atg8a^{d4}$ mutant samples (**Fig. 4D**). Together, these data imply that ectopic expression of splice variants (*Atg8a-B* and -*C*) and/or a paralog (*Atg8b*), as well as a trans-splicing-like mechanism (when 2 primary RNA transcripts are joined and ligated) may rescue some *Atg8a-A* activities in *Atg8a-A* lf mutant eye samples.

We observed similar compensatory mechanisms for mutations in *Atg18a* and *Atg4a* that also possess a well-defined paralog, *Atg18b* and *Atg4b*, respectively. *Atg18b* became activated in the $Atg18a^{KG07569}$ mutant background (**Figs. 4E** and **S19**), while *Atg4b* was

upregulated in an *Atg4a* mutant background, as compared with control eye disc samples (w^{1118}) (**Figs. 4F** and **S20**). Consistent with results above, a significant amount of Atg8a-positive autophagic structures was detectable in $Atg8a^{KG07569}$ mutant, but not in *Atg8a* RNAi*(GD)* samples (**Fig. 4G** to **G''''**). These data indicate that $Atg8a^{KG07569}$ mutant eye samples are not completely defective for autophagy (indeed, $Atg8a^{KG07569}$ mutant adults had no defect in eye formation, but nearly half of the *Atg8a* RNAi*(GD)* animals exhibited obvious malformations in eye morphology; **Table S1** and **Fig. 3F**). We could also readily identify autophagic structures in eye disc cells clonally deficient in Atg17 or Atg1 function (**Figs. 4H** to **I'**).

Knockdown of *Atg13* and *Atg17* had almost no effect on eye development (**Table S1** and **Fig. 3F**). Deletion alleles of *Atg13* and *Atg17* did also not change (*Atg13*) or only occasionally altered (*Atg17*) the morphogenesis of this organ (**Fig. S17**). This is particularly interesting, as these mutations effectively abolish the transcriptional activity of the corresponding genes in the fat body [63,64]. Analyzing homozygous mutant progeny of heterozygous parents however revealed the presence of both *Atg13* transcript and protein in the eye disc of L3W larvae (**Figs. S21A** to **A''** and **S22A**, **A'**). Similar to these results, *Atg17*-specific mRNA could also be detected in eye disc samples dissected from homozygous *Atg17* mutants (**Figs. S21B**, **B'** and **S22B**). Since both mutations ($Atg13^{\Delta 81}$ and $Atg17^{d130}$) represent large deletions covering a significant part of the corresponding coding region, the presence of transcripts (and proteins) could be the consequence of maternally contributed factors. Using a dominant female sterile technique (with the use of ovo^{D1} dominant negative mutation), we generated homozygous *Atg13* mutants with no maternal *Atg13* product, and found that animals die prior to the L3W stage (note that homozygous *Atg13* mutants with maternal contribution die as pupae) (**Fig. S21A'''**). Probably due to these mechanisms, specific transcripts and autophagic structures accumulated, although at lowered levels than in controls,

in *Atg13* and *Atg17* mutant eye disc samples (**Figs. S22** and **S23**). Together, these results raise the possibility that maternal effect can also rescue autophagic activity in the eye disc of larvae homozygous for certain *Atg* mutations and derived from heterozygous parents.

To further prove the specificity of genetic compensation eliminating the phenotypic manifestation of *Atg* lf mutations, we silenced *Atg14* in the $Atg14^{\Delta 5.2}$ mutant genetic background (importantly, *Atg14* encodes a single transcript and has no paralog). *Atg14* RNAi animals exhibited a compromised eye phenotype with a relatively high penetrance (**Fig. 3F** and **Table S1**), while the Δ*5.2* mutation [56] did not influence eye morphology **(Fig. 5**). If genetic compensatory mechanisms rescue normal eye morphology in $Atg14^{\Delta 5.2}$ mutants, one would expect the suppression of the eye phenotype caused by RNAi treatment in the mutant background (in the mutant, there is no transcript that the RNAi could degrade). Indeed, the presence of the Δ*5.2* mutation highly rescued normal eye development in *Atg14* RNAi samples (in females, the penetrance of wild-type eye morphology increased from 60% to 95%, in males, it was elevated from 50% to 80%) (**Fig. 5**).

Based on genetic compensation discussed above we postulate that lf mutations in *Atg* genes do not completely eliminate autophagy functions in the affected tissues, thereby masking the phenotypic manifestation of mutant alleles. In good accordance with this assumption, the level of Ref(2)P/SQSTM1/p62 serving as a substrate for autophagy varied significantly among different *Atg* mutant animals (**Fig. S24**). The most significant Ref(2)P accumulation was evident in *Atg13* and *Atg17* mutant samples, the gross mutant phenotype of which appears to be the most severe (lethal) among those examined (the other mutants are viable). Thus, in the latter samples, autophagy still operates, although at decreased levels as compared with control.

Knockdown of* Atg *genes in the eye disc triggers apoptotic cell death

Reduced activity of *Atg* genes in the entire eye disc can retard eye development; the affected animals frequently displayed a small eye or eyeless phenotype (**Table S1** and **Fig. 3**). To address whether these morphological defects result from, at least in part, excessive cell death, we monitored the amount of cells with apoptotic features in normal (control) versus autophagy deficient eye disc samples. We found that samples from animals depleted for Atg3, Atg14 or Atg101 show a much higher number of TUNEL-positive (*i.e.*, fragmented DNA-containing) cells than those derived from the corresponding control [*ey-Gal4(II)/+* or *ey-Gal4(III)/+*] animals (**Fig. 6A** to **E**, **I**). We also performed acridine orange (AO) staining on eye discs of L3W stage larvae to detect acidic compartments, whose accumulation is also a characteristic feature of cells undergoing apoptosis. Samples from *Atg3*, *Atg14* and *Atg101* RNAi animals showed increased levels of AO-positive cells, relative to the corresponding controls (*ey-Gal4*) (**Fig. 6A'** to **E'**, **I**). The elevated number of TUNEL- and AO-positive cells in *Atg* RNAi samples was evident both in front of and behind the MF.

Consistent with these data, human cleaved-CASP3/caspase-3-specific antibody staining also revealed elevated amounts of cells showing increased caspase activity in samples dissected from *Atg3-*, *Atg14-* and *Atg101* RNAi animals, as compared with their corresponding controls (**Fig. 6A''** to **E''**, **J**). This implies increased levels of cell death because this human cleaved-CASP3-specific antibody reveals CASP9-like Dronc activity in *Drosophila*, at least in part due to generating cleaved Drice and cleaved Cp1 effector caspases [65]. A *UAS-Apoliner* reporter has previously been developed to effectively detect effector caspase activity in dying apoptotic cells [66]. Using this tool, we observed intense enzymatic activity in samples dissected from certain *Atg* RNAi animals (**Fig. 6F** to **H**, **K**; in the enlarged part of panels **G** and **H**, intense white labeling —that marks cell death events—is visible). However, contrary to what we found by TUNEL and AO staining, caspase activation was

predominantly detectable in front of the MF (in the PZ and prospective head cuticle). This implies that downregulation of *Atg* genes in the eye disc triggers at least 2 types of programmed cell death, a caspase-independent and caspase-dependent apoptosis. The former mainly occurs in the DZ, while the latter appears in front of the MF. Alternatively, the elimination of cell corpses is perturbed in the DZ, or the sign of human cleaved-CASP3-specific antibody may reflect apoptosis-independent caspase activity in the PZ [65].

In sum, we conclude that defects in autophagy in the developing eye disc promote apoptotic cell death, and this effect is likely to contribute to reduction in size of the affected adult eye. Inhibiting autophagy in the DZ alone (*GMR-Gal4*) does not impair eye development. Thus, autophagic activity in front of and/or within the MF is necessary for the survival of columnar cells in the entire eye disc.

The Hox *gene* lab *(*labial*) is expressed in the disc proper where it modulates the transcription of Atg8a-A*

As demonstrated above, the distribution of Atg8a-positive autophagic structures exhibited a specific pattern in the developing eye tissue, locating predominantly in the MF and DZ (**Figs. 2D to E'''** and **S3, S7**). This observation prompted us to investigate whether autophagy in this tissue is regulated by developmental factors. Transcriptional control of certain *Atg* genes, including *Atg8a*, plays an important role in autophagy induction [52,67,68]. *Atg8a* encodes 3 isoforms, *A*, *B* and *C*, out of which *Atg8a-A* appears to function primarily in early phases of eye development (**Fig. 4A'**, **B**).

To gain insights into the possible mechanisms underlying *Atg8a-A* regulation during eye development, we searched for conserved binding sites of developmental regulatory

factors in the *Atg8a* locus (including both regulatory and coding regions), and identified 2 putative conserved binding sites for Hox proteins (Homeobox-containing transcription factors, a subset of homeotic proteins), master regulators of early developmental events. One of these newly identified sites is located in the first intron of *Atg8a-A*, while the other is located within its 3' untranslated region (3' UTR) (**Fig. 7A**). In close proximity to these Hox regulatory elements, putative binding sites for Hox cofactors including exd (extradenticle) and hth (homothorax) were also identified. The intronic binding site appears to be specific to lab, whereas the 3' UTR binding site seems to be specific to Dfd (Deformed), but other Hox proteins cannot be excluded (the putative lab binding site is actually similar to an alternative lab consensus binding sequence identified in the regulatory region of the *Drosophila* gene *CG11339*) [69,70]. Both *lab* and *Dfd* are expressed in the peripodial membrane of the eye-antennal disc [71,72]. To investigate the expression pattern of these *Hox* genes in more detail, *in situ* hybridization assays were performed by using antisense *lab* and *Dfd* RNA probes. Specificity of the probes was confirmed by *in situ* hybridizations which recapitulated the formerly established expression patterns at certain embryonic stages (FlyBase) (**Figs. 7B**, **C** and **S25A**) [73,74]. According to these results, *lab* was mainly expressed in the MF and in the area from which the head cuticle develops, as well as weak staining was detectable in other parts of the PZ and in the peripodial membrane (**Fig. 7D**, **D'**). It is worth to note that this newly identified expression pattern for *lab* is much wider in this organ than reported previously [71,72]. As strong accumulation of Atg8a-positive autophagic structures was also evident in the MF (**Figs. 2D** to **E'''** and **S3**), we propose that *Atg8a-A* and its potential transcriptional regulator lab share activity domains in the eye disc. We also examined *Dfd* expression, and found that it is only evident in the peripodial membrane (**Fig. S25B**, **B'**), as reported previously [71,72]. This expression domain was further confirmed by analyzing a Dfd-GFP reporter system (**Fig. S25C** to **D'**).

To test whether the 2 newly identified conserved Hox binding sites in the *Atg8a-A* locus are functional *in vivo*, we generated an *eGFP-Atg8a-A* reporter construct containing endogenous upstream and downstream regulatory sequences, together with the entire coding region fused with eGFP (**Fig. 7E**). This construct involves both of the putative Hox binding sites identified in this study. Using site-directed mutagenesis, we further generated 2 mutant versions of the construct. One of them lacks the intronic (*i.e.*, lab-specific) exd-Hox binding site (*$_{mutlab}$eGFP-Atg8a-A*), while the other misses the 3' UTR (*i.e.* Dfd-specific) exd-Hox binding site (*$_{mutHox}$eGFP-Atg8a-A*) (**Fig. 7E'**). Importantly, the wild-type reporter was capable of recapitulating the accumulation pattern of Atg8a proteins, obtained by anti-Atg8a antibody staining and using conventional fluorescent microscopy (**Fig. 7F**, **F'**). The expression intensity of the mutant reporters—integrated into different genomic environments, the 51C and 58A cytological regions—was significantly elevated in the anterior part of the eye disc, in front of the MF, as compared with the control (non-mutated) construct (**Fig. 7G** to **G''**). To determine precisely the area(s) where lab may repress *Atg8a-A* expression, we divided the eye disc into 9 parts, and determined *$_{mutlab}$eGFP-Atg8a-A* expression levels in these subregions (**Figs. 7G'''** and **S26**). Quantification of *$_{mutlab}$eGFP-Atg8a-A* expression intensity showed that the absence of the putative lab binding site leads to elevated expression in the ventral prospective head cuticle and lateral flap (bars highlighted by red frames in **Fig. 7G'''**). *$_{mutHox}$eGFP-Atg8a-A* expression was also much stronger, mainly in the prospective head cuticle and ventral lateral flap, than the corresponding control (**Fig. 7G'''**). Based on these data we propose that these potential Hox binding sites are functional *in vivo*, and that lab, and perhaps (an)other Hox protein(s), directly regulates *Atg8a-A* in these regions. As Dfd accumulates in the peripodial membrane but not in the disc proper (**Fig. S25B** to **D'**), we focused on the putative lab binding site only in further experiments.

To confirm the inhibitory effect that lab exerts on *Atg8a-A* expression in front of the MF, we downregulated and overexpressed *lab* from drivers that are active in this area. Indeed, the former intervention strongly upregulated (**Fig. 7H** to **H''''**) while the latter inhibited (**Fig. 7I** to **I''''**) *eGFP-Atg8a-A* expression. Excessive expression of the reporters was most evident in the region of the ventral head cuticle and lateral flap (yellow arrows in **Fig. 7H'** to **H'''**). Thus, lab inhibits *Atg8a-A* expression in front of the MF, especially in the region of the prospective head cuticle. The inhibitory effect of lab hyperactivation on *Atg8a-A* expression was abolished when the lab binding site mutant reporter version was examined (**Fig. 7I** to **I'''**), confirming the *in vivo* functionality of this particular lab binding site.

The expression profile of these reporters highly coincided with the aberrant eye morphology of *lab* RNAi adult flies. Depletion of *lab* led to a shift in the ventral head-eye cuticle border in favor of the head cuticle (the white arrow in **Fig. 7J'**, **J''**). This phenotype was often associated with the overgrowth of the head cuticle as well as with the lateral overgrowth of adult eyes (**Fig. 7J'''**), morphological features that have been described previously for lab^4 mutants [72]. We conclude that lab inhibits the expression of *Atg8a-A* in the ventral prospective head cuticle and ventral lateral flap via the newly identified putative binding site.

lab upregulates* Atg8a-A *in the MF

As shown above, autophagic structures abundantly accumulate in the MF and DZ (**Figs. 2** and **S3**, **S6**, **S7**). *lab* mRNA was also readily detectable in the MF, but not in the DZ (**Fig. 7D**, **D'**). Upon these data, we investigated how lab influences the transcription of *Atg8a-A* in the MF. To address this issue we silenced *lab* by *ey-Gal4(III)* driver that is active in the MF and DZ (**Figs. 1** and **S5C**). Semi-quantitative PCR experiments revealed highly reduced levels of

Atg8a-A transcript in *lab* RNAi eye disc samples, as compared with controls (**Fig. 8A**). Downregulating *lab* by *GMR-Gal4* driver being active only in the DZ, however, did not alter *Atg8a-A* transcript levels (*lab* is not expressed in the DZ; **Fig. 7D**, **D'**) (**Fig. S27**). Next, relative transcript levels of *Atg8a-A* were determined by quantitative real-time PCR in eye disc samples dissected from L3W larvae with control versus *lab* RNAi and *lab* overexpressing genetic backgrounds (**Fig. 8B**). Data convincingly showed that samples defective for *lab* contain significantly fewer *Atg8a-A* transcripts while those hyperactive for *lab* display higher levels of *Atg8a-A* transcripts than control ones. Thus, lab activates *Atg8a-A* expression in the MF. Taken together, we suggest that in the eye primordium, lab has a dual role in the regulation of *Atg8a-A* activity. First, lab inhibits *Atg8a-A* transcription in the prospective ventral head cuticle and lateral flap, presumably through a lab-exd-specific binding site we identified in the first intron (**Fig. 7G** to **I''''**). It is likely that this regulatory interaction plays a role in the determination of the normal head-eye cuticle border (**Fig. 7J** to **J'''**). Second, lab promotes the expression of *Atg8a-A* in the MF to activate autophagy (**Fig. 8A**, **B**). These opposite effects of lab on *Atg8a-A* activity may be mediated by different Hox cofactors.

lab activates autophagy in the MF and DZ

As shown above, lab increases *Atg8a-A* expression in the MF (**Figs. 8** and **S27**). This finding raised the intriguing possibility that lab influences eye development, at least in part, through modulating autophagic activity. The overexpression of *lab* in the eye disc by *ey-Gal4(II)* driver led to the formation of headless adults. Thus, we overexpressed *lab* by an eye-specific driver with a weaker activity domain, *ey-Gal4(III)*, and found that this intervention results in small eyes or a phenotype without eyes in the affected adults, with almost a full penetrance (**Fig. 9A**, **B**) (in females: no eye, 10.20%; small eye, 89.80%, normal eye, 0%; and in males:

no eye, 18.75%; small eye, 75.00%; normal eye, 6.25%). On the contrary, eye disc-specific silencing of *lab* resulted in eye overgrowth and also compromised eye development through altering the boundary of the head-eye cuticle (**Figs. 7J** to **J'''** and **9C**, **D**).

lab overexpression in the eye disc enhanced autophagic activity (**Fig. 9A'** to **A'''**, **B'** to **B'''**, **E**). Conversely, silencing or mutational inactivation of *lab* in this organ lowered the amount of autophagic structures (**Figs. 9C'** to **C'''**, **D'** to **D'''**, **F** and **S28, S31A** to **A''**). Indeed, the amount of Atg5- and Atg8-positive structures was significantly increased in *lab*-hyperactive (**Fig. 9B'**, **B''**, **E**) but decreased in *lab*-defective genetic backgrounds (**Figs. 9D'**, **D''**, **F** and **S28A**, **A'**, **B**, **B', S31A** to **A''**). Similarly, the number of acidic compartments became higher when *lab* was overexpressed (**Fig. 9B'''**, **E**), but became smaller when *lab* was silenced or inactivated (**Figs. 9D'''**, **F**, and **S28A''**, **B''**). These results indicate that *lab* induces autophagic activity in the MF and DZ. We hypothesize that this effect of lab in the DZ is likely to be realized in a cell non-autonomous manner (as we could detect no *lab* transcript in this disc region), probably through stable products of target genes it regulates.

We also studied the complex regulatory relationship between lab and autophagy in the fat body of L3F larvae. In good agreement with data we obtained from the MF, fat body cells clonally defective for *lab* exhibited very low amounts of LysoTracker-Red-positive (acidic) structures, as compared with control cells (**Fig. S29A** to **A''**). In addition, fat body cells clonally overexpressing *lab* contained much higher amounts of Atg8a-positive autophagic structures than non-overexpressing control ones (**Fig. S29B**, **B'**). Thus, in certain cell types, including columnar cells in the MF and larval fat body cells, lab activates autophagy. The fact that lab induces autophagy in the larval fat body was somehow unexpected since the other Hox proteins were reported to redundantly inhibit developmental autophagy in fat body cells [61]. Thus, lab may be the sole *Drosophila* Hox paralog that activates the autophagic process in this tissue.

To further distinguish the role of *lab* in the peripodial membrane from its role in the disc proper (as *ey-Gal4* drivers are active in both disc proper and peripodial membrane), we used *c311-Gal4* driver [42] to silence *lab* specifically in the peripodial membrane. This intervention enhanced the amount of acidic compartments in columnar cells (**Fig. S30**). Since *lab* knockdown driven by *ey-Gal4(II)* inhibited autophagy in these cells, it is likely that *lab* is endogenously active in certain columnar cells where it modulates the autophagic process.

Both overexpression and inactivation of* lab *in the eye disc cause excessive cell death

As demonstrated above, lab activates autophagy in the MF at least in part through enhancing *Atg8a-A* expression (**Figs. 8A**, **B**, **9B** to **B'''**, **D** to **D'''**, **E**, **F** and **S28**, **S31A** to **A''**). Then, autophagic activity remains high in the DZ in a cell non-autonomous manner (**Fig. 7D**, **D'**). Since defects in autophagy strongly induced ectopic cell death in this organ (**Fig. 6**), we asked whether deregulation of *lab* similarly affects cell survival in the developing eye tissue. We found that depletion of *lab* leads to a massive elevation in the number of TUNEL-positive nuclei and acidic cell bodies, mainly in the DZ (by 2.84 and 1.53 times, respectively) (**Fig. 9C''''** to **D'''''**, **G**). lab deficiency also markedly increased the amount of human cleaved-CASP3-positive cells showing elevated caspase-associated immunoreactivity, but, unlike AO-positive cells, this change was predominantly evident in the PZ and prospective head cuticle (**Fig. S31B** to **B''**, **C**, **C'**). *lab* overexpression similarly increased the number of TUNEL- (8.35 times) and AO-positive (3.49 times) structures (**Fig. 9A''''**, **A'''''**, **B''''**, **B'''''**, **G**), and the amount of cells with chromatin condensation (**Fig. 9H**). We conclude that the Hox protein lab, a master regulator of early development, promotes the survival of columnar cells in the eye primordium via, at least in part, fine tuning autophagy. This effect of lab in the DZ may occur indirectly.

Discussion

Under normal cellular settings, autophagy operates at basal levels to maintain the homeostasis and long-term survival of terminally differentiated cells [75]. Cellular stress factors, however, can trigger autophagic activity at both transcriptional and posttranscriptional levels. This response involves various signaling cues and regulatory proteins [76-78]. The autophagic process also becomes activated during numerous developmental events [16,17,34,35]. For example, during *Drosophila* metamorphosis the degradation of larval tissues is primarily achieved by autophagy [18,30], or at very early stages of mammalian development the elimination of maternally-deposited factors occurs via autophagic degradation [17]. However, little is known about the key regulatory proteins that control the activity of *Atg* genes in developmental processes. Hox proteins, master regulators of early animal development, modulate autophagy in the *Drosophila* fat body [61]. This regulatory interaction between Hox factors and autophagy suggests a much stricter developmental control of the autophagic process than was previously assumed.

In this study we demonstrated that autophagic structures accumulate in a specific pattern in the *Drosophila* eye disc, predominantly in the MF and DZ (**Figs. 2**, and **S3**, **S6**, **S7**), and that this pattern does not reflect the distribution of 2 key Atg proteins, Atg5 and Atg8a, which, using conventional fluorescent microscopy, were detected nearly ubiquitously in this organ, but most intensely in the area from which the head cuticle develops (**Figs. 2A,** and **6F**, **F'**). Other parts of the developing eye tissue displayed only basal levels of autophagic structures. Thus, autophagy displays a characteristic spatial activity pattern in the eye disc of L3W larvae, raising the possibility that lysosome-mediated cellular self-degradation contributes to the morphogenesis of this organ.

We further showed that silencing of several *Atg* genes can seriously compromise the development of the *Drosophila* compound eye (**Table S1** and **Figs. 3A** to **F** and **S8**, **S9**). In this set of experiments *Atg* RNAi constructs were driven by *ey-Gal4(II)*, ey-*Gal4(III)* or *so7-Gal4* that have a broad expression domain in the eye primordium (**Fig. S5B** to **D**). The effectiveness of RNAi constructs was increased by parallel-expressing *Dcr-2* (making RNAi more efficient), and animals were maintained at 29°C, which is the optimum temperature for Gal4 proteins to bind the *UAS* sequence. The pleiotropic effect of *Atg* gene knockdowns included severe reduction in organ size (small eye phenotype), even the complete absence of the organ (eyeless phenotype), and alteration in organ shape (aberrant eye morphology). Some of the *Atg* RNAi constructs we assayed influenced eye growth and morphogenesis with high penetrance, while other constructs proved highly or completely ineffective (**Table S1** and **Fig. 3F**). The former constructs were capable of significantly reducing both the transcriptional and translational activity of the corresponding *Atg* genes as well as the amount of autophagic structures (**Figs. S10**, **S12** and **S13**). Contrary to these functional RNAi samples, the latter failed to lower the corresponding protein levels, and were unable to modulate autophagic activity (**Figs. S11** to **S13**). To provide an additional evidence for the specificity of eye phenotypes caused by *Atg* knockdowns, we rescued normal eye development in *Atg8a-*, *Atg14-* and *Atg101* RNAi animals by a transgene carrying the wild-type copy of the corresponding *Atg* gene (**Figs. S12D** and **S14**) or a duplication bearing the wild-type copy of *Atg101* (**Fig. S15**). In addition, downregulation of *Atg* genes specifically in the peripodial membrane did not affect eye morphogenesis (**Table S2** and **Fig. S16**).

Previous studies have detected no obvious defect in adult eye morphology when *Atg* genes are silenced by *GMR-Gal4* driver [48,50]. It is possible that *GMR-Gal4* is expressed in less excessive levels in the eye disc than *ey-Gal4(II)* and *ey-Gal4(III)* do. Alternatively, the function of autophagy is more significant in the MF and/or PZ where *GMR-Gal4* is not active.

We also explored the effect of lf mutations in *Atg* genes on eye development in this organism. In the literature several studies have reported no influence of autophagy on this developmental paradigm [48-52]. Contrary to these data, we found that mutational inactivation of *Atg17* and *Atg1* can impede eye formation (**Fig. S17**). Some of the mutant animals failed to develop the organ. The percentage of eye phenotypes in these mutant backgrounds however was relatively low, appearing only in the minority of animals examined. Lf mutations in other *Atg* genes did not affect eye formation. It has been recently demonstrated in zebrafish that genetic compensatory mechanisms attenuate the phenotypic effect of deleterious mutations but not gene knockdowns [59]. In accordance with these findings, mutations in *Atg4a*, *Atg8a*, and *Atg18a* led to the activation or upregulation of the corresponding paralogous genes, *Atg4b*, *Atg8b* and *Atg18b*, respectively (**Figs. 4A** to **C** and **S12F, S19**, **S20**). Moreover, splice variants of *Atg8a*, *A*, *B* and *C*, identified only recently were expressed in an orchestrated way to compensate their own deficiency; in the eye disc isoform *A* is active (and *B* in a lesser extent), and a mutation that specifically inhibits *Atg8a-A* resulted in the transcriptional activation or upregulation of isoforms *B* and *C* (**Figs. 4A** to **F** and **S12**, **S18**). We also showed the presence of maternally contributed transcripts in homozygous *Atg13* and *Atg17* mutant samples derived from heterozygous parents (**Figs. S21** and **S22**). Thus, multiple compensatory mechanisms can abolish eye phenotypes in *Atg* mutant samples. As an evidence, the $Atg14^{\Delta 5.2}$ mutation, which alone did not affect eye development, strongly suppressed the highly penetrant eye phenotype of *Atg14* RNAi animals (the mutation eliminates the transcripts the RNAi could act on) (**Fig. 5**). The parallel expression of (a) paralog(s) and/or splice variant(s), as well as maternally contributed gene products, each have the potential to rescue autophagic activity in a certain *Atg* mutant background. In other words, many *Atg* mutant animals examined so far are not completely defective for autophagy. Indeed, we could readily detect autophagic structures in eye disc

samples dissected from *Atg8a*, *Atg13*, *Atg17* and *Atg1* lf mutants (**Figs. 4G** to **I'** and **S23**). In the light of these results, the functional analysis of *Atg* mutant systems requires more attention in future genetic studies on *Drosophila* and on other models [79].

In *Atg* RNAi eye disc samples displaying an obvious phenotype, reduction in autophagic activity was accompanied with enhanced amounts of cells with apoptotic features (**Fig. 6**). Although mutational inactivation of autophagy is known to trigger apoptosis in mammalian cell lines and nematodes [80,81], one can argue that the increased number of apoptotic cell corpses observed in these autophagy deficient systems is simply a consequence of failure in the heterophagic elimination of dying cells, a process that also requires *Atg* gene function [82,83]. However, an increase in caspase activity pointed to excessive levels of apoptosis rather than defects in the engulfment of dying cells (**Fig. 6A''** to **E''**, **F** to **H**, **J**, **K**). Both methods (staining with human cleaved-CASP3-specific antibody and using the Apoliner caspase sensor) essentially led to the same observation, *i.e*. increased levels of apoptotic cell death. This is important because human cleaved-CASP3-specific antibody staining alone could mark positive cells independently of caspase activity [65]. Hence, our present data provide evidence for a role of *Atg* genes in preventing columnar cells from undergoing apoptosis in the *Drosophila* eye disc. In clonal analysis of *Atg* lf mutations with ref(2)P accumulation (also known as SQSTM1 and p62 in mammals) there was no apparent cell death effect. Although the lethal $Atg13^{\Delta 81}$ and $Atg17^{d130}$ mutations significantly increased ref(2)P levels (**Fig. S24**), autophagic activity was still observable in these mutant samples (**Fig. S23**). Presumably, this was due to the presence of maternally contributed factors, explaining why the clonal cells contained autophagic structures (**Fig. 4H** to **I'**). Alternatively, apoptotic cell death occurred in *Atg* mutant cell clones but an apoptosis-induced compensatory proliferation mechanism rescued a nearly-normal eye morphology [84].

In mammalian cell cultures, upregulation of the *Atg8* ortholog *MAP1LC3B* by the transcription factor TFEB leads to elevated autophagy [67]. In *Drosophila*, expression levels of *Atg1* and *Atg8a* are also proportional to autophagic activity [52,68]. Since *Atg1* plays a role in brain development in an autophagy-independent manner [85], we focused on the *Atg8a* genomic region to found potential binding sites for transcription factors that may regulate autophagy during eye morphogenesis. We identified 2 conserved Hox binding sites within the *Atg8a* coding sequences (**Fig. 7A**). Furthermore, conserved binding sites for 2 Hox co-factors, Exd and Hth, were also uncovered in the close vicinity of these Hox regulatory elements (**Fig. 7A**). These sequence data are consistent with a recent finding that Hox proteins including Dfd, Ubx and Abd-B redundantly inhibit autophagy in the fat body to prevent a premature degradation of the organ [61].

By generating an endogenously regulated *eGFP-Atg8a-A* translational fusion reporter (**Fig. 7E**) and its 2 mutant derivatives lacking either of the 2 newly identified conserved Hox-Exd binding sites (**Fig. 7E'**), we revealed that both of these sites are functional *in vivo, i.e.* they are responsive to regulatory cues (**Fig. 7F** to **I''''**). In front of the MF, particularly in the prospective ventral head cuticle, Atg8a-A proteins accumulated at much higher levels in the lab binding site mutant versions than in the corresponding control (**Fig. 7G'''**). Thus, the intronic regulatory element may mediate *Atg8a-A* repression by a specific Hox protein, lab, in the anterior part of the eye disc. In contrast, quantification of *Atg8a-A* transcript levels in the MF (**Fig. 8A**, **B**), together with the analysis of autophagic activity (**Figs. 2** and **S7**), unambiguously showed that lab activates *Atg8a-A* in this eye disc region. In accordance with these results, *lab* was also expressed at relatively high levels in the PZ, particularly the prospective head cuticle, and in the MF (**Fig. 7D** and **D'**). Consistent with these observations, *lab* deficiency in the eye disc led to decreased activity of autophagy, while *lab* hyperactivity elevated the amount of autophagic structures in the MF and DZ (**Figs. 9A** to **D'''** and **S28**,

S31). Thus, *lab* is required for establishing physiological levels of autophagy in the eye disc, most probably by upregulating *Atg8a* in the MF and downregulating this gene in front of the MF, especially in the regions from which the ventral head cuticle develops. In addition to modulating autophagic activity, dysregulation of *lab* in the eye disc caused an excess in the amount of columnar cells undergoing apoptosis (**Figs. 9A'''' to D''''', G**, **H** and **S31**).

Based on these data we propose a model that lab exerts a dual effect on *Atg8a-A* expression in the developing eye primordium (**Fig. 10**). First, lab represses *Atg8a-A* in the prospective ventral head cuticle. This regulatory interaction may depend on the lab regulatory sequence we identified in the first intron of *Atg8a-A* (**Fig. 7A**), and be required for the correct formation of the head-eye cuticle border (**Fig. 7J** to **J'''**). Second, lab activates *Atg8a-A* expression within the MF (**Fig. 8**). As a result, autophagic structures are generated abundantly in this eye region (**Figs. 2** and **S3**, **S6**, **S7**). As the MF moves anteriorly, autophagy activity remains elevated in the DZ. As *lab* transcripts were largely undetectable in the latter area (**Fig. 7D**, **D'**), autophagic regulation is achieved by factors other than lab. Nevertheless, in the MF and DZ, intense autophagy promotes the survival, and likely differentiation, of photoreceptor and accessory cells (**Fig. 10**). We propose that lab is critical for normal eye development in *Drosophila* through supporting survival and differentiation of columnar cells. Together, these data may shed light into a more prominent role of autophagy in tissue shaping and organ development than previously thought. As autophagy is implicated in several human developmental disorders, such as Vici syndrome and myopathies [5,8-10], findings presented by this study may also provide a better understanding of the mechanisms underlying such pathologies, thereby having significant medical relevance.

Acknowledgements

This work was supported by the Hungarian Scientific Research Found grants NK78012 and K109349 to T.V. and M.S., the Hungarian Brain Research Program (KTIA_NAP_13) and OTKA grant K82039 to J.M, and by the New National Excellence Program of the Ministry of Human Capacities. A part of *Drosophila* stocks was obtained from the Bloomington Drosophila Stock Center (NIH P40OD018537) and Vienna Drosophila Resource Center (VDRC, www.vdrc.at). Other *Drosophila* strains and reagents were kindly provided by Barry Dickson, Deborah Hursh, Gábor Juhász, Daniel R. Marenda, Tamás Maruzs and Máté Varga. qPCR experiments and the evaluation of results were assisted by Mónika Kosztelnik. The authors also thank Regina Preisinger, Beatrix Supauer, Tünde Pénzes, Gabriella Szabados, Judit Botond and Sára Simon for the excellent technical assistance.

Materials and Methods

Fly stocks, genetics and conditions

Drosophila strains were maintained on standard cornmeal-sugar-agar medium. Stocks were obtained from the Bloomington *Drosophila* Stock Center (referred to as "BL"), the Vienna *Drosophila* RNAi Center (referred to as "v") and the *Drosophila* Genetic Resource Center, Kyoto (referred to as "DGRC"). Other strains were gift from members of the *Drosophila* research community. We used the following RNAi lines to silence autophagic genes:

Atg1 RNAi (*Atg1*^{JF02273}, BL26731 and *Atg1*^{HMS02750}, BL44034)
Atg2 RNAi (*Atg2*^{HMS01198}, BL34719 and *Atg2*^{JF02786}, BL27706)
Atg3 RNAi (*Atg3*^{HMS01348}, BL34359)
Atg4a RNAi (*Atg4a*^{JF03003}, BL28367 and *Atg4a*^{HMS01482}, BL35740)
Atg5 RNAi (*Atg5*^{JF02703}; BL27551 and *Atg5*^{HMS01244}, BL34899 and *Atg5*^{KK108904}, v104461)
Atg6 RNAi (*Atg6*^{JF02897}, BL28060 and *Atg6*^{HMS01483}, BL35741)
Atg7 RNAi (*Atg7*^{JF02787}, BL27707 and *Atg7*^{HMS01358}, BL34369)
Atg8a RNAi (*Atg8a*^{GD4654}, v43097, *Atg8a*^{JF02895}, BL28989 and *Atg8a*^{HMS01328}, BL34340)
Atg8b RNAi (*Atg8b*^{HMS01245}, BL34900)
Atg9 RNAi (*Atg9*^{JF02891}, BL28055 and *Atg9*^{HMS01246}, BL34901)
Atg10 RNAi (*Atg10*^{HMS02026}, BL40859)
Atg12 RNAi (*Atg12*^{KK111564}, v102362 and *Atg12*^{HMS01153}, BL34675)
Atg13 RNAi (*Atg13*^{KK100340}, v103381 and *Atg13*^{HMS02028}, BL40861)
Atg14 RNAi (*Atg14*^{KK100903}, v108559)
Atg16 RNAi (*Atg16*^{HMS01347}, BL34358)
Atg17 RNAi (*Atg17*^{KK101847}, v104864)
Atg18a RNAi (*Atg18a*^{JF02898}, BL28061 and *Atg18a*^{HMS01193}, BL34714)
Atg101 RNAi (*Atg101*^{KK101226}, v106176 and *Atg101*^{HMS01349}, BL34360)
Vps15 RNAi (*Vps15*^{HMS00908}, BL34092 and *Vps15*^{GL00085}, BL35209)
Vps34/*Pi3K59F* RNAi (*Vps34*^{HMS00261}, BL33384 and *Vps34*^{GL00175}, BL36056)

In this study the following *Gal4* drivers were used:
ey-Gal4(II) was also obtained from BDSC (w*; P{GAL4-ey.H}, 3-8, BL5534)
ey-Gal4(III) was kindly provided by Barry Dickson (Janelia Research Campus, Ashburn, Virginia, US) *GMR-Ga4* (*w*; P{GAL4-ninaE.GMR}12*, BL1104)
so7-Gal4 (*y*^{1} *w*; P{so7-GAL4}A/TM6B*, BL26810)
c311-Gal4 (*y*^{1}*; P{GawB}c311*, BL5937)
Ubi-Gal4 (*w*; P{Ubi-GAL4.U}2/CyO*, BL32551)

UAS-Dcr-2 (*w*^{1118}*; P{UAS-Dcr-2.D}2*, BL24650 and *w*^{1118}*; P{UAS-Dcr-2.D}10,* Bl24651) was used to enhance the efficiency of long hairpin RNAi constructs.

The following mutant stocks were used:

Atg1 (*Atg1*^{KG07993} in *y*^{d2}, *w*^{1118}, *ey-FLP, GMR-lacZ; Atg1*^{KG07993}, *FRT80B/TM6B*, 111645, DGRC and *Atg1*^{25} in *Atg1*^{25}, *FRT80B/TM6B* - kindly provided by Tamas Maruzs, BRC, Szeged, Hungary)
Atg4a (*w*^{1118}*; Mi{ET1}Atg4*^{MB03551}, BL23542)
Atg18a (*w*; P{SUPor-P}Atg18*^{KG03090} *ry*^{506}*/TM6B,* BL13945, modified)
Atg3^{10} [86]
Atg7$^{\Delta 77}$[49]
Atg8a^{KG07569} (outcrossed variant of BL14639)
Atg8a^{d4} [62]
Atg13$^{\Delta 81}$ [63]
Atg14$^{\Delta 5.2}$ (*hs-FLP*; FRT82B, Atg14$^{\Delta 5.2}$*/TM6C*) [56]
Atg17^{d130} (*w*; FRT2A, FRT82B, Atg17*^{d130} [64]
DC352 (*w*^{1118}*; Dp(1;3) DC352, PBac{DC352}VK00033*, BL30762) and *g-Atg14* [56] were used as the genomic rescue of *Atg101* and *Atg14*, respectively. We applied *UAS-Atg17-GFP* [64] for the rescue experiment of *Atg17*^{d130}.
Atg3, *Atg7*, *Atg8a*, *Atg13* and *Atg17* mutant alleles and *UAS-Atg17-GFP* were gift from Gábor Juhász (Eötvös University, Budapest, Hungary), while *Atg14* mutant allele and *g-Atg14* were kindly provided by Tor Erik Rusten (Oslo University Hospital, Oslo, Norway).

Genotype *w*^{1118} (BL3605) was used as the control.

UAS-GFP-mCherry-Atg8a [87,88] and *UAS-Apoliner* (*w*; P{UAS-Apoliner}5*, BL32122), were both recombined with *ey-Gal4(II)* and were used to examine autophagy and effector caspase activity, respectively.

To analyze *Hox* gene functions, the following strains were used:
Dfd-GFP (y^{1} *w***; PBacVK00037,* BL30877)
UAS-lab (*w*^{1118}*; P{UAS-lab.M}X2*, BL7300)
lab RNAi (*labKK*^{107959}, v100311)
w; FRT82B, lab*^{4} [72]

We obtained the following strains to perform mosaic analysis:
w; Ubi-GFP, FRT80B* (BL1620)
y^{d2}*, w*^{1118}*, ey-FLP GMR-lacZ; RpS17*^{4}*, w*$^{+}$*, FRT80B/TM6B* (BL5621)
y^{d2}*, w*^{1118}*. ey-FLP. GMR-lacZ; FRT82B, w*$^{+}$*, l(3)cl-R3*^{1}*/TM6B* (BL5620)
w; neoFRT82B, ry*^{506} (BL2035 with the replacement of the first chromosome to *w**)
w, ey-FLP; FRT82B, Ubi-GFP/TM6B* (a gift from Deborah Hursh)
w, hs-FLP; FRT82B, Ubi-GFP* (a gift from Deborah Hursh)
y, w*, hs-FLP; Act<CD2<Gal4, UAS-GFP, nls, 4-mCherry-Atg8a* [89]

w**; P{neoFRT}82B P{ovoD1-18}3R/st*^{1} *βTub85D*^{D} *ss*^{1} *e*^{s}*/TM3, Sb*^{1} (BL2149) was applied for the Dominant Female Sterile technique [90].

Immunohistochemistry

Fixation and immunostaining of imaginal discs were essentially carried out as described previously [91]. The following primary antibodies were used: rabbit anti-Atg5 (Sigma Aldrich, AV54267) at 1:1000; mouse anti-GFP (Merck Millipore, MAB3580) at 1:500; guinea pig anti-Atonal (gift from Daniel R. Marenda, Drexel University, Philadelphia) [92] at 1:200, rat anti-Atg8a (kindly provided by Gábor Juhász, Eötvös University, Budapest, Hungary) [64,88] at 1:200; rabbit anti-cleaved CASP3/caspase-3 (Cell Signaling Technology, 9661) at 1:400. For nuclear staining, Hoechst 33342 (0.1 mg/ml, Molecular Probes, H-1399) dye was used. Alexa Fluor 488 and Texas Red (Life Technologies, A21210, A11088, T2767) at 1:500 were used as secondary antibodies.

LysoTracker Red and acridine orange staining, TUNEL assay

L3W stage larvae were dissected in PBS (Sigma, P4417), and stained for the eye-antennal imaginal disc (together with the mouth hook and larval brain) using the fluorescent dye LysoTracker Red (Life Technologies, L7528) in 1:1000 dilution for 2 min. Samples were washed once with PBS, and incubated 2 times in PBS for 2.5 min. Eye-antennal discs were mounted into glycerol:PBS (4:1) containing Hoechst 33342 (0.1 mg/ml; Molecular Probes, H-1399). Acridine orange staining was carried out as follows. L3W larvae were dissected in PBS, eye-antennal imaginal discs were stained with acridine orange (0.01 mg/ml in PBS) for 2 min. Samples were washed once in PBS, then incubated in PBS for 3 min. Discs were mounted into glycerol:PBS (4:1). TUNEL (Terminal deoxynucleotidyl transferase dUTP nick end-labelling) assay was performed as described previously [93]. The following reagents were used: Equilibrium Buffer (Merck Millipore, S7106), Reaction Buffer (Merck Millipore, S7105), TdT enzyme (Merck Millipore, S7107) anti-digoxigenin-AP (Roche, 11093274910), NBT-BCIP solution (Sigma, 72091).

Analysis of autophagy in larval fat body samples

Preparation of fat bodies was carried out in PBS (Sigma, P4417) solution. LysoTracker Red staining was executed as described above. Covering was achieved in glycerol:PBS (4:1) solution containing 0.1 mg/ml Hoechst 33342 (Life Technologies, H-1399). Starvation was achieved by transferring larvae onto 20% sucrose solution for 3 h, well-fed condition was provided by using a medium containing 0.825 g cornmeal, 0.405 g sugar, 0.585 g yeast, 2 ml water 3 h prior to dissection.

In situ hybridization

To detect *labial* mRNA in the eye disc, *in situ* hybridization was performed using anti-digoxigenin-AP (Roche, 11093274910) and NBT-BCIP solution (Sigma, 72091) [94].

mRNAs were isolated from 10 mg of wandering larvae lysate with Pure Link RNA Mini Kit (Thermo Fisher Scientific, 12183018A), cDNAs were generated by reverse transcription (RevertAid First Strand cDNA Synthesis Kit, Thermo Fisher Scientific, K1621). The probe for *in situ* hybridization was generated by *labial* specific primers (forward: 5'-ACT ACC TGC CAG TGG AAT CG-3' and reverse: 5'-TTC AAC TTT GCT TGC TCG TG-3').

Western blotting

For anti-Atg5 (rabbit; Sigma Aldrich, AV54267) specificity test, fat body samples were dissected from well-fed L3 stage (76-90 h) *Drosophila* larvae. In other cases, proteins were isolated from eye-antennal imaginal discs (20 pairs/sample) of wandering L3 larvae. Membranes were probed with anti-Ref(P)2 (rabbit, 1:2500) [62], anti-Atg13 (rat, 1:5000) [64], anti-Atg8a (rabbit, 1:2500) [88] - all of these were kindly provided by Gábor Juhász, Eötvös University, Budapest, Hungary, alpha-Tub84B (mouse, 1:2500; Sigma, T6199), anti-rabbit IgG alkaline phosphatase (1:1000; Sigma, A3687), anti-mouse IgG alkaline phosphatase (1:1000; Sigma, A5153) and anti-rat IgG alkaline phosphatase (1:1000; Sigma, A8438), and developed by NBT-BCIP solution (Sigma, 72091). Two technical parallels were carried out in each case.

Generation of* eGFP-Atg8a-A *reporter constructs

An endogenously regulated *eGFP-Atg8a-A* reporter construct was generated, containing a 268 base pair-long promoter element, the full length *Atg8a-A* coding sequence except from the stop codon, and *eGFP* inserted into the end of the upstream regulatory sequence. For PCR amplification, the following primers were used: *Atg8a-A* promoter element, forward 5'-CGC GGA TCC GCG GCA GTG TGA CCG TAG GTG TG-3' and reverse 5'-ACA GTT AAC TGT GAT TGC AAT GAA GAG GTA ATT GG-3'; *eGFP*, forward 5'-ACA GTT AAC TGT CAT CCT GGT CGA GCT GGA-3'and reverse 5'-CCG CTC GAG CGG CTT GTA CAG CTC GTC CAT GC-3'; the translation initiation site, forward 5'-CCG CTC GAG CGG ATG AAG TTC CAA TAC AAG GAG GAG-3' and reverse 5'-TGC TCT AGA GCA TCT TCC TGT CAC TTA TCG CTG A-3'. PCR experiments were performed with High Fidelity PCR Enzyme Mix (Thermo Fisher Scientific, K0191). PCR fragments were ligated into the vector pattB (7418 base pair, Getentry accession number: KC896839). *In vitro* mutagenesis was performed by the QuikChange® XL II Site-Directed Mutagenesis Kit (Agilent Technologies, 200521-5). Mutagenesis of the putative Hox|Exd binding site was performed with the following primers: forward 5'-GGT CGT CTT GGG GCT AAA AT-3' and reverse 5'-CCA AGA CGA CCA TTT TAG CC-3'. Using these primers, a Δ*Hox-Exd* (1st intron) deficient *eGFP-Atg8a-A* plasmid was generated, which lacks the TGATCAATTT sequence. Mutagenesis of the putative Hox|Exd binging site in the 3' UTR was made by the following primers: forward 5'-CAC GAT GCA ACA AAA TTC TGT GTG TGT ATG GTT ACG AAT AGG AC-3' and reverse 5'-CAC AGA ATT TTG CAT CGT GGT CCT ATT CGT AAC CAT ACA CA-3'. Using these primers, a Δ*Hox-Exd* (3' UTR)-defective *eGFP-Atg8a-A*

construct was generated, lacking the sequence CATATTTAG. *Drosophila* transgenic lines were created by the ΦC31-based integration system [95], attP-51C, attP-58A and attP-68E were used as landing sites. After performing initial tests, attP-51C and attP-58A insertions were used for further experiments.

Microscopy

TUNEL- and eGFP-Atg8a images were captured with an Olympus BX51 microscope (Eötvös University, Budapest, Hungary) (with a UPlanApo 20x/.070 objective), equipped with a F-ViewII camera (Olympus, Eötvös University, Budapest, Hungary), and the AnalySIS software. Semi-confocal fluorescent images were captured with a Zeiss Axioimager Z1 upright microscope (Eötvös University, Budapest, Hungary) (with Plan-NeoFluar 10x 0.3 NA, Plan-NeoFluar 40x 0.75 NA and Plan-Apochromat 63x 1,4 NA objectives) equipped with an ApoTome; and AxioVision 4.82 and ImageJ 1.45s software were used to examine and evaluate the data obtained. Confocal images of fixed samples were acquired on a Zeiss LSM710 inverted confocal microscope with a Plan-Apochromat 20x/0.8 M27 objective (MTA TTK, Budapest, Hungary); line averaging: 8x; scanning mode: sequential unidirectional; excitation: 405 nm (Hoechst33342), 488 nm (eGFP), and 543 nm (mCherry); main dichroic beam splitter: MBS-405 (Hoechst 33342), MBS-488 (eGFP) and MBS-458/543 (mCherry); Hoechst 33342 was detected 410IF, eGFP was detected between 493 to 575 nm, and mCherry was detected 578IF. Transmission images were captured with the 405 nm laser line. Images were processed by using ZEN software. Photographs of adult eyes were taken with a Nikon SMZ1000 Stereomicroscope (with Nikon Plan APO 1x WD70 objective) equipped with a Media Cybernetics, Evolution MP 5.0 Mega-pixel camera (Eötvös University, Budapest, Hungary) using the QCapture Pro 5.0 software. Stereomicrographs were processed with CombineZ5.

Transmission electron microscopy

Eye-antenna discs were dissected from wandering L3 larvae in PBS, and were fixed with 2% formaldehyde, 0.5% glutaraldehyde, 3 mM $CaCl_2$ and 1% sucrose in 0.1 M Na-cacodylate, pH 7.4 for 1 h at room temperature. After washing with 0.1 M cacodylate buffer, samples were incubated in 0.5% osmium tetroxide for 1 h and in half-saturated aqueous uranyl acetate (for 30 min, at RT), dehydrated in graded series of ethanol, embedded in LR White according to the manufacturer's instructions, and cured for 24 h at 60°C. Ultrathin sections (70 to 80 μm) were stained with 4% uranyl acetate in 50% methanol (for 8 min) and lead citrate (for 3 min) and were examined on a Jeol JEM-1011 transmission electron microscope (Eötvös University, Budapest, Hungary) at 60 kV, and images were obtained with an Olympus/SIS Morada CCD camera (Eötvös University, Budapest, Hungary), using the Olympus/SIS iTEM software.

PCR experiments

30 pairs of eye-antenna disc were dissected from wandering L3 larvae in PBS, collected in TRI Reagent® solution (Zymo Research, R2050-1-50), and homogenized. RNA isolation was done according to the Direct-zol™ RNA MiniPrep kit (Zymo Research, R2050) protocol, which also includes a DNAse treatment. Reverse transcription was performed using RevertAid First Strand cDNA Synthesis Kit (Thermo Fisher Scientific, K1621).

The following primers were used in semi-quantitative RT-PCR to amplify internal controls: *Act5C/Actin5C*, forward 5'- GGA TAC TCC CGA CAC AA-3' and reverse 5'-GAG CAG CAA CTT CGT CA-3'; *Gapdh1*, forward 5'-AAA AAG CTC CGG GAA AAG G-3' and reverse 5'-AAT TCC GAT CTT CGA CAT GG-3'; *RpL32*, forward 5'-GCT AAG CTG TCG CAC AAA TGG-3' and reverse 5'-GTA GCC AAT GCC TAG CTT GTT C-3' (for experiments shown in **Fig. 4**) or 5'-CTT GTT CGA TCC GTA ACC GAT G-3' (for experiments shown in **Fig. 7**). For detection of *Atg4a,* forward 5'-TGG TCA GAT GGT TCT CGC C-3' and reverse 5'-TTC AAG GCA GCG CTT TAA GG-3'; *Atg4b*, forward 5'-TGG TCA GAT GGT TCT CGC C-3' and reverse 5'-AAG GCA CAT GGG GTT TTG G-3'; *Atg18a*, forward 5'-CAG AAA CCA TGA GCC TGC-3' and reverse 5'-AGA CGC TCG ATG AGG AAC AG-3'; *Atg18b*, forward 5'-CTT TAC TTC CCT GTC CGT GC-3' and reverse 5'-TAA AGT GCA TCT TGA GGC-3'; Atg3, forward 5'- CAA GTC AAT TGA GAG AGC CAT C-3' and reverse 5'-TGT CGC TAT CTG GAG TGT GC-3'; *Atg13*, forward 5'-GAG GAC TAC GAC AAG CTG GT-3' and reverse 5'-AGT TTG TCC CTG CCT CTC TC-3'; *Atg14*, forward 5'-CCA TCT GGA CGT GAA CAA TG-3' and reverse 5'-GCA GAG AGT TTT CGT CCT CTG-3'; *Atg17*, forward 5'-GCC ATG AGA AGC TCT GCC TA-3' and reverse 5'-TAC AAG GTG AGC GAG TCC TG-3'; *Atg101*, forward 5'-CAC CTG ACG ACC CTC CAT-3' and reverse 5'-GGG ATC CAA AGT CAC AAT ACT GA-3'. Semi-quantitative RT-PCR for *Atg8a*: one common reverse primer was used to all isoforms 5'-CGT GAT GTT CCT GGT ACA GGG A-3', the forward primers were the followings: *Atg8a-A*, 5'-CAA TAC AAG GAG CAC GC-3'; *Atg8a-B*, 5'-AGT CAT AGA TGC GCT GA-3'; *Atg8a-C*, 5'-ATT CCA GAG CCA AGG AAA TG-3'. For *Atg8b*, forward 5'-ATC CGC AAG CGT ATC AAT CT-3' and reverse 5'-TGA CGA CGT TGT CTG CTT CT-3. For *htt*, forward 5'-GGT GGT CAA TAG TGG AGT GC-3' and reverse 5'-GCG STT ATC TCC GGG TCA TC-3'. 3 to 4 technical parallels were carried out.

For quantitative real-time PCR experiments, the following primers were used: *Atg8a-A*, forward 5'-GGT CAG TTC TAC TTC CTC ATT CGC-3' and reverse 5'-ATA GTC CTC GTG ATG TTC CTG-3'. *Act5C/Actin5C* was used as internal control: forward 5'-CCA GAG ACA CCA AAC CGA AAG-3' and reverse 5'-GAG CAG CAA CTT CGT C-3'. Quantitative real-time PCR was carried out with a Roche LightCycler 480 instrument (Eötvös University, Budapest, Hungary) using the LightCycler® 480 SYBR Green I Master kit (Roche, 03003230001). Three parallel measurements were done, and repeated once.

Image analysis

AxioVision 4.82 and ImageJ 45s software [96] were used to examine and evaluate data. Quantification of dot-like structures (foci) was carried out on cut views, which had been generated by maximum intensity projection of 1 µm thick optical sections in AxioVision 4.82. Image were opened in ImageJ, then channel splitting, background subtraction (rolling ball radii were 5 to 15 in case of eye discs, while for fat body samples were 1 to 5), using default threshold (with adjustment when it was necessary) and analyzing particles were done. TUNEL- and cleaved human CASP3-antibody-positive cells were counted manually in ImageJ, using cut views. Apoliner-GFP-positive nuclei were counted manually in ImageJ, using single optical sections. Regions of the eye filed were identified according to the nuclear staining. Quantification of *eGFP-Atg8a-A*-expression was performed on conventional fluorescent images of the columnar cells-ward side of the eye-antennal discs. Measurement of mean pixel intensity of the selected region of the eye field was done in ImageJ. Quantifications of gel bands from semi-quantitative RT-PCRs or western blots were also carried out in ImageJ, using densitometry analyses. These quantifications highly depend on the number of amplification cycles and/or the time of exposure.

Statistics

A Lilliefors test were used assess whether there was a normal distribution of samples examined. If it was normal, the F test was performed to compare 2 variances in the case of independent samples. If the variances were equal, a two-sample Student t test was used otherwise, a t test for unequal variances (also called the Welch's t test) was applied. If the distribution of a sample is not normal, Mann-Whitney U test was performed. In the case of paired samples, paired t test was applied for normal distribution; else Wilcoxon signed-rank test was used.

Bioinformatics

The sequence of *Atg8a-A* genomic regions from 4 *Drosophila* species (*D. melanogaster*, *D. simulans*, *D. erecta* and *D. sechellia*) were obtained from FLYBASE (www.flybase.com) [97]. Conserved Hox+Exd and Hth binding sites [69,98,99] were identified by BLAST (http://blast.ncbi.nlm.nih.gov/Blast.cgi) [100]. Potential binding sites were aligned with ClustalW (http://www.ebi.ac.uk/Tools/msa/clustalw2/) [101].

References

[1] Liu Y, Levine B. Autosis and autophagic cell death: the dark side of autophagy. *Cell Death Differ* 2014; 22:367–76.

[2] Das G, Shravage BV, Baehrecke EH. Regulation and function of autophagy during cell survival and cell death. *Cold Spring Harb Perspect Biol* 2012; 4. pii: a008813.

[3] Takacs-Vellai K, Bayci A, Vellai T. Autophagy in neuronal cell loss: a road to death. *BioEssays* 2006; 28:1126–31.

[4] Levine B, Kroemer G. Autophagy in the pathogenesis of disease. *Cell* 2008; 132:27–42.

[5] Vellai T, Takács-Vellai K. Regulation of protein turnover by longevity pathways. *Adv Exp Med Biol* 2010; 694:69–80.

[6] Vellai T. Autophagy genes and ageing. C*ell Death Differ* 2009; 16:94–102.

[7] Vellai T, Takacs-Vellai K, Sass M, Klionsky DJ. The regulation of aging: does autophagy underlie longevity? *Trends Cell Biol* 2009; 19:487–94.

[8] Jiang P, Mizushima N. Autophagy and human diseases. *Cell Res*. 2014; 24:69–79.

[9] Mizushima N, Levine B, Cuervo AM, Klionsky DJ. Autophagy fights disease through cellular self-digestion. *Nature* 2008; 451:1069–75.

[10] Sandri M, Coletto L, Grumati P, Bonaldo P. Misregulation of autophagy and protein degradation systems in myopathies and muscular dystrophies. *J Cell Sci* 2013; 126:5325–33.

[11] Feng Y, He D, Yao Z, Klionsky DJ. The machinery of macroautophagy. *Cell Res* 2014; 24:24–41.

[12] Sigmond T, Barna J, Tóth ML, Takács-Vellai K, Pásti G, Kovács AL, Vellai T. Autophagy in Caenorhabditis elegans. *Methods Enzymol* 2008; 451:521–40.

[13] Varga M, Fodor E, Vellai T. Autophagy in zebrafish. *Methods* 2015; 75:172–80.

[14] Fodor E, Sigmond T, Ari E, Lengyel K, Takács-Vellai K, Varga M, Vellai T. Methods to study autophagy in zebrafish. *Methods Enzymol* 2017; 588:467–96.

[15] Yang Z, Klionsky DJ. An overview of the molecular mechanism of autophagy. *Curr Top Microbiol Immunol* 2009; 335:1–32.

[16] Levine B, Klionsky DJ. Development by self-digestion: molecular mechanisms and biological functions of autophagy. *Dev Cell* 2004; 6:463–77.

[17] Mizushima N, Levine B. Autophagy in mammalian development and differentiation. *Nat Cell Biol* 2010; 12:823–30.

[18] Berry DL, Baehrecke EH. Growth arrest and autophagy are required for salivary gland cell degradation in Drosophila. *Cell* 2007; 131:1137–48.

[19] Otto GP, Wu MY, Kazgan N, Anderson OR, Kessin RH. Macroautophagy is required for multicellular development of the social amoeba Dictyostelium discoideum. *J Biol Chem* 2003; 278:17636–45.

[20] Voigt O, Poggeler S. Autophagy genes Smatg8 and Smatg4 are required for fruiting-body development, vegetative growth and ascospore germination in the filamentous ascomycete Sordaria macrospora. *Autophagy* 2013; 9:33–49.

[21] Besteiro S, Williams RA, Morrison LS, Coombs GH, Mottram JC. Endosome sorting and autophagy are essential for differentiation and virulence of Leishmania major. *J Biol Chem* 2006; 281:11384–96.

[22] Alvarez VE, Kosec G, Sant'Anna C, Turk V, Cazzulo JJ, Turk B. Autophagy is involved in nutritional stress response and differentiation in Trypanosoma cruzi. *J Biol Chem* 2008; 283:3454–64.

[23] Sato M, Sato K. Degradation of paternal mitochondria by fertilization-triggered autophagy in C. elegans embryos. *Science* 2011; 334:1141–4.

[24] Zhang Y, Yan L, Zhou Z, Yang P, Tian E, Zhang K, et al. SEPA-1 mediates the specific recognition and degradation of P granule components by autophagy in C. elegans. *Cell* 2009; 136:308–21.

[25] Erdelyi P, Borsos E, Takacs-Vellai K, Kovacs T, Kovacs AL, Sigmond T, et al. Shared developmental roles and transcriptional control of autophagy and apoptosis in Caenorhabditis elegans. *J Cell Sci* 2011; 124:1510–8.

[26] Borsos E, Erdélyi P, Vellai T. Autophagy and apoptosis are redundantly required for C. elegans embryogenesis. *Autophagy* 2011;7:557–9.

[27] Melendez A, Talloczy Z, Seaman M, Eskelinen EL, Hall DH, Levine B. Autophagy genes are essential for dauer development and life-span extension in C. elegans. *Science* 2003; 301:1387–91.

[28] Juhász G, Csikós G, Sinka R, Erdélyi M, Sass M. The Drosophila homolog of Aut1 is essential for autophagy and development. *FEBS Lett* 2003; 543:154–8.

[29] Denton D, Shravage B, Simin R, Mills K, Berry DL, Baehrecke EH, et al. Autophagy, not apoptosis, is essential for midgut cell death in Drosophila. *Curr Biol* 2009; 19:1741–6.

[30] Tracy K, Baehrecke EH. The role of autophagy in Drosophila metamorphosis. *Curr Top Dev Biol* 2013; 103:101–25.

[31] Politi Y, Gal L, Kalifa Y, Ravid L, Elazar Z, Arama E. Paternal mitochondrial destruction after fertilization is mediated by a common endocytic and autophagic pathway in Drosophila. *Dev Cell* 2014; 29:305–20.

[32] Aburto MR, Sanchez-Calderon H, Hurle JM, Varela-Nieto I, Magarinos M. Early otic development depends on autophagy for apoptotic cell clearance and neural differentiation. *Cell Death Dis* 2012; 3:e394.

[33] Tsukamoto S, Kuma A, Murakami M, Kishi C, Yamamoto A, Mizushima N. Autophagy is essential for preimplantation development of mouse embryos. *Science* 2008; 321:117–20.

[34] Hale AN, Ledbetter DJ, Gawriluk TR, Rucker EB, 3rd. Autophagy: regulation and role in development. *Autophagy* 2013; 9:951–72.

[35] Di Bartolomeo S, Nazio F, Cecconi F. The role of autophagy during development in higher eukaryotes. *Traffic* 2010; 11:1280–9.

[36] Kuma A, Hatano M, Matsui M, Yamamoto A, Nakaya H, Yoshimori T, et al. The role of autophagy during the early neonatal starvation period. *Nature* 2004; 432:1032–6.

[37] Baerga R, Zhang Y, Chen PH, Goldman S, Jin S. Targeted deletion of autophagy-related 5 (atg5) impairs adipogenesis in a cellular model and in mice. *Autophagy* 2009; 5:1118–30.

[38] Kundu M, Lindsten T, Yang CY, Wu J, Zhao F, Zhang J, et al. Ulk1 plays a critical role in the autophagic clearance of mitochondria and ribosomes during reticulocyte maturation. *Blood* 2008; 112:1493–502.

[39] Miller BC, Zhao Z, Stephenson LM, Cadwell K, Pua HH, Lee HK, et al. The autophagy gene ATG5 plays an essential role in B lymphocyte development. *Autophagy* 2008; 4:309–14.

[40] Ready DF, Hanson TE, Benzer S. Development of the Drosophila retina, a neurocrystalline lattice. *Dev Biol* 1976; 53:217–40.

[41] Haynie JL, Bryant PJ. Development of the eye-antenna imaginal disc and morphogenesis of the adult head in Drosophila melanogaster. *J Exp Zool* 1986; 237:293–308

[42] Gibson MC, Schubiger G. Peripodial cells regulate proliferation and patterning of Drosophila imaginal discs. *Cell* 2000; 103:343–50.

[43] Pappu KS, Mardon G. Genetic control of retinal specification and determination in Drosophila. *Int J Dev Biol* 2004; 48:913–24.

[44] Wolff T, Ready DF. The beginning of pattern formation in the Drosophila compound eye: the morphogenetic furrow and the second mitotic wave. *Development* 1991; 113:841–50.

[45] Hennig KM, Colombani J, Neufeld TP. TOR coordinates bulk and targeted endocytosis in the Drosophila melanogaster fat body to regulate cell growth. *J Cell Biol* 2006; 173:963–74.

[46] Wang Y-H, Huang M-L. Reduction of Lobe leads to TORC1 hypoactivation that induces ectopic Jak/STAT signaling to impair Drosophila eye development. *Mech Dev* 2009; 126:781–90.

[47] Juhasz G, Hill JH, Yan Y, Sass M, Baehrecke EH, Backer JM, et al. The class III PI(3)K Vps34 promotes autophagy and endocytosis but not TOR signaling in Drosophila. *J Cell Biol* 2008; 181:655–66.

[48] Chen SF, Kang ML, Chen YC, Tang HW, Huang CW, Li WH, et al. Autophagy-related gene 7 is downstream of heat shock protein 27 in the regulation of eye morphology, polyglutamine toxicity, and lifespan in Drosophila. *J Biomed Sci* 2012; 19:52.

[49] Juhasz G, Érdi B, Sass M, Neufeld TP. Atg7-dependent autophagy promotes neuronal health, stress tolerance, and longevity but is dispensable for metamorphosis in Drosophila. *Genes Dev* 2007; 21:3061–6.

[50] Velentzas PD, Velentzas AD, Pantazi AD, Mpakou VE, Zervas CG, Papassideri IS, et al. Proteasome, but not autophagy, disruption results in severe eye and wing dysmorphia: a subunit- and regulator-dependent process in Drosophila. *PloS One* 2013; 8:e80530.

[51] Pérez E, Das G, Bergmann A, Baehrecke EH. Autophagy regulates tissue overgrowth in a context-dependent manner. *Oncogene* 2015; 34:3369–76.

[52] Scott RC, Juhasz G, Neufeld TP. Direct induction of autophagy by Atg1 inhibits cell growth and induces apoptotic cell death. *Curr Biol* 2007; 17:1–11.

[53] Mizushima N, Yamamoto A, Hatano M, Kobayashi Y, Kabeya Y, Suzuki K, et al. Dissection of autophagosome formation using Apg5-deficient mouse embryonic stem cells. *J Cell Biol* 2001; 152:657–68.

[54] Kramer JM, Staveley BE. GAL4 causes developmental defects and apoptosis when expressed in the developing eye of Drosophila melanogaster. *Genet Mol Res* 2003; 2:43–7.

[55] Li WZ, Li SL, Zheng HY, Zhang SP, Xue L. A broad expression profile of the GMR-GAL4 driver in Drosophila melanogaster. *Genet Mol Res* 2012; 11:1997–2002.

[56] Katheder NS, Khezri R, O'Farrell F, Schultz SW, Jain A, Rahman MM, et al. Microenvironmental autophagy promotes tumour growth. *Nature* 2017; 541:417–20.

[57] Atkins M, Mardon G. Signaling in the third dimension: the peripodial epithelium in eye disc development. *Dev Dyn* 2009; 238:2139–48.

[58] Ochaba J, Lukacsovich T, Csikos G, Zheng S, Margulis J, Salazar L, et al. Potential function for the Huntingtin protein as a scaffold for selective autophagy. *Proc Natl Acad Sci USA* 2014; 111:16889–94.

[59] Rossi A, Kontarakis Z, Gerri C, Nolte H, Hölper S, Krüger M, et al. Genetic compensation induced by deleterious mutations but not gene knockdowns. *Nature* 2015; 524:230–3.

[60] Scott RC, Schuldiner O, Neufeld TP. Role and regulation of starvation-induced autophagy in the Drosophila fat body. *Dev Cell* 2004; 7:167–78.

[61] Banreti A, Hudry B, Sass M, Saurin AJ, Graba Y. Hox proteins mediate developmental and environmental control of autophagy. *Dev Cell* 2014; 28:56–69.

[62] Pircs K, Nagy P, Varga A, Venkei Z, Erdi B, Hegedus K, et al. Advantages and limitations of different p62-based assays for estimating autophagic activity in Drosophila. *PloS One* 2012; 7:e44214.

[63] Chang YY, Neufeld TP. An Atg1/Atg13 complex with multiple roles in TOR-mediated autophagy regulation. *Mol Biol Cell* 2009; 20:2004–14.

[64] Nagy P, Karpati M, Varga A, Pircs K, Venkei Z, Takats S, et al. Atg17/FIP200 localizes to perilysosomal Ref(2)P aggregates and promotes autophagy by activation of Atg1 in Drosophila. *Autophagy* 2014; 10:453–67.

[65] Fan Y, Bergmann A. The cleaved-Caspase-3 antibody is a marker of Caspase-9-like DRONC activity in *Drosophila*. *Cell Death Differ* 2010; 17: 534-39

[66] Bardet PL, Kolahgar G, Mynett A, Miguel-Aliaga I, Briscoe J, Meier P, et al. A fluorescent reporter of caspase activity for live imaging. *Proc Natl Acad Sci USA* 2008; 105:13901–5.

[67] Settembre C, Di Malta C, Polito VA, Garcia Arencibia M, Vetrini F, Erdin S, et al. TFEB links autophagy to lysosomal biogenesis. *Science* 2011; 332:1429–33.

[68] Simonsen A, Cumming RC, Brech A, Isakson P, Schubert DR, Finley KD. Promoting basal levels of autophagy in the nervous system enhances longevity and oxidant resistance in adult Drosophila. *Autophagy* 2008; 4:176–84.

[69] Ebner A, Cabernard C, Affolter M, Merabet S. Recognition of distinct target sites by a unique Labial/Extradenticle/Homothorax complex. *Development* 2005; 132:1591–600.

[70] Slattery M, Riley T, Liu P, Abe N, Gomez-Alcala P, Dror I, et al. Cofactor binding evokes latent differences in DNA binding specificity between Hox proteins. *Cell* 2011; 147:1270–82.

[71] Diederich RJ, Pattatucci AM, Kaufman TC. Developmental and evolutionary implications of labial, Deformed and engrailed expression in the Drosophila head. *Development* 1991; 113:273–81.

[72] Stultz BG, Park SY, Mortin MA, Kennison JA, Hursh DA. Hox proteins coordinate peripodial decapentaplegic expression to direct adult head morphogenesis in Drosophila. *Dev Biol* 2012; 369:362–76.

[73] Kumar S, Konikoff C, Van Emden B, Busick C, Davis KT, Ji S, et al. FlyExpress: visual mining of spatiotemporal patterns for genes and publications in Drosophila embryogenesis. *Bioinformatics* 2011; 27:3319–20.

[74] Bergson C, McGinnis W. An autoregulatory enhancer element of the Drosophila homeotic gene Deformed. *EMBO J* 1990; 9:4287–97.

[75] Mizushima N, Komatsu M. Autophagy: renovation of cells and tissues. *Cell* 2011; 147:728–41.

[76] Kroemer G, Marino G, Levine B. Autophagy and the integrated stress response. *Mol Cell* 2010; 40:280–93.

[77] Pietrocola F, Izzo V, Niso-Santano M, Vacchelli E, Galluzzi L, Maiuri MC, et al. Regulation of autophagy by stress-responsive transcription factors. *Semin Cancer Biol* 2013; 23:310–22.

[78] He C, Klionsky DJ. Regulation mechanisms and signaling pathways of autophagy. *Annu Rev Genet* 2009; 43:67–93.

[79] Mauvezin C, Ayala C, Braden CR, Kim J, Neufeld TP. Assays to monitor autophagy in Drosophila. *Methods* 2014; 68:134–9.

[80] Boya P, Gonzalez-Polo RA, Casares N, Perfettini JL, Dessen P, Larochette N, et al. Inhibition of macroautophagy triggers apoptosis. *Mol Cell Biol* 2005; 25:1025–40.

[81] Takacs-Vellai K, Vellai T, Puoti A, Passannante M, Wicky C, Streit A, et al. Inactivation of the autophagy gene bec-1 triggers apoptotic cell death in C. elegans. *Curr Biol* 2005; 15:1513–7.

[82] Qu X, Zou Z, Sun Q, Luby-Phelps K, Cheng P, Hogan RN, et al. Autophagy gene-dependent clearance of apoptotic cells during embryonic development. *Cell* 2007; 128:931–46.

[83] Huang S, Jia K, Wang Y, Zhou Z, Levine B. Autophagy genes function in apoptotic cell corpse clearance during C. elegans embryonic development. *Autophagy* 2013; 9:138–49.

[84] Fan Y, Bergmann A. Apoptosis-induced compensatory proliferation. The Cell is dead. Long live the Cell! *Trends Cell Biol* 2008; 18:467–73.

[85] Toda H, Mochizuki H, Flores R, 3rd, Josowitz R, Krasieva TB, Lamorte VJ, et al. UNC-51/ATG1 kinase regulates axonal transport by mediating motor-cargo assembly. *Genes Dev* 2008; 22:3292–307.

[86] Nagy P, Varga A, Kovacs AL, Takáts S, Juhász G. How and why to study autophagy in Drosophila: It's more than just a garbage chute. *Methods* 2014; 75:151–61.

[87] Nezis IP, Shravage BV, Sagona AP, Lamark T, Bjørkøy G, Johansen T, et al., Autophagic degradation of dBruce controls DNA fragmentation in nurse cells during late Drosophila melanogaster oogenesis. *J Cell Biol*. 2010; 190:523–31.

[88] Takats S, Nagy P, Varga A, Pircs K, Karpati M, Varga K, et al. Autophagosomal Syntaxin17-dependent lysosomal degradation maintains neuronal function in Drosophila. *J Cell Biol* 2013; 201:531–9.

[89] Arsham AM, Neufeld TP. A genetic screen in Drosophila reveals novel cytoprotective functions of the autophagy-lysosome pathway. *PloS One* 2009; 4:e6068.

[90] Chou TB, Perrimon N. The autosomal FLP-DFS technique for generating germline mosaics in Drosophila melanogaster. *Genetics* 1996; 144:1673–9.

[91] Klein T. Immunolabeling of Imaginal Discs. In: Dahmann C, ed. Drosophila: Humana Press, 2008; 253–63.

[92] Melicharek D, Shah A, DiStefano G, Gangemi AJ, Orapallo A, Vrailas-Mortimer AD, Marenda DR. Identification of novel regulators of atonal expression in the developing Drosophila retina. *Genetics*. 2008; 180:2095–110.

[93] McCall K, Baum J, Cullen K, Peterson J. Visualizing Apoptosis. In: Henderson D, ed. Drosophila Cytogenetics Protocols: Humana Press, 2004:431–42.

[94] Wilk R, Murthy SUM, Yan H, Krause HM. In Situ Hybridization: Fruit fly embryos and tissues. Current Protocols Essential Laboratory Techniques: John Wiley & Sons, Inc., 2008.

[95] Bischof J, Maeda RK, Hediger M, Karch F, Basler K. An optimized transgenesis system for Drosophila using germ-line-specific phiC31 integrases. *Proc Natl Acad Sci USA* 2007; 104:3312–7.

[96] Schneider CA, Rasband WS, Eliceiri KW. NIH Image to ImageJ: 25 years of image analysis. *Nat Methods* 2012; 9:671–675,

[97] Attrill H, Falls K, Goodman JL, Millburn GH, Antonazzo G, Rey AJ, et al. FlyBase: establishing a Gene Group resource for Drosophila melanogaster. *Nucleic Acids Res* 2016; 44:D786–92.

[98] Takács-Vellai K, Vellai T, Chen EB, Zhang Y, Guerry F, Stern MJ, et al. Transcriptional control of Notch signaling by a HOX and a PBX/EXD protein during vulval development in C. elegans. *Dev Biol* 2007; 302:661–9.

[99] Regos A, Lengyel K, Takacs-Vellai K, Vellai T. Identification of novel cis-regulatory regions from the Notch receptor genes lin-12 and glp-1 of Caenorhabditis elegans. *Gene Expr Patterns* 2013; 13:66–77.

[100] Madden T. The BLAST Sequence Analysis Tool. In: The NCBI Handbook. 2nd edition. Bethesda (MD): National Center for Biotechnology Information (US), 2013. Available from: https://www.ncbi.nlm.nih.gov/books/NBK153387/

[101] Larkin MA, Blackshields G, Brown NP, Chenna R, McGettigan PA, McWilliam H, et el. ClustalW and ClustalX version 2. *Bioinformatics* 2007; 23:2947–8.

Figure legends

Figure 1. Expression domains of eye selector genes and eye-specific drivers in the *Drosophila* eye disc. (**A**) Schematic representation of the *Drosophila* eye-antenna imaginal disc, which has 2 major parts: the antenna and eye fields (surface view). The main regions of the eye field are indicated (the proliferation and differentiation zones, PZ and DZ; the morphogenetic furrow, MF). Blue arrow shows the direction where the MF migrates. Expression domains of some eye disc-specific selector genes (grey) and different *Gal4* drivers (blue) used in this study are shown. (**B**) Cross sectional view of the eye-antennal imaginal disc.

Figure 2. Autophagic structures accumulate in a specific pattern in the *Drosophila* eye disc. **(A** to **A’’’)** Anti-Atg5 antibody staining shows a nearly uniform Atg5 accumulation in the eye disc, with highest levels in the areas of prospective head cuticle (yellow arrows). Green foci in the differentiation zone (DZ) correspond to Atg5-positive structures (early autophagosomal structures). Pictures were taken by conventional fluorescence microscopy. (**B** to **B’’’**) Optical sectioning by a semiconfocal microscopy reveals an unequal distribution of Atg5-positive autophagic structures in the eye disc, predominantly in the MF and DZ. (**C** to **C’’’’**) Confocal microscopy image showing anti-Atg5-positive autophagic structures. Ato (red) is specific marker for labeling the MF. (**D** to **D’’’**) Anti-Atg8a antibody staining indicates autophagic structures, using optical sectioning of a semiconfocal microscopy. Green foci indicate autophagosomal and autolysosomal membranes. Atg8a-positive structures accumulate most abundantly along and behind the MF (indicated by a white arrow). (**E** to **E’’’**) *mCherry-Atg8a* reporter gene driven by *ey-Gal4(II)* is expressed almost in the entire eye field. Red foci label autophagosomes and autolysosomes. mCherry-Atg8a-positive structures accumulate most

evidently in the DZ. Images in panels A to E''' are positioned as antenna parts are up; bars: 100 μm; samples were prepared from L3W larvae. MF: morphogenetic furrow. Hoechst staining indicates nuclei. Animals were maintained at 25°C.

Figure 3. Silencing of *Atg* genes in the eye disc can severely compromise eye morphology in the affected adults. (**A**) Stereomicrograph of an *ey-Gal4(II)/+* adult head, which served as a control for silencing of *Atg101* and *Atg14*, showing wild-type eye morphology. (**A'**) Atg5 antibody staining indicates early autophagic structures (green dots) in the eye disc of an *ey-Gal4(II)/+* control animal. (**A''**) mCherry-Atg8a accumulation in the eye disc of an *ey-Gal4(II)/+* control animal. Fluorescent foci (red) indicate autophagosomal and autolysosomal structures. (**A'''**) LysoTracker Red staining marks acidic structures in the eye disc of an *ey-Gal4(II)/+* control animal. (**B**) Small eye phenotype of an *ey-Gal4(II)/Atg101* RNAi adult. (**B' to B'''**) Silencing of *Atg101* in the eye disc leads to reduced levels of Atg5- (**B'**) mCherry-Atg8a- (**B''**) and LysoTracker Red- (**B'''**) positive structures. (**C**) The eyeless phenotype of an *ey-Gal4(II)/Atg14* RNAi adult. (**C'** to **C'''**) Depletion of Atg14 in the eye disc leads to reduced levels of Atg5- (**C'**) mCherry-Atg8a- (**C''**) and LysoTracker Red- (**C'''**) positive structures. (**D**) Stereomicrograph of an *ey-Gal4(III)/+* adult head, which served as a control for silencing *Atg3*, showing wild-type eye. (**D'**) Atg5 accumulation, (**D''**) mCherry-Atg8a expression and (**D'''**) LysoTracker Red staining in the *ey-Gal4(III)/+* genetic background. (**E**) Stereomicrograph of an *ey-Gal4(III)/Atg3* RNAi adult head showing a small eye phenotype., (**E'**) Silencing of *Atg3* in the eye disc leads to a reduced amount of Atg5-, (**E''**) mCherry-Atg8a-, and (**E'''**) LysoTracker Red-positive foci. In images **A'** to **A'''**, **B'** to **B'''**, **C'** to **C'''**, **D'** to **D'''** and **E'** to **E'''**, the antenna part is up; bars: 50 μm. At the upper left corner of each image, the red rectangle indicates the area enlarged. Eye disc samples were dissected from L3W larvae. (**F**) Silencing of *Atg* genes in the eye primordium can severely compromise the

development of the organ. The penetrance of eye phenotypes may depend on the efficiency of the RNAi constructs used (also see **Figs. S9** and **S10**). In some cases, like *Atg2*, *Atg3*, *Atg6*, *Atg14* and *Atg101*, the phenotype is manifested with a nearly full penetrance. (**G**) Effect of *Atg3*, *Atg14* and *Atg101* RNAi treatments on autophagic activity in the eye disc of L3W larvae. The ratio of anti-Atg5/mCherry-Atg8a/LysoTracker Red-positive structures and the area of entire eye disc in each image is shown as averages, the data represent relative values. Bars represent mean ±S.D., *: $P<0.05$, **: $P<0.01$, two-sample Student t test, t test for unequal variances or Mann-Whitney U test. Temperature: 29°C, with the exception of **E''**: 18°C, and **D** to **D'''**, **E**, **E'**, **E'''**: 25°C. In fluorescence images, the background expression was highly reduced in order to strengthen the visibility of puncta.

Figure 4. Genetic compensatory mechanisms rescue autophagic activity in *Atg* loss-of-function mutant backgrounds. (**A**) The structure of *Atg8a* gene. Orange boxes represent coding sequences, connecting lines indicate intronic sequences, grey boxes show untranslated regulatory elements. The 3 isoforms, *A*, *B* and *C*, are indicated. (**A'**) Expression levels of the 3 *Atg8a* isoforms in the eye disc. Semi-quantitative PCR was performed with isoform-specific primers; the number of amplification cycles (NACs) was 40. *Atg8a-A* is expressed more abundantly than *Atg8a-B* (for quantification, see **Fig. S14**). (**B**) Expression levels of the *Atg8a* isoforms in an *Atg8a* lf mutant background affecting isoform *A* (allele *KG07569*). While *Atg8a-A* expression ceased, *Atg8a-B* became upregulated, as compared with the control (w^{1118}) background (yellow arrow). NACs were 34, and under this setting *Atg8a-B* is not detectable. (**C**) *Atg8b*, a paralog of *Atg8a*, is upregulated in an *Atg8a* mutant background (arrow). In panels **B** and **C**, *Act5C* and *RpL32* were used as internal controls. (**D**) *Atg8a-A* transcript can be detectable in mutant animals bearing a deletion allele of *Atg8a*, *d4* (one of the primers was designed to the region covering the deletion). (**E**) The expression of *Atg18b*, a

paralog of *Atg18a*, is activated in an *Atg18a* mutant background, but not in control (w^{1118}). (**F**) The *Atg4a* paralog *Atg4b* became upregulated in *Atg4a* mutant animals, as compared with the control (w^{1118}) background. In panels **D** to **F**, *Act5C* was used as an internal control, arrows show the increased transcript levels. (**G** to **G'''**) Atg8a-specific antibody staining displays Atg8a-positive structures in the eye disc of control RNAi (**G**) and *Atg8a* RNAi (**G'**) animals, as well as of control (**G''**) versus $Atg8a^{KG07569}$ mutant animals. *ey-Gal(II)* driver was used with *UAS-Dcr-2*. (**G''''**) Quantification of Atg8a-positive structures in genotypes shown in panels **G** to **G'''**. Bars represent mean ±S.D., **: $P<0.01$; ***: $P<0.001$; Mann-Whitney U test. (**H**) Atg5-specific structures (red) in cells clonally defective for Atg17 function (not green). (**H'**) The corresponding uncolored picture. **(I)** Atg5 accumulation in cells deficient in Atg1 (not green) and in control cells (green). (**I'**) The corresponding uncolored picture. In panels **H'** and **I'**, the dotted lines indicate homozygous mutant cells without *Atg17* and *Atg1* activity, respectively. In images **G'** to **G'''**, **H** and **I**, the antenna part is up; bars: 50 µm. Eye disc samples were dissected from L3W larvae. Temperature was 25°C.

Figure 5. Genetic compensation rescues normal eye development in $Atg14^{\Delta 5.2}$ mutants. *Atg14*-specific RNAi treatment causes highly penetrant defects in eye development in both genders. A loss-of-function mutation in *Atg14*, Δ*5.2*, however, does not influence eye morphology. In $Atg14^{\Delta 5.2}$ mutants with no *Atg14* transcript, the eye phenotype caused by *Atg14* RNAi treatment is significantly suppressed (the mutation eliminates the transcript on which RNAi would act).

Figure 6. Downregulation of *Atg* genes in the eye disc triggers apoptosis. (**A**) TUNEL (terminal deoxynucleotidyl transferase dUTP nick end labeling) staining reveals only a few

fragmented DNA-containing nuclei in the eye disc of an *ey-Gal4(II)/+* larva (control). (**B**, **C**) TUNEL-positive cells in *Atg101* RNAi and *Atg14* RNAi samples. In the RNAi samples, higher numbers of TUNEL-positive nuclei are evident, as compared with controls. **(D)** *ey-Gal4(III)/+* served as a control for (**E**) the *Atg3* RNAi sample. (**A'** to **E'**) Acridine orange (AO) staining identifies acidic (apoptotic) cell bodies (green foci). Control *ey-Gal4/+*samples (**A'**, **D'**) contain much fewer AO-positive structures than the corresponding *RNAi* samples (**B'**, **C'**, **E'**). In images **A** to **H**, the antenna part is up; bars: 50 μm. At the upper left corner of AO-stained images, a small picture shows the entire eye-antenna imaginal disc and a red rectangle indicates the area enlarged. Eye discs were dissected from L3W larvae. (**A''** to **E''**) Human cleaved-CASP3/Caspase-3-specific antibody staining reveal cells showing increased caspase activity and presumably undergoing apoptosis. Control samples (**A''** and **D''**) contain no human cleaved CASP3 immunoreactive cell while the corresponding RNAi samples do (**B''**, **C''**, **E''**). (**F** to **H**) The *Apoliner-gfp* reporter gene functions as a sensor for effector caspase activity in cells undergoing apoptosis. Apoliner-GFP normally binds the plasma membrane (green), but effector caspases (primarily Drice and Cp1) cleaves the nuclear localization signal-GFP tag from the membrane, thereby transferring GFP into the nucleus (white signal, as a result of GFP and Hoechst dye colocalization). (**F**) There is no detectable level of effector caspase activity in the eye disc of an *ey-Gal4(II)/+* larva (control). Silencing of *Atg101* (**G**) and *Atg14* (**H**) in the eye primordium increases the number of nuclei with white signal, as compared with control samples. Enlarged boxes represent disc area in higher magnification, eye discs were dissected from L3W larvae. (**I**) Quantification of cells with apoptotic features in control (*ey-Gal4*) versus *Atg* RNAi genetic backgrounds. Average numbers of TUNEL-positive nuclei (grey) and the area of AO-positive structures (green) are indicated. (**J**) The amount of cells showing caspase-associated immunoreactivity in control (*ey-Gal4*) versus *Atg* RNAi animals. (**K**) Quantification of cells with effector caspase activity,

detected by Apoliner (from panels **F** to **H**). In panel **I**, data are normalized to their own control, in panels **I** to **K**, bars represent mean ±S.D., *: $P<0.05$, **: $p<0.01$, ***: $P<0.005$, two-sample Student t test, t test for unequal variances or Mann-Whitney U test. Temperature for silencing *Atg14* and *Atg101* was 29°C, for silencing *Atg3* was 25°C.

Figure 7. lab represses *Atg8a* in the regions of prospective ventral head cuticle and ventral lateral flap. (**A**) Structure of the *Atg8a-A* coding region and the position of the 2 conserved Hox-exd (blue letters) and hth (green letters) binding sites. Blue boxes indicate coding sequences, connecting lines correspond to intronic sequences, and grey boxes represent 5' and 3' untranslated regions (UTRs). The ATG site and STOP codon are also indicated. Parts of *Atg8a-A* coding sequences from *Drosophila* species were aligned. Identical nucleotides nearby the Hox-exd-hth binding sites are represented by red letters. Nucleotides that belong to the lab site are in uppercase, those belong to the Exd site are in lowercase. The canonical Hox-Exd binding site is indicated. *A distinct consensus lab-exd-hth site that was identified in *CG11339* gene [69]. (**B**) Localization of the *lab* transcript in the 13th embryonic stage (up) and in a late 16th embryonic stage (bottom), according to the FlyBase [73]. (**C**) *In situ* hybridization of *lab* RNA shows an expression pattern being identical to those found previously (in panel **C**). This shows the specificity of the probe (antisense *lab* RNA). (**D**, **D'**) *In situ* hybridization of antisense *lab* RNA in the eye disc. *lab* is mainly expressed in the morphogenetic furrow and in the region of prospective head cuticle. (**D''**) *In situ* hybridization of sense *labial* RNA in the eye disc shows no specific staining (negative control). (**E**) Structure of an *eGFP-Atg8a-A* reporter gene driven by endogenous regulatory elements. Restriction enzymes used for cloning are indicated (arrows). (**E'**) Sequences deleted from the mutated versions of the reporter are indicated by dashes. (**F**) Anti-Atg8a antibody staining on an eye disc. Conventional (non-confocal) fluorescent picture displaying Atg8a

protein distribution, rather than autophagic structures as it was shown in **Figs. 2D** to **D'''** and **S3A** to **A'''**. (**F'**) Expression pattern of *eGFP-Atg8a-A* reporter in the eye disc. Conventional (non-confocal) image. Atg8a-specific antibody staining (**F**) and GFP reporter analysis (**F'**) reveal similar accumulation patterns. (**G** to **G''**) e*GFP-Atg8a-A* expression is significantly enhanced in regions anterior to the MF when either of the potential Hox|Exd binding sites was mutated (in the first intron or 3' UTR, shown in panel E'), as compared to the control reporter. 51C and 58A represent cytological regions. (**G'''**) Quantification of expression (pixel) intensity of e*GFP-Atg8a-A* reporter with wild-type vs. mutant Hox binding sequences in 9 different regions of the eye disc (these regions are shown in **Fig. S24**). Red frames indicate regions where expression levels statistically differ between wild-type and potential lab binding-site-mutated constructs. (**H** to **H'''**) *eGFP-Atg8a-A* expression in eye discs from animals with *lab* deficiency. The area of excessive *Atg8a* expression is indicated by arrows. *ey-Gal4(II)* was used as a driver. (**H''''**) Quantification of *Atg8a-A* expression intensity in genetic background indicated. Only the 2 eye disc regions where significant differences had been observed (**G'''**) were assayed. (**I** to **I'''**) *eGFP-Atg8a-A* expression in eye discs from animals with a *lab*-hyperactive genetic background. Ectopic lab represses *Atg8a* expression. *ey-Gal4(III)* was used as a driver. (**I''''**) Quantification of *Atg8a-A* expression intensity in genetic background indicated. In panels **F**, **F'**, **H** to **H'''** and **I** to **I'''**, pictures were taken by conventional fluorescence microscopy, *i.e.* without (semi)confocal sectioning. (**J** to **J''**) Eye morphology in *lab* RNAi adults. Control (**J**) and RNAi (**J'**, **J''**) samples. Ventral view. In panels **J'** and **J''**, arrows indicate the region with cuticle overgrowth. *ey-Gal4(II)* was used a driver. (**J'''**) Quantification of eye phenotypes in animals depleted for lab. In panels **G'''**, **H''''**, **I''''** and **J'''**, bars represent mean ±S.D., *: $P<0.05$, **: $P<0.01$, ***: $P<0.005$; two-sample Student t test or t test for unequal variances. In panels **D** to **D''**, **F** to **G''**, **H** to **H'''**

and **I** to **I’’’** the antenna part is up; bars 50 μm. Eye discs were dissected from L3W larvae. Experiments were carried out at 25°C (**A** to **G’’’**, **I** to **I’’’’**) or 29°C (**H** to **H’’’’**, **J** to **J’’’**).

Figure 8. lab activates *Atg8a-A* expression in the MF. (**A**) Semi-quantitative RT-PCR experiment displays reduced levels of *Atg8a-A* transcript (red arrow) in *lab* RNAi [driven by *ey-Gal4(III)*] eye discs, as compared with untreated control samples. *RpL32* and *Act5C* serve as internal controls. M; molecular size marker. *ey-Gal4(III)* is expressed in the area of the MF and DZ. Note that *lab* RNAi driven by *GMR-Gal4* that is active in the DZ only does not affect *Atg8a* transcript levels (**Fig. S25**). (**B**) qPCR showing relative levels of *Atg8a-A* mRNA in *lab*-hyperactive (*UAS-lab*) versus *lab*-depleted [driven by *ey-Gal4(III)*] genetic backgrounds, normalized to their own controls and mRNA levels of internal control genes. *Act5C* served as an internal control. Eye disc samples of L3W larvae were assayed. In panel **B**, bars represent mean ±S.D. Temperatures were 29°C (**A** and *lab* RNAi part of **B**) or 25°C (*UAS-lab* part of **B**).

Figure 9. lab promotes autophagic activity in the differentiation zone in a cell non-autonomous way. (**A** to **B’’’’’**) Overexpression of *lab* enhances while its silencing (**C** to **D’’’’’**) reduces autophagic activity in the DZ. Both interventions can lead to excessive cell death revealed by TUNEL and acridine orange (AO) staining. (**A**) Stereomicrograph of an *ey-Gal4(III)/+* adult head, serving as a control for *lab* overexpression. It shows normal eye morphology. (**A’**) Atg5 accumulation in the eye disc of an *ey-Gal4(III)/+* control animal. (**A’’**) mCherry-Atg8a accumulation in the eye disc of an *ey-Gal4(II)/+* animal (control). Red foci correspond to autophagosomes and autolysosomes. (**A’’’**) LysoTracker Red-positive structures in the eye disc of an *ey-Gal4(III)/+* control animal. Red foci indicate lysosomes, autolysosomes and multivesicular bodies. (**A’’’’**) TUNEL staining reveals only a few

fragmented DNA-containing nuclei (*i.e*. cells undergoing apoptosis) in the eye disc of an *ey-Gal4(III)/+* control animal. (**A’’’’’**) AO staining identifies only a few apoptotic cell bodies in the eye disc of an *ey-Gal4(III)/+* a control animal. (**B**) Stereomicrograph of an *UAS-lab/+; ey-Gal4(III)/+* adult head with reduced eye morphology. (**B’**) Overexpression of *lab* during eye development leads to enhanced Atg5 accumulation, (**B’’**) *mCherry-Atg8a* expression, (**B’’’**) LysoTracker Red-positive staining, and (**B’’’’**) increased numbers of TUNEL-positive and (**B’’’’’**) AO-positive structures. (**C** to **C’’’’’**) Samples from *ey-Gal4(II), UAS-Dcr-2/+* animals, serving as controls for *lab* RNAi background (**D** to **D’’’’’**). Controls exhibit normal eye morphology. (**D**) Stereomicrograph of an *ey-Gal4(II), UAS-Dcr-2/lab* RNAi adult head displaying obvious defects in eye morphology (see also **Fig. 6J** to **J’’**). Silencing of *lab* during eye development leads to reduced amount of (**D’**) Atg5-, (**D’’**) mCherry-Atg8a- and (**D’’’**) LysoTracker Red-positive foci, as well as (**D’’’’**) increased amounts of TUNEL- and (**D’’’’’**) AO-positive nuclei. In panels **A’** to **A’’’’’**, **B’** to **B’’’’’**, **C’** to **C’’’’’** and **D’** to **D’’’’’**, the antenna part is up; bars: 50 μm. At the upper left corner of each image, the red rectangle indicates the enlarged area. Eye disc samples were prepared from L3W larvae. (**E**) Quantification of the effect of *lab* overexpression and (**F**) the effect of *lab* silencing and lab^4 mutation on autophagic activity in the MF and DZ. The ratio of areas of anti-Atg5-/mCherry-Atg8a-/anti-Atg8a-/LysoTracker Red-positive structures and the entire eye disc in each image (eye disc) is on average, data are normalized to the corresponding control. (**G**) Quantification of the effect of *lab* overexpression, silencing and lab^4 mutation on apoptosis in the eye disc. The ratio of the number of TUNEL-positive nuclei/the area of the AO-positive structures and the entire eye disc in each image (eye disc) is on average; data are compared to their own control. On panels **E** to **G**, bars represent mean ±S.D., *: $P<0.05$, **: $P<0.01$; two-sample Student t test, t test for unequal variances or Mann-Whitney U test. (**H**) Transmission electron micrograph showing several cells with apoptotic features (arrows) in columnar cells from an

animal overexpressing *lab* in the eye disc; bar 200 nm. Experiments were carried out at 25°C (*UAS-lab* and lab^4) or at 29°C (*lab* RNAi and its control).

Figure 10. Model for how lab regulates *Atg8a*-A and influences autophagic activity in the eye disc. lab may repress *Atg8a* expression in the regions of prospective ventral head cuticle and ventral lateral flap, while *Atg8a* expression and autophagic activity in the MF are induced. Levels of autophagic activity remain elevated behind the moving MF (*i.e*. in columnar cells), which presumably occurs in a cell non-autonomous way. The differentiated regulation of *Atg8a* expression and autophagy in the eye disc by lab may involve distinct Hox cofactors. Brown coloring indicates areas where *lab* transcript is detectable; ochre shows the areas (prospective ventral head cuticle and ventral lateral flap) where lab inhibits *Atg8a* expression; orange coloring indicates the region (MF) where lab activates *Atg8a*. Blue dots show high levels of autophagic structures. PZ, proliferation zone; DZ, differentiation zone; arrows indicate activation, and the bar represents inhibitory interaction.

Dear Editor, dear Dan,

thank you very much for the accurate perusal of our manuscript indicated above. We have addressed almost all of the points you and the associated editor raised, and changed the manuscript accordingly. The two exceptions are listed below:

1. We have used the standard nomenclature of *Drosophila* genes and gene products as FlyBase suggests: https://wiki.flybase.org/wiki/FlyBase:Nomenclature#Proteins. Accordingly, the initial letter of protein names/symbols has remained in capital. Thus, we have used "Labial" ("Lab"), …
2. In several graphs, we have used the Standard Deviation (SD) instead of the Standard Error of the Means (SEM) because SD serves to characterize the variance of samples while SEM concerns the whole population ("SEM is not allowed to use to summarize the variability in the data presented in the results instead of SD", Nagele: Misuse of standard error of the mean (SEM) when reporting variability of a sample. A critical evaluation of four anaesthesia journals. *British J Anaesthesia* 90:514-516; 2003 and, Altman and Bland, Standard deviations and standard errors. *British Med J* 2005; 331(7521):903; 2005).

We hope that our new draft is now suitable for publication in Autophagy. Thanks again for your help in improving the material to its final form.

Sincerely,

Tibor

Tibor Vellai
corresponding author

Supplementary Materials

Developmentally regulated autophagy is required for eye formation in *Drosophila*

Viktor Billes, Tibor Kovács, Anna Manzéger, Péter Lőrincz, Sára Szincsák, Péter István Kulcsár, Ágnes Regős, Tamás Korcsmáros, Tamás Lukácsovich, Gyula Hoffmann, Miklós Erdélyi, József Mihály, Krisztina Takács-Vellai, Miklós Sass, Tibor Vellai

Supplementary materials include:

Genotypes; Supplementary Tables: S1, S2; Supplementary Figures and Figure Legends: S1 to S31

List of genotypes

Figure 2.
(A to D'''): w^{1118}
(E to E'''): *w*; ey-Gal4(II), UAS-mCherry-Atg8a/+*

Figure 3.
(A, A', A'''): *w*; ey-Gal4(II)/+*
(A''): *w*; ey-Gal(II), UAS-mCherry-Atg8a/+*
(B, B', B'''): *w*; ey-Gal4(II)/Atg101* RNAi *(KK101226)*
(B''): *w*; ey-Gal(II), UAS-mCherry-Atg8a/Atg101* RNAi *(KK101226)*
(C, C', C'''): *w*; ey-Gal4(II)/Atg14* RNAi
(C''): *w*; ey-Gal(II), UAS-mCherry-Atg8a/Atg14* RNAi
(D, D', D'''): *w*; ey-Gal4(III)/+*
(D''): *w*; UAS-mCherry-Atg8a/+; ey-Gal4(III)/+*
(E, E', E'''): *ey-Gal4(III)/Atg3 RNAi*
(E''): *w*; ey-Gal4(II), UAS-mCherry-Atg8a/+; Atg3* RNAi/+ (at 18°C)
(F): see Table S1
(G): *ey-Gal4(II)=w*; ey-Gal4(II)/+ Atg101* RNAi=*w*; ey-Gal4(II)/Atg101* RNAi *(KK101226)*. *Atg14* RNAi=*w*; ey-Gal4(II)/Atg14* RNAi. ey-Gal4(III)=*w*; ey-Gal4(III)/+*. *Atg3* RNAi=*w*; ey-Gal4(III)/Atg3* RNAi.

Figure 4.
(A' to D): w^{1118} and $Atg8a^{KG07569}$.
(E): w^{1118} and $Atg18a^{KG03090}$*/Atg18a Df(3L)Exel6112*. (*Atg18a* Df(3L)Exel6112 is a large deletion overlapping the genomic region of *Atg18a*)
(F): w^{1118} and $Atg4^{MB03551}$
(G to G''''): RNAi control = w*; *ey-Gal4(II), UAS-Dcr-2/+*. *Atg8a* RNAi = w*; *ey-Gal4(II), UAS-Dcr-2/+; Atg8a* RNAi/+
(H, H'): Non-green cells: *w*, ey-FLP; FRT82B,* $Atg17^{d130}$. Green cells: *w*, ey-FLP; FRT82B, Ubi-GFP* or *w*, ey-FLP; FRT82B,* $Atg17^{d130}$*/FRT82B, Ubi-GFP*
(I, I'): non-green cells: *w*, ey-FLP;* $Atg1^{KG07993}$*, FRT80B*. Green cells: *w*, ey-FLP; Ubi-GFP, FRT80B* or *w*, ey-FLP; Ubi-GFP, FRT80B /* $Atg1^{KG07993}$*, FRT80B.*

Figure 5. $Atg14^{\Delta 5.2}$ *= ey-Gal4, UAS-FLP/+; FRT82B, Atg14Δ5.2/FRT82B, GMR-hid, l(3)CL-R1*
Atg14 RNAi *= Atg14* RNAi*/ey-Gal4, UAS-FLP; FRT82B/FRT82B, GMR-hid, l(3)CL-R1*
Atg14 RNAi*;* $Atg14^{\Delta 5.2}$ *= Atg14* RNAi*/ey-Gal4, UAS-FLP; FRT82B, Atg14Δ5.2/FRT82B, GMR-hid, l(3)CL-R1*

Figure 6.
ey-Gal4(II) = *w*; ey-Gal4(II)/+*. *Atg101* RNAi = *w*; ey-Gal4(II)/Atg101* RNAi *(KK101226)*. *Atg14* RNAi = *w*; ey-Gal4(II)/Atg14* RNAi. ey-Gal4(III) = *w*; ey-Gal4(III)/+*. *Atg3* RNAi = *w*; ey-Gal4(III)/Atg3* RNAi.

Figure 7.
(C, D, F): w^{1118}
(F'): w^{1118}*; eGFP-Atg8a-A (attP-58A)*
(G): w^{1118}*; eGFP-Atg8a-A (attP-51C)*
(G'): w^{1118}*;* $_{mutlab}$*eGFP-Atg8a-A (attP-51C)*
(G''): w^{1118}*;* $_{mutHox}$*eGFP-Atg8a-A (attP-51C)*
(H to H''''): *eGFP-Atg8a-A* = w*; *eGFP-Atg8a-A (attP-58A)/ey-Gal4(II), UAS-Dcr-2. eGFP-Atg8a-A, lab* RNAi = w*; *lab* RNAi*, eGFP-Atg8a-A (attP-58A)/ ey-Gal4(II), UAS-Dcr-2.* $_{mutlab}$*eGFP-Atg8a-A* = w*; $_{mutlab}$*eGFP-Atg8a-A (attP-*

58A)/ey-Gal4(II), UAS-Dcr-2. $_{mutlab}$*eGFP-Atg8a-A, lab* RNAi = w*; *lab* RNAi, $_{mutlab}$*eGFP-Atg8a-A (attP-58A)/ey-Gal4(II), UAS-Dcr-2*

(I to I’’’’): eGFP-Atg8a-A = *w*; eGFP-Atg8a-A (attP-51C)/+; ey-Gal4(III)/+. eGFP-Atg8a-A; UAS-lab = w*; eGFP-Atg8a-A (attP-51C)/UAS-lab; ey-Gal4(III)/+.* $_{mutlab}$*eGFP-Atg8a-A = w*;* $_{mutlab}$*eGFP-Atg8a-A (attP-51C)/+; ey-Gal4(III)/+.* $_{mutlab}$*eGFP-Atg8a-A; UAS-lab = w*;* $_{mutlab}$*eGFP-Atg8a-A (attP-51C)/UAS-lab; ey-Gal4(III)/+.*(J) *w*; ey-Gal4(II), UAS-Dcr-2/+*, (J’’-J’’’): lab RNAi = *w*; lab* RNAi*/ey-Gal4(II), UAS-Dcr-2*

(J): *w*; ey-Gal4(II), UAS-Dcr-2/+.*

Figure 8.

(A): *w*; ey-Gal4(III)/+* and *w*; lab* RNAi*/+; ey-Gal4(III)/UAS-Dcr-2*

(B): UAS-lab = *w*; UAS-lab/+; ey-Gal4(III)/+. lab* RNAi = *w*; lab* RNAi*/+; ey-Gal4(III)/UAS-Dcr-2*.

Figure 9.

(A, A’, A’’’ to A’’’’’): *w*; ey-Gal4(III)/+*

(A’’): *w*; UAS-mCherry-Atg8a/+; ey-Gal4(III)/+*

(B, B’, B’’’ to B’’’’’ and H): *w*; UAS-lab/+; ey-Gal4(III)/+*

(B’’): *w*; UAS-mCherry-Atg8a/UAS-lab; ey-Gal4(III)/+*

(C, C’, C’’’ to C’’’’’): *w*; ey-Gal4(II), UAS-Dcr-2/+*

(A’’’): *w*; UAS-mCherry-Atg8a/ey-Gal4(II), UAS-Dcr-2*

(D, D’, D’’’ to D’’’’’): *w*; ey-Gal4(II), UAS-Dcr-2/lab* RNAi

(A’’’): *w*; ey-Gal4(II), UAS-mCherry-Atg8a/lab* RNAi*; UAS-Dcr-2/+*

(E to G): *ey-Gal4(III)* = w*; *ey-Gal4(III)/+. UAS-lab* = w*; *UAS-lab/+; ey-Gal4(III)/+. ey-Gal4(II)* = w*; *UAS-Dcr-2; ey-Gal4(II)/+. lab* RNAi = w*; *ey-Gal4(II), UAS-Dcr-2/lab* RNAi; FRT82B = w*, *ey-FLP*; *FRT82B, l(3)cl-R3*^{1}*/FRT82B*. *lab*^{4} *= ey-FLP; FRT82B, l(3)cl-R3*^{1}*/FRT82B*, *lab*^{4}*. l(3)cl-R3*^{1} is a lethal mutation causing the loss of homozygous cells. This latter system leads to eye discs nearly homozygous for *lab*^{4}.

Supplementary Tables

Tables S1. Depletion of Atg proteins in the eye disc can severely compromise the development of the organ.

Gene	*Gal4* driver, UAS construct	Ratio of eye phenotypes (%)	Total amount of samples	Eye phenotype				Sex	T
				Wild-type	Aberrant	Small	Eyeless		
-	*ey-Gal4(II)/+*	0	332	332	0	0	0	F	29°C
		0	286	286	0	0	0	M	29°C
-	*ey-Gal4(II)*	0	362	362	0	0	0	F	25°C
		0	304	304	0	0	0	M	25°C
Dcr-2 overexpr.	*ey-Gal4(II); UAS-Dcr-2/+*	0	386	386	0	0	0	F	29°C
		0	284	284	0	0	0	M	29°C
eGFP #1	*ey-Gal4(II)/+; $eGFP^{pVALIUM20shRNA}$(III)/+*	0	348	348	0	0	0	F	29°C
		0	240	240	0	0	0	M	29°C
eGFP #2	*ey-Gal4(II)/+; $eGFP^{pVALIUM22shRNA}$(III)/+*	0	118	118	0	0	0	F	29°C
		0	88	88	0	0	0	M	29°C
eGFP #3	*ey-Gal4(II)/$eGFP^{pVALIUM22shRNA}$(II)*	0	136	136	0	0	0	F	29°C
		0	2	2	0	0	0	M	29°C
Atg1	*ey-Gal4(II); $Atg1^{JF02273}$*	0.00	136	136	0	0	0	F	25°C
		8.73	126	115	7	4	0	M	25°C
Atg2	*ey-Gal4(III)/$Atg2^{HMS01198}$*	20.45	132	105	4	23	0	F	29°C
		100	36	0	1	33	2	M	29°C
	ey-Gal4(II); UAS-Dcr-2/UAS-Dcr-2; $Atg2^{JF02786}$/+	10	70	63	0	7	0	F	29°C
		33.33	36	24	0	12	0	M	29°C
Atg3	*ey-Gal4(III)/$Atg3^{HMS01348}$*	82.43	74	13	14	41	6	F	29°C
		93.1	58	4	3	51	0	M	29°C
Atg4a	*ey-Gal4(II); $Atg4a^{JF03003}$*	0	244	244	0	0	0	F	25°C
		3.9	308	296	5	6	1	M	25°C
Atg5	*ey-Gal4(II); $Atg5^{JF02703}$*	0	80	80	0	0	0	F	25°C
		13.39	112	97	4	10	1	M	25°C
Atg6	*ey-Gal4(II); UAS-Dcr-2/UAS-Dcr-2; $Atg6^{JF02897}$/+*	100	102	0	0	102	0	F	29°C
		100	64	0	0	64	0	M	29°C
Atg7	*ey-Gal4(II); $Atg7^{JF02787}$*	0	322	322	0	0	0	F	25°C
		1.61	496	488	1	7	0	M	25°C
Atg8a	*ey-Gal4(II); UAS-Dcr-2/+; $Atg8a^{GD4654}$/+*	17.75	845	695	26	123	1	F	29°C
		50.6	500	247	32	216	5	M	29°C
	ey-Gal4(II); UAS-Dcr-2/+; $Atg8a^{JF02895}$/+	15.22	473	401	31	41	0	F	29°C
		42.99	328	187	22	119	0	M	29°C
Atg8b	*ey-Gal4(II)/+; $Atg8b^{HMS01245}$/+*	0	222	222	0	0	0	F	29°C
		6.08	148	139	0	9	0	M	29°C
Atg9	*ey-Gal4(II); $Atg9^{JF02891}$*	0	508	508	0	0	0	F	25°C
		2.88	800	777	6	17	0	M	25°C
Atg10	*ey-Gal4(II)/$Atg10^{HMS02026}$*	0	128	128	0	0	0	F	29°C
		0	84	84	0	0	0	M	29°C
Atg12	*$Atg12^{KK111564}$; ey-Gal4(III)*	0	226	226	0	0	0	F	29°C

		1.09	92	91	0	1	0	M	29°C
Atg13	*ey-Gal4(II); Atg13^{KK100340}*	0	268	268	0	0	0	F	25°C
		0.31	320	319	0	1	0	M	25°C
Atg14	*ey-Gal4(II); UAS-Dcr-2/Atg14^{KK100903}*	78.26	46	10	0	25	11	F	25°C
				pupal lethal				M	25°C
Atg16	*ey-Gal4(II)/+; Atg16^{HMS01347}/+*	0.68	146	145	0	1	0	F	29°C
		1.67	120	118	0	2	0	M	29°C
Atg17	*Atg17^{KK101847}; ey-Gal4(III)*	0.42	238	237	0	1	0	F	29°C
		0	222	222	0	0	0	M	29°C
Atg18a	*ey-Gal4(II); Atg18a^{JF02898}*	0	70	70	0	0	0	F	25°C
		1.59	126	124	2	0	0	M	25°C
Atg101	*ey-Gal(II); UAS-Dcr-2/Atg101^{KK101226}*	96.67	60	2	0	49	9	F	29°C
		100	6	0	0	5	1	M	29°C
Vps15	*ey-Gal4(II)/+; Vps15^{HMS00908}/+*	45.65	46	25	0	21	0	F	29°C
		83.33	6	1	0	5	0	M	29°C
Pi3K59F /Vps34	*ey-Gal4(II)/+; Vps34^{GL00175}/+*	0	244	244	0	0	0	F	29°C
		0.44	226	225	1	0	0	M	29°C

RNAi constructs that work effectively (*i.e.* decrease transcript levels) cause severe, highly penetrant defects in eye development. Those affecting eye development with a relatively high percentage (over 50%) are highlighted by yellow coloring. overexpr., overexpression; F, female; M, male; T, temperature.

Table S2. Depletion of Atg proteins only in the peripodial membrane does not affect eye development.

Gene	**UAS construct**	**Ratio of aberrant eyes (%)**	**Total amount of eyes observed**	**Eye phenotype**			**Sex**	**T**
				Wild-type	**Small**	**Eyeless**		
eGFP #1	*eGFP$^{pVALIUM20shRNA(III)}$*	1.84	326	320	5	1	F	29°C
		1	200	198	2	0	M	29°C
eGFP #3	*eGFP$^{pVALIUM22shRNA(II)}$*	0.77	392	389	3	0	F	29°C
		0	76	76	0	0	M	29°C
Atg1	*Atg1^{HMS02750}*	0.36	558	556	1	1	F	29°C
		0	494	494	0	0	M	29°C

Atg2	*Atg2*^{HMS01198}	larval lethal					F	29° C
		larval lethal					M	29° C
Atg3	*Atg3*^{HMS01348}	larval lethal					F	29° C
		larval lethal					M	29° C
Atg4a	*Atg4a*^{HMS01482}	0.88	114	113	1	0	F	29° C
		0	68	68	0	0	M	29° C
Atg5	*Atg5*^{HMS01244}	0	102	102	0	0	F	29° C
		0	90	90	0	0	M	29° C
Atg6	*Atg6*^{HMS01483}	0	156	156	0	0	F	29° C
		0	92	92	0	0	M	29° C
Atg7	*Atg7*^{HMS01358}	1	100	99	1	0	F	29° C
		0	94	94	0	0	M	29° C
Atg8a	*Atg8a*^{HMS01328}	0.31	324	323	1	0	F	29° C
		0.43	234	233	1	0	M	29° C
Atg8b	*Atg8b*^{HMS01245}	0	298	298	0	0	F	29° C
		0	174	174	0	0	M	29° C
Atg9	*Atg9*^{HMS01246}	1.64	366	360	5	1	F	29° C
		0.91	110	109	1	0	M	29° C
Atg10	*Atg10*^{HMS02026}	0	162	162	0	0	F	29° C
		0	132	132	0	0	M	29° C
Atg12	*Atg12*^{HMS01153}	1.12	178	176	2	0	F	29° C
		0.88	114	113	1	0	M	29° C
Atg13	*Atg13*^{HMS02028}	0	432	432	0	0	F	29° C
		0	410	410	0	0	M	29° C
Atg14	*Atg14*^{KK100903}	0.39	254	253	1	0	F	29°

								C
		0	44	44	0	0	M	29° C
Atg16	*Atg16*^{HMS01347}	0	156	156	0	0	F	29° C
		0	158	158	0	0	M	29° C
Atg18a	*Atg18a*^{HMS01193}	0.98	410	406	2	2	F	29° C
		0	264	264	0	0	M	29° C
Atg101	*Atg101*^{KK101226}	0	120	120	0	0	F	29° C
		0	12	12	0	0	M	29° C
	Atg101^{HMS01349}	0	28	28	0	0	F	29° C
		pupal lethal					M	29° C
		0	60	60	0	0	F	25° C
		0	54	54	0	0	M	25° C
Vps15	*Vps15*^{HMS00908}	pupal lethal					F	29° C
		pupal lethal					M	29° C
		0	60	60	0	0	F	25° C
		0	76	76	0	0	M	25° C
	Vps15^{GL00085}	0.36	560	558	1	1	F	29° C
		0	78	78	0	0	M	29° C
Pi3K59F/ Vps34	*Pi3K59F/Vps34*^{HMS00261}	0	222	222	0	0	F	29° C
		0	10	10	0	0	M	29° C

F, female; M, male; T, temperature.

Supplementary Figures

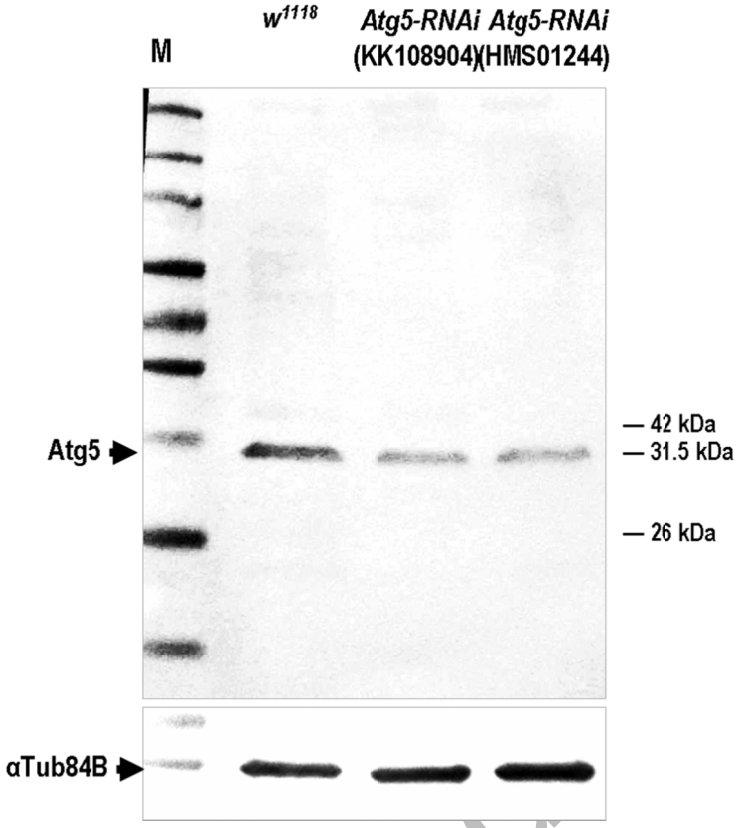

Figure S1. Western blot analysis showing the specificity of the Atg5 antibody used in this study. A single Atg5-specific band is visible (upper arrow) that is weaker in *Atg5* RNAi backgrounds. w^{1118}, control sample. Protein samples were isolated from fat bodies of well-fed L3 staged larvae (76 to 90 h). αTub84B (α-Tubulin at 84B) was used as an internal control. M, molecular mass marker.

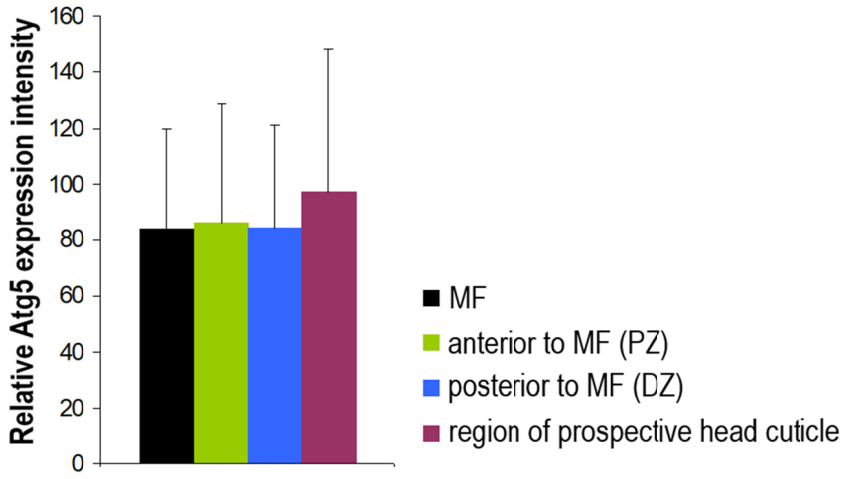

Figure S2. Ubiquitous accumulation of Atg5 in the eye disc. Relative Atg5 protein levels were determined in different regions of the eye disc. Bars represent mean ±S.D., no significant change was detected among the regions examined. MF, morphogenetic furrow; PZ, proliferation zone; DZ, differentiation zone. Genotype: w^{1118}.

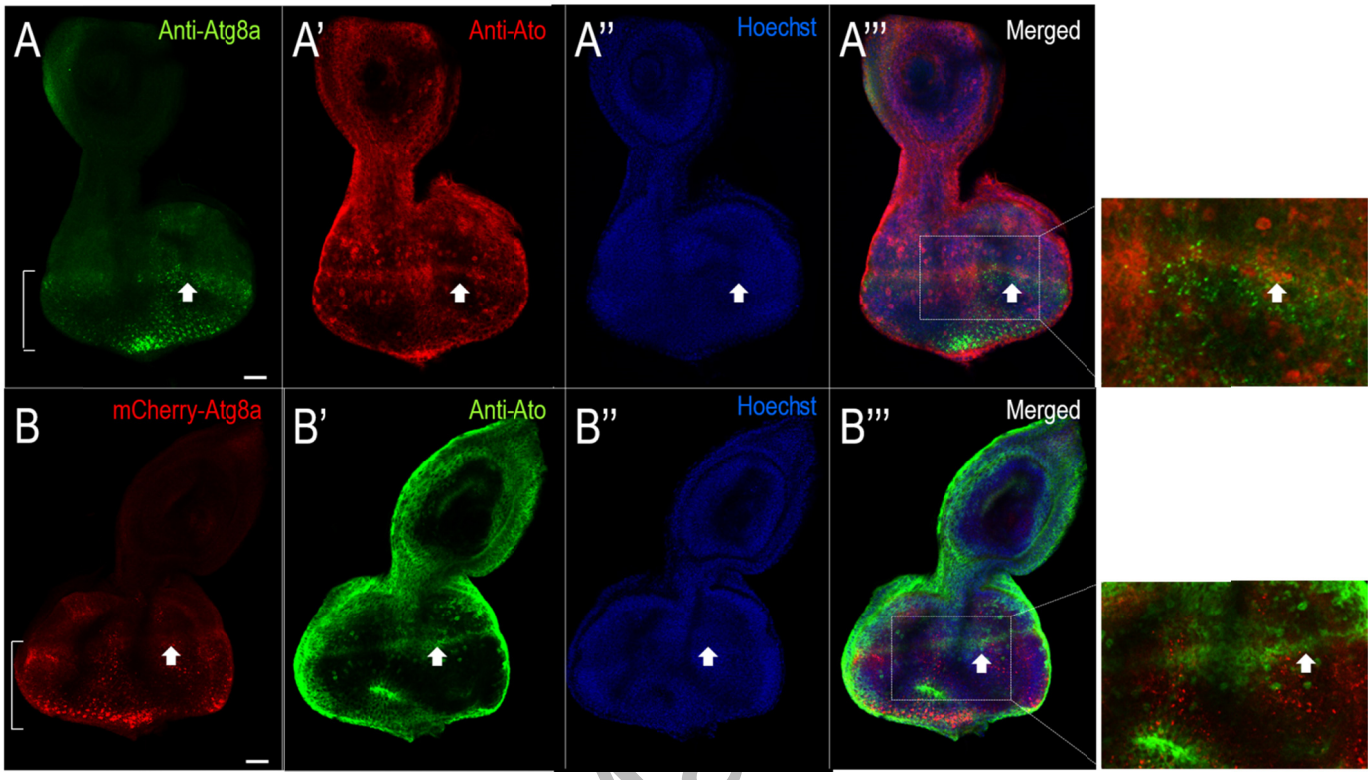

Figure S3. Accumulation of Atg8a-positive autophagic structures in the eye disc. (**A**) Anti-Atg8a antibody staining shows green foci labeling autophagic structures predominantly in the MF and DZ. (**A'**) Anti-Atonal (Ato) antibody staining (red) show the area of MF. (**A''**) Hoechst staining (blue) indicates nuclei. (**A'''**) Merged image. (**B**) Autophagic structures (red foci) labeled by an mCherry-Atg8a reporter. (**B'**) Atonal-specific antibody staining (green) indicates the MF. (**B''**) Hoechst staining (blue) shows nuclei. (**B'''**) Merged image. Pictures in panels **A** to **B'''** were made by confocal microscopy; bars: 10 µm. The bracket indicates the regions of the morphogenetic furrow (MF) and differentiation zone (DZ), the arrow points to the MF. Genotype in (**A** to **A'''**): w^{1118}; (**B** to **B'''**): *w*; ey-Gal4(II)/UAS-mCherry-Atg8a.*

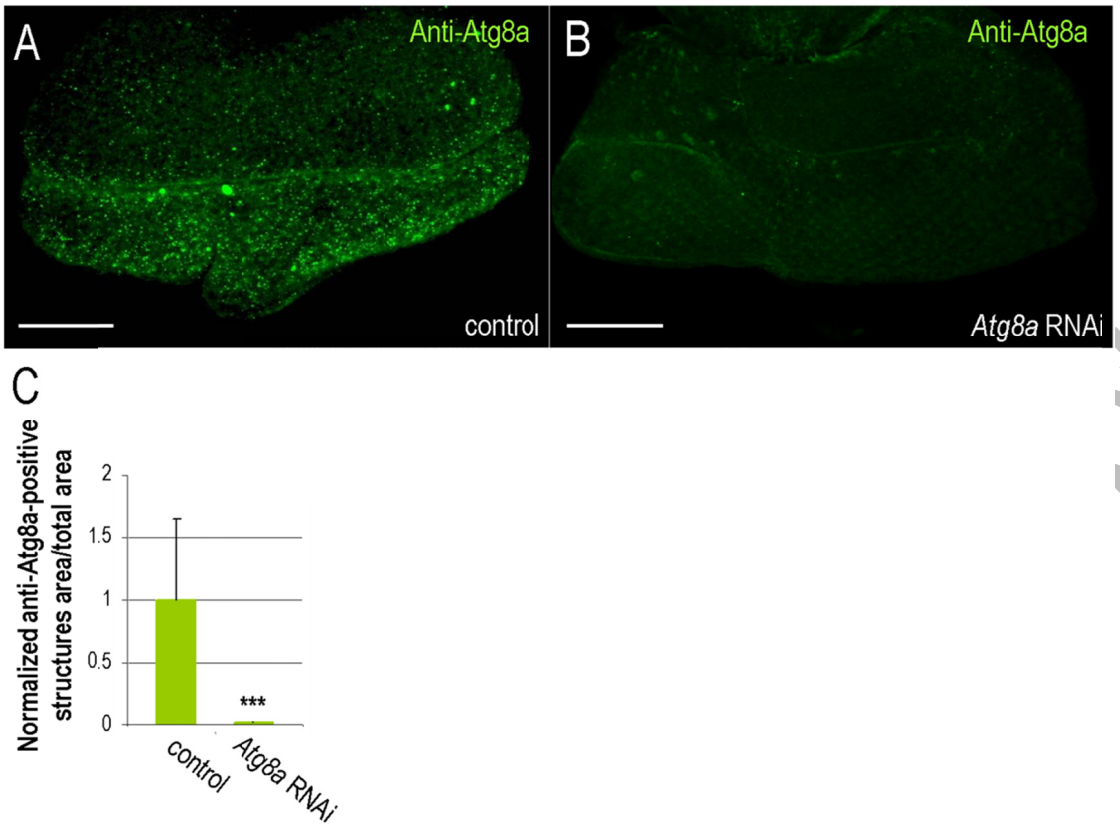

Figure S4. The Anti-Atg8a antibody used in this study specifically labels autophagic structures. (**A**) Anti-Atg8a antibody staining on a control eye disc labels autophagic structures (green foci). (**B**) Anti-Atg8a antibody staining fails to detect autophagic structures in an *Atg8a* RNAi eye disc. (**C**) Quantification of Atg8a-positive structures in control (untreated) versus *Atg8a* RNAi eye disc samples. Bars represent mean ±S.D., ***: $P<0.001$, Mann-Whitney U-test. In panels **A** to **B**, antenna part is up; bars: 50 µm. Samples were dissected from L3W larvae. control = *w*; ey-Gal4(II), UAS-Dcr-2/+*. *Atg8a* RNAi = *w*; ey-Gal4(II), UAS-Dcr-2/+; Atg8a* RNAi (*GD4654) /+*.

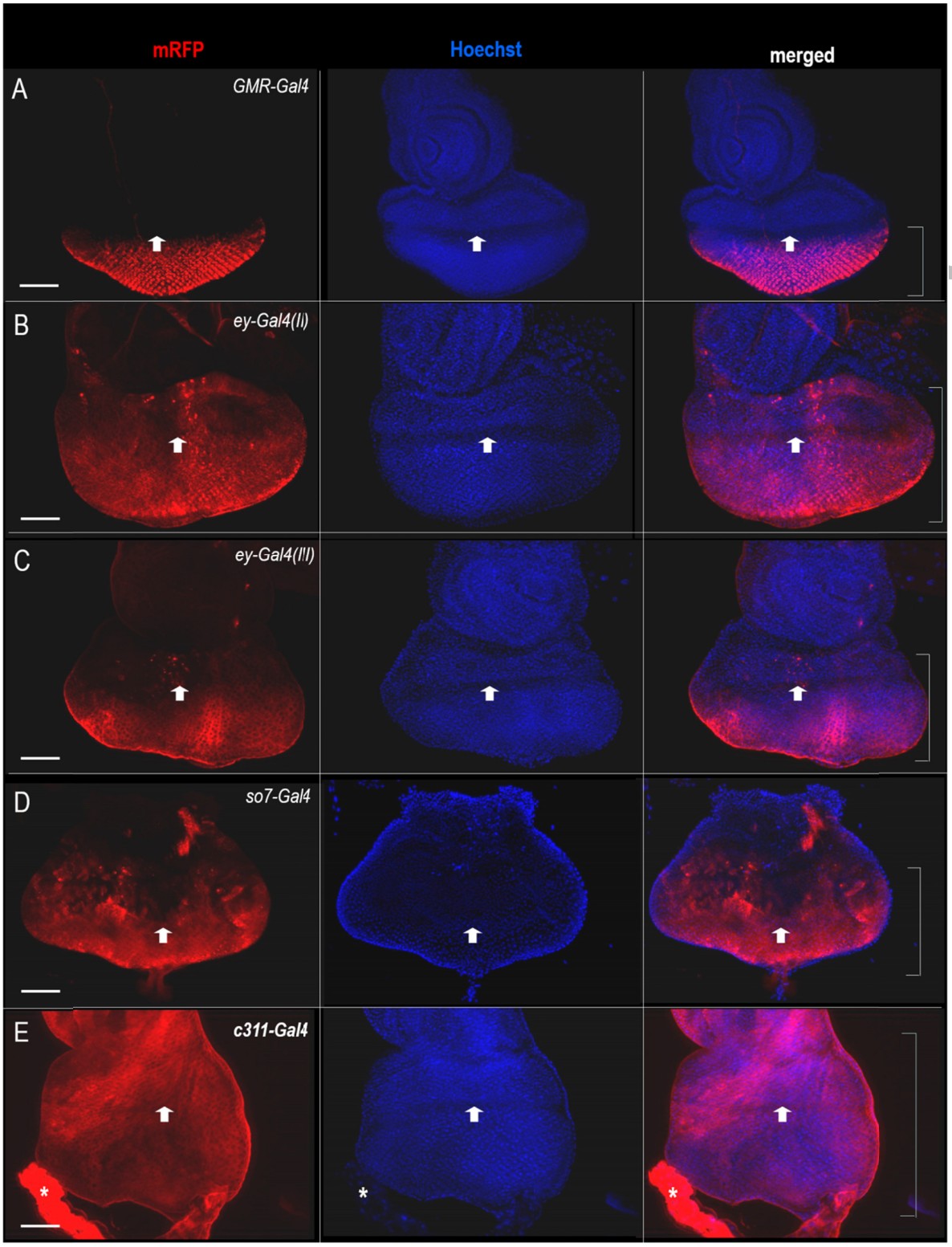

Figure S5. Expression domain of eye-specific *Gal4* drivers used in this study. (**A**) Expression of *GMR-Gal4* in the eye disc is restricted to the differentiation zone. No expression is detectable in the morphogenetic furrow (MF) and proliferation zone, *i.e.* in front of the MF.

(**B**) The broad expression domain of *ey-Gal4(II)* in the eye disc includes each major part of the organ. (**C**) Expression of *ey-Gal4(III)* in the eye disc is evident only in the MF and differentiation zone (behind the MF). A few cell rows in front of the MF also express the reporter. (**D**) Expression of *so7-Gal4* in the eye disc. Reporter activity is evident in almost the entire organ. (**E**) Expression of *c311-Gal4* is detectable only in the peripodial membrane. This driver is highly expressed in the optic stalk (signed by asterisk). In each panel, the white arrow indicates the MF, Hoechst staining (blue) shows nuclei, brackets in the merged pictures designate the extent of expression domains, antenna part is up; bars: 50 µm. *UAS-Apoliner* was used as the source of mRFP. Heterozygous animals were examined.

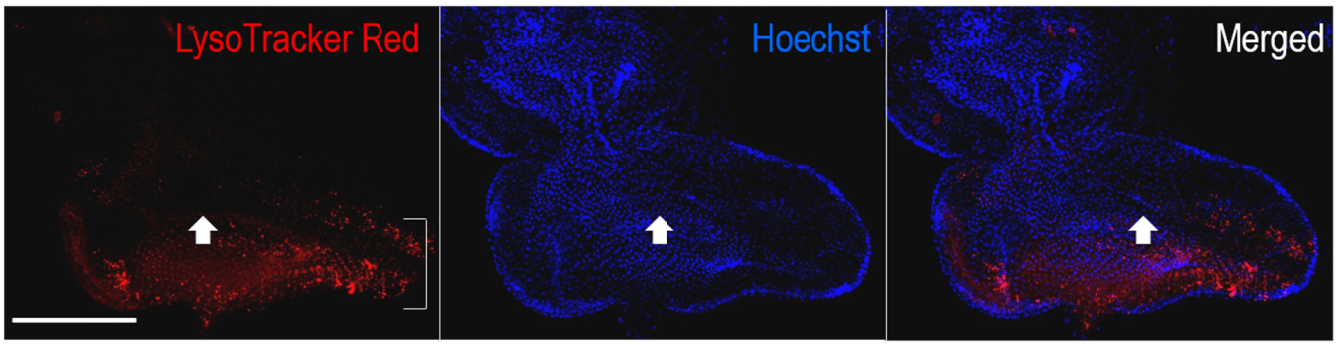

Figure S6. LysoTracker Red staining indicates acidic compartments in the eye disc. Images are positioned as the antenna part is up, the bar represents 100 µm, and the arrow indicates the position of the morphogenetic furrow. The sample was prepared from an L3W larva. Hoechst staining (blue) indicates nuclei. Acidic compartments (autophagosomes, autolysosomes and multivesicular bodies) predominantly accumulate in the MF and differentiation zone (bracket). Genotype: w^{1118}.

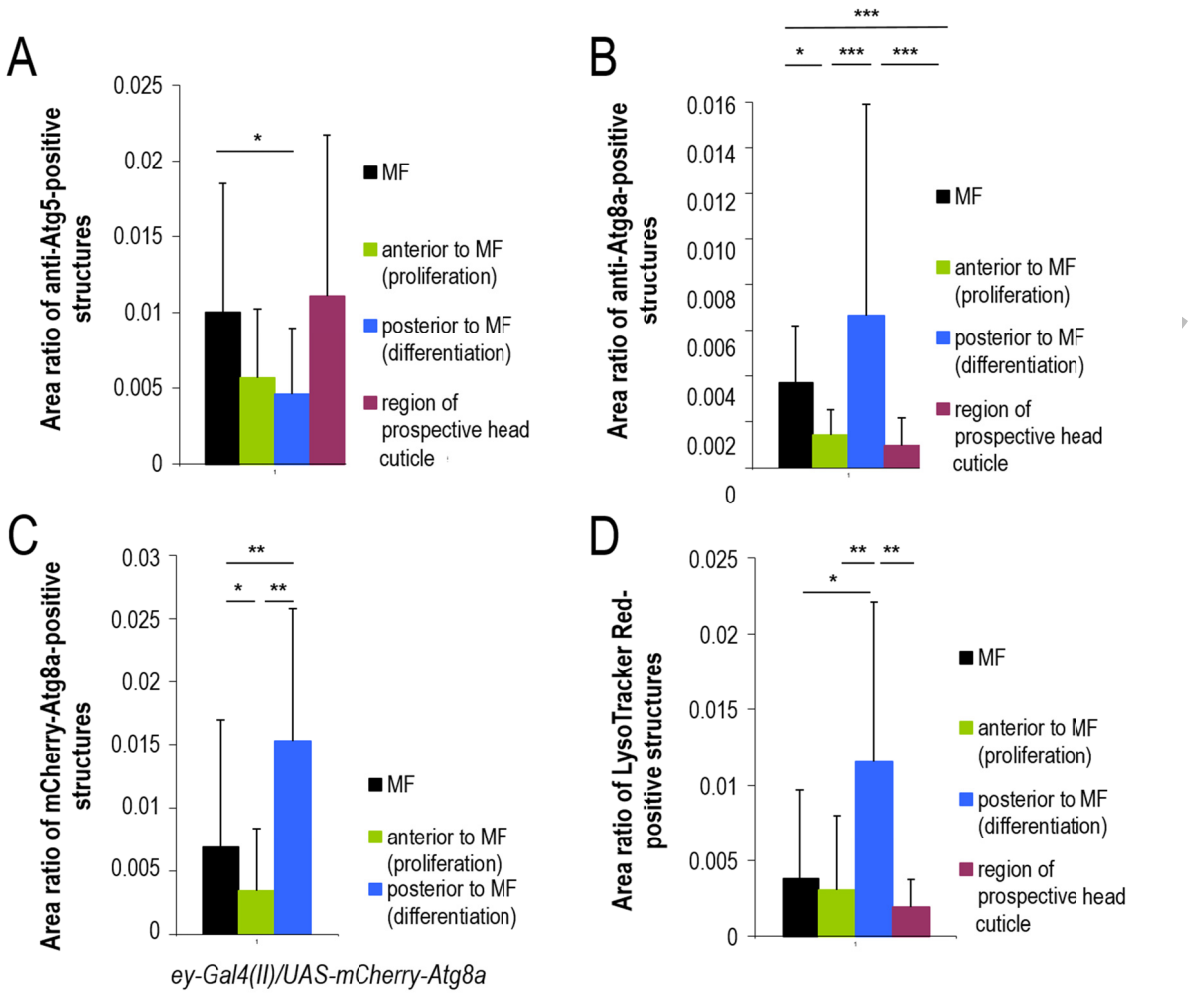

Figure S7. Relative amount of autophagic structures in different regions of the eye disc. (**A**) The amount of Atg5-specific foci in different parts of the eye disc. (**B**, **C**) Relative amount of Atg8a-specific structures in the main parts of the eye disc. Anti-Atg8a staining (**B**) and *mCherry-Atg8a* reporter expression (**C**) are specific to autophagic compartments. (**D**) Relative amount of LysoTracker Red-positive acidic structures in different parts of the eye disc. Samples were prepared from L3W larvae. According to the combined data, autophagic structures predominantly accumulate within the morphogenetic furrow (MF) and differentiation zone (DZ) (posterior to MF). Bars represent mean ±S.D.; *: $P<0.05$, **: $P<0.01$, ***: $P<0.001$, two-sample Student *t* test, *t* test for unequal variances or Mann-

Whitney U test. Genotype in (A, B, D): w^{1118} (C): *w*; ey-Gal4(II)/ UAS-mCherry-Atg8a.* The number of samples ranged between 4 and 16.

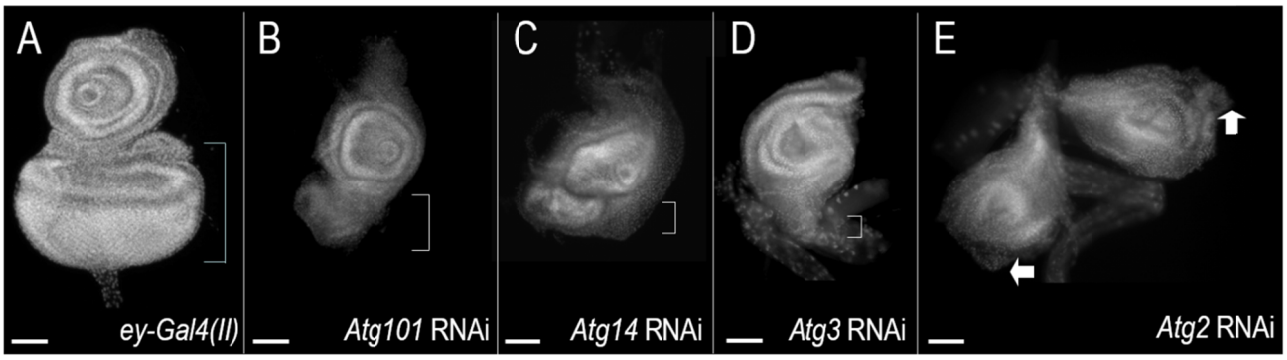

Figure S8. Silencing of *Atg* genes in the eye disc can severely compromise the shape and size of the organ. (**A**) Eye disc sample expressing *ey-Gal4(II)* only (control) shows normal morphology. (**B** to **E**) Morphological defects in *Atg* RNAi eye disc samples. Brackets indicate the area of the eye field. In panel **E**, white arrows show where the eye field should be located. Samples were prepared from L3W larvae, antenna part is up; bars: 50 µm. Genotypes: **A**, *w*; ey-Gal4(II)/+*; **B**, *w*; ey-Gal4(II), UAS-Dcr-2/Atg101* RNAi *(KK101226)*; **C**, *w*; ey-Gal4(II), UAS-Dcr-2/Atg14* RNAi; **D**, *w*; ey-Gal4(II)/+; Atg3* RNAi/+; **E**, *w*; ey-Gal4(II)/+; Atg2* RNAi *(HMS01198)/+*.

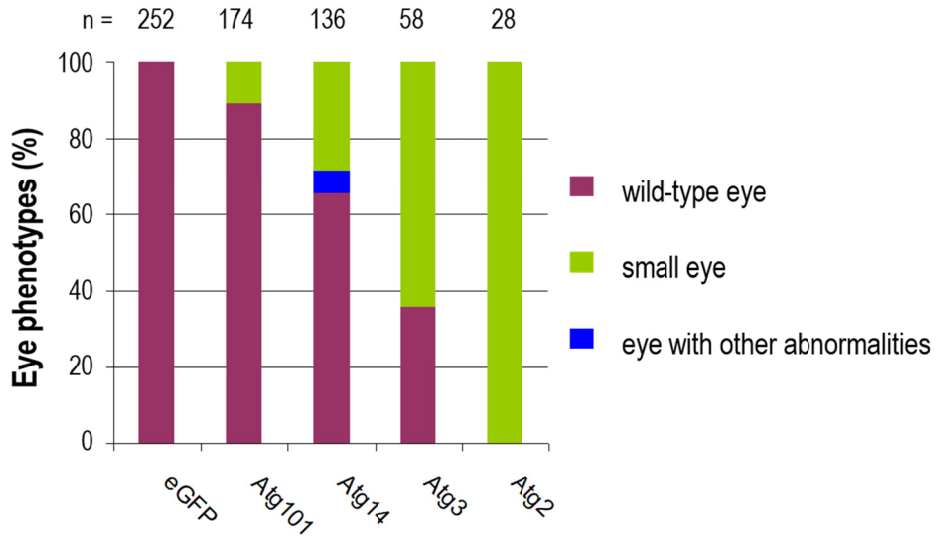

Figure S9. Silencing of *Atg* genes by the *so7-Gal4* driver can cause severe defects in eye development. *so7-Gal4* is active in almost the entire eye disc (also see **Fig. S5D**). eGFP = *eGFP*^{pVALIUM20shRNA}*(III)/so7-Gal4*. Atg101 = *Atg101* RNAi *(KK101226)/+; so7-Gal4/+*. Atg14 = *Atg14* RNAi */+; so7-Gal4/+* Atg3 = *Atg3* RNAi*/so7-Gal4*. Atg2 = *Atg2* RNAi *(HMS01198)/so7-Gal4*.

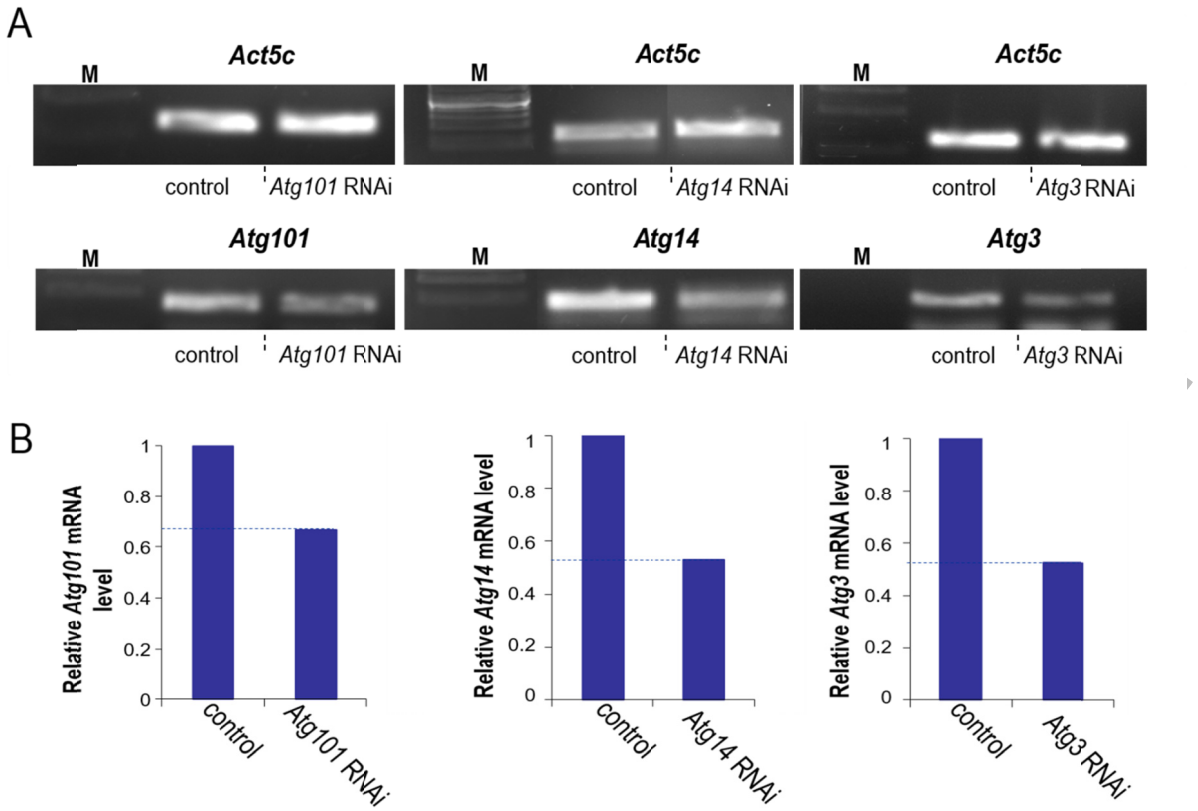

Figure S10. Effective *Atg* RNAi constructs causing defects in eye development significantly reduce the level of the corresponding *Atg* transcripts in the eye disc. (**A**) Semi-quantitative RT-PCR analysis showing that *Atg101*-, *Atg14*- and *Atg3*-specific RNAi constructs markedly (nearly by half) lower the amount of transcripts in the eye disc (bottom images). *Act5C/Actin5c* was used as an internal control (upper images). M, molecular weight marker. (**B**) Quantification of band intensities shown in panel **A**. Control for *Atg101* RNAi and *Atg14* RNAi = *w*; ey-Gal4(II)/+*. *Atg101* RNAi = *w*; ey-Gal4(II)/Atg101* RNAi *(KK101226)*. *Atg14* RNAi = *w*; ey-Gal4(II)/Atg14* RNAi. control for *Atg3* RNAi = *w*; ey-Gal4(III)/+*. *Atg3* RNAi = *w*; ey-Gal4(III)/Atg3* RNAi.

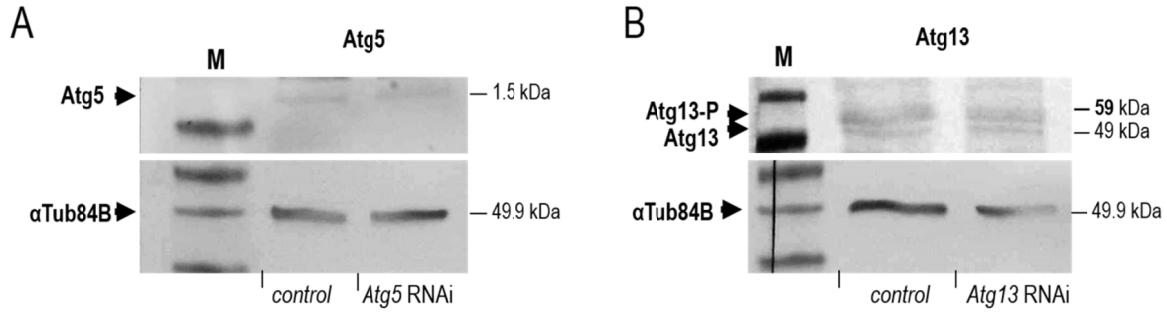

Figure S11. Ineffective *Atg* RNAi constructs causing no defect in eye development do not, or very weakly, alter the amount of the corresponding Atg proteins in the eye disc. Western blot analysis showing the relative amount of Atg5 (**A**) as well as Atg13 and Atg13-P (**B**) proteins, as compared with control samples. Eye-antennal discs were dissected from L3W larvae. αTub84B was used as an internal control. M, molecular mass marker. Genotypes: Control = *w*; ey-Gal4(II), UAS-Dcr-2/+*. *Atg5* RNAi = *w*; ey-Gal4(II), UAS-Dcr-2/+; Atg5* RNAi *(JF02703)/+*. *Atg13* RNAi = *w*; ey-Gal4(II), UAS-Dcr-2/Atg13* RNAi.

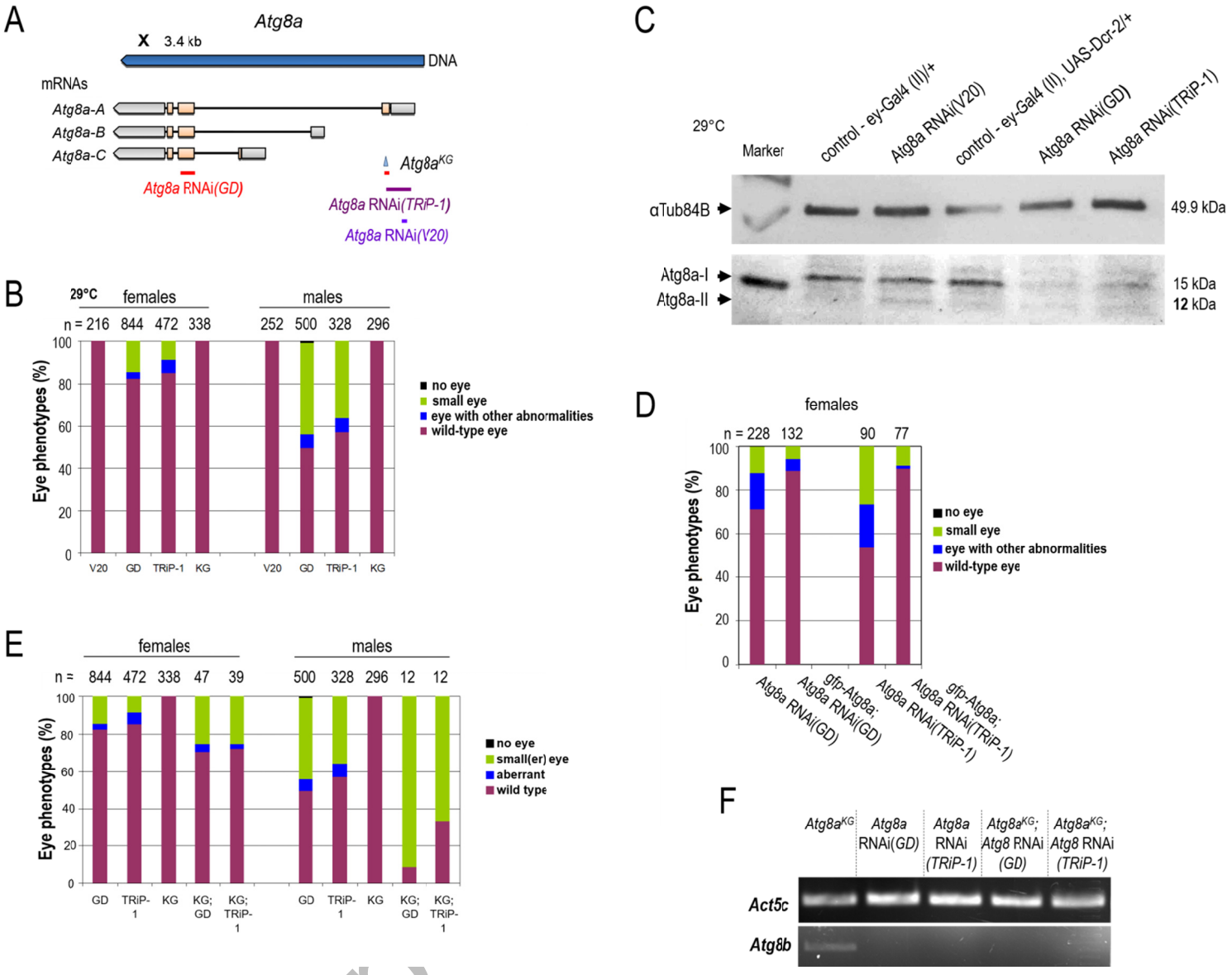

Figure S12. Silencing of *Atg8a* can lead to defects in eye development. (**A**) The transcript isoforms of *Atg8a* (*A*, *B* and *C*) and genomic sites that were targeted by RNAi constructs and the mutation *KG* (*Atg8a*^{KG03090}) are indicated. (**B**) The penetrance of eye phenotypes caused by RNAi treatment and the *KG* mutation. The RNAi construct *V20* and mutation *KG* are proved to be ineffective. (**C**) Levels of Atg8a isoforms (soluble I and PE-conjugated II) in control and RNAi-treated eye samples. (Ineffective) *V20* is not capable of reducing protein levels, whereas (effective) *GD* and *TRiP-1* markedly lowered their accumulation. (**D**) The eye

phenotypes of *Atg8a* RNAi*(GD)* and -*(TRiP-1)* animals can be partially rescued by a transgene containing a full copy of wild-type *Atg8a*. (**E**) Silencing of *Atg8a* by the RNAi construct *GD* and *TRiP-1* in the $Atg8a^{KG}$ mutant background causes a synergistic effect: *RNAi-KG* "double" inhibited animals display defects in eye development with a higher penetrance than the RNAi treatments alone. This may result from the activity of various splice variants (*A*, *B* and *C*) and/or paralogs (*Atg8a* and *Atg8b*). (**F**) Semi-qPCR analysis shows that *Atg8a* RNAi*(GD)* and *Atg8a* RNAi*(TRiP-1)* constructs also eliminate *Atg8b* transcripts. Note that *Atg8b* mRNA is absent in wild-type eye disc (**Fig. 4B**) but is upregulated in $Atg8a^{KG}$ mutant background. In the latter, *GD* and *TRiP-1* RNAi constructs trigger its degradation. *Act5C* was used as an internal control.

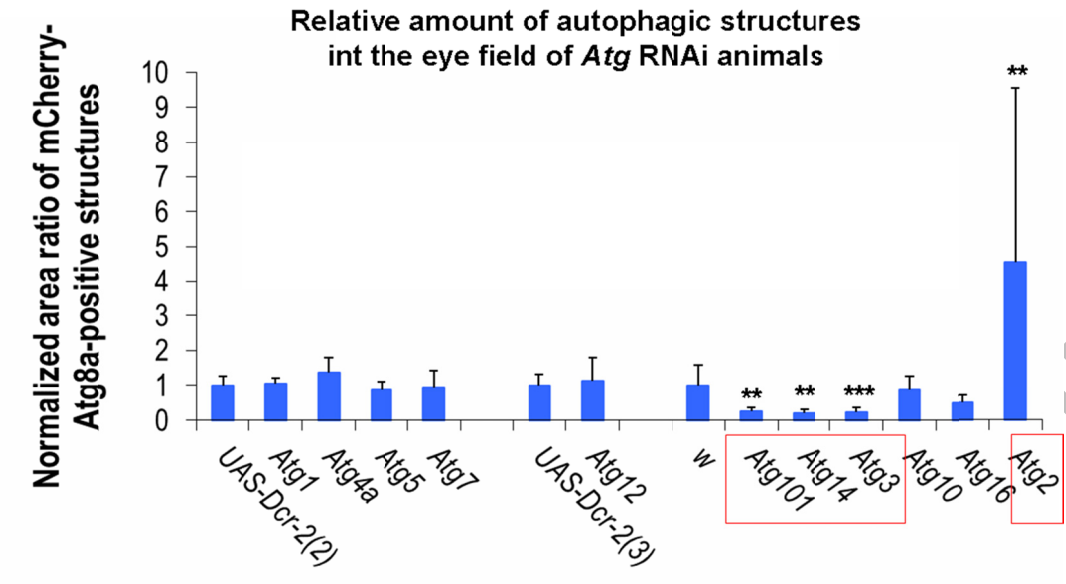

Figure S13. *Atg* RNAi constructs that do not alter eye development are incapable of reducing the relative amount of autophagic structures in this organ. Red frames indicate samples with significant changes. These *Atg* RNAi constructs lead to an obvious eye phenotype. The other constructs proved ineffective to reduce the amount of autophagic structures and to influence eye development. *w*, w^{1118} (control). Bars represent mean ±S.D., **: $P<0.01$, ***: $P<0.001$, two-sample Student t test, t test for unequal variances or Mann-Whitney U test. *Atg1*, *Atg4a*, *Atg5* and *Atg7* RNAi constructs were coexpressed with *UAS-Dcr-2(II)*. Expression of *UAS-Dcr-2(II)* alone served as a control. *Atg12* RNAi was coexpressed with *UAS-Dcr-2(III)*. Expression of *UAS-Dcr-2(III)* alone served as a control. For $Atg101^{KK101226}$-, *Atg14*, *Atg3*, *Atg10*, *Atg16*, and *Atg2* RNAi constructs, *w* (w^{1118}) served as control. In each cross, male genotype was *w*; ey-Gal4(II), UAS-mCherry-Atg8a*.

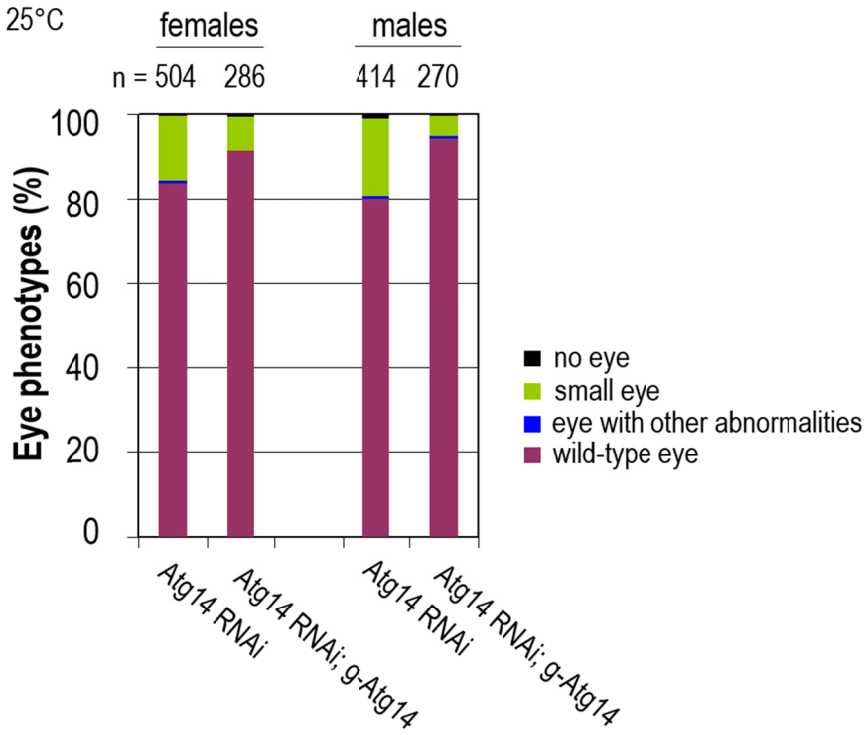

Figure S14. Normal eye development can be rescued in *Atg14* RNAi animals by a transgene containing the wild-type copy of *Atg14*. *g-Atg14* transgene contains a wild-type copy of *Atg14*. It can suppress the mutant eye phenotype by nearly half in *Atg14* RNAi animals. Genotypes: *Atg14* RNAi = *w*; ey-Gal4(II)/Atg14* RNAi. *Atg14* RNAi, *g-Atg14* = *w*; ey-Gal4(II)/Atg14* RNAi*; g-Atg14/+*.

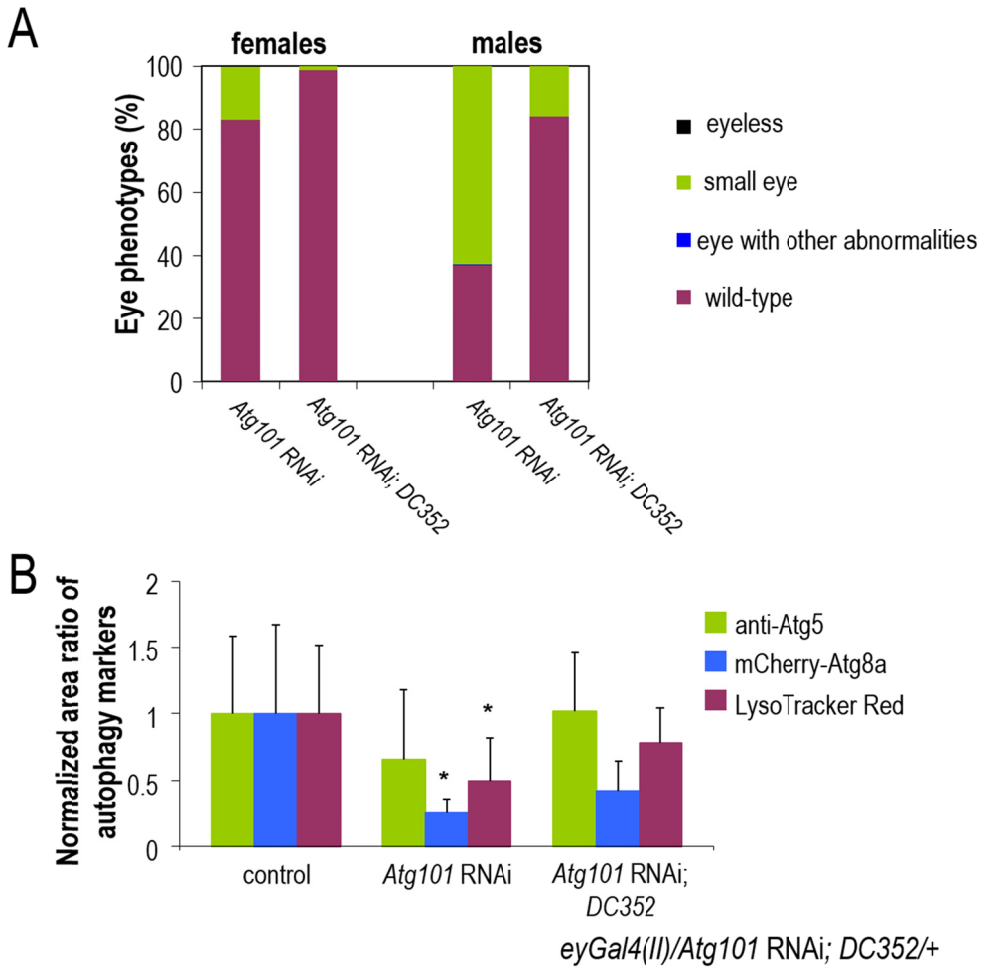

Figure S15. A duplication covering the *Atg101* locus can rescue normal eye development in *Atg101* RNAi animals. (**A**) Penetrance of the eye phenotype in *Atg101* RNAi females and males in control versus *DC352/+* genetic backgrounds. *DC532* is a transgenic duplication that covers *Atg101*. Note that the penetrance of the eye phenotype obtained from this experiment is lower than in those shown in **Fig. 3F** and **Table S1**. The reason for this difference stems from the fact that in the rescuing experiment *Dcr-2* was not overexpressed. (**B**) The presence of *DC352* largely rescues autophagic activity in *Atg101* RNAi eye disc samples. Bars represent mean ±S.D., *: $P<0.05$; two-sample Student t test or t test for unequal variances.

Genotypes: control=*w*; ey-Gal4(II)/+*. *Atg101* RNAi=*w*; ey-Gal4(II)/Atg101* RNAi *(KK101226)*. *Atg101* RNAi; DC352=*w*; ey-Gal4(II)/Atg101* RNAi *(KK101226); DC352/+*.

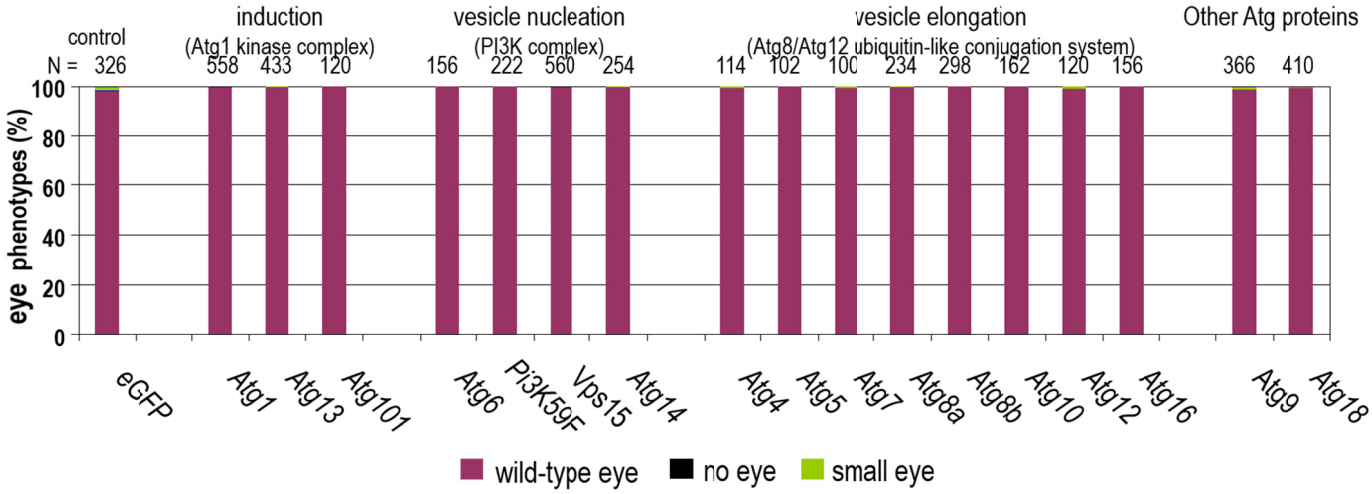

Figure S16. Silencing of *Atg* genes in the peripodial membrane only does not affect eye development. *Atg* genes and the number of samples examined are indicated. *RNAi* constructs were driven by *c311-Gal4* (see also in **Fig. S5E**). Knockdown of *eGFP* (control) leads to aberrant eye morphology at the largest extent (1.84%) among the samples. Data are also shown in **Table S2**.

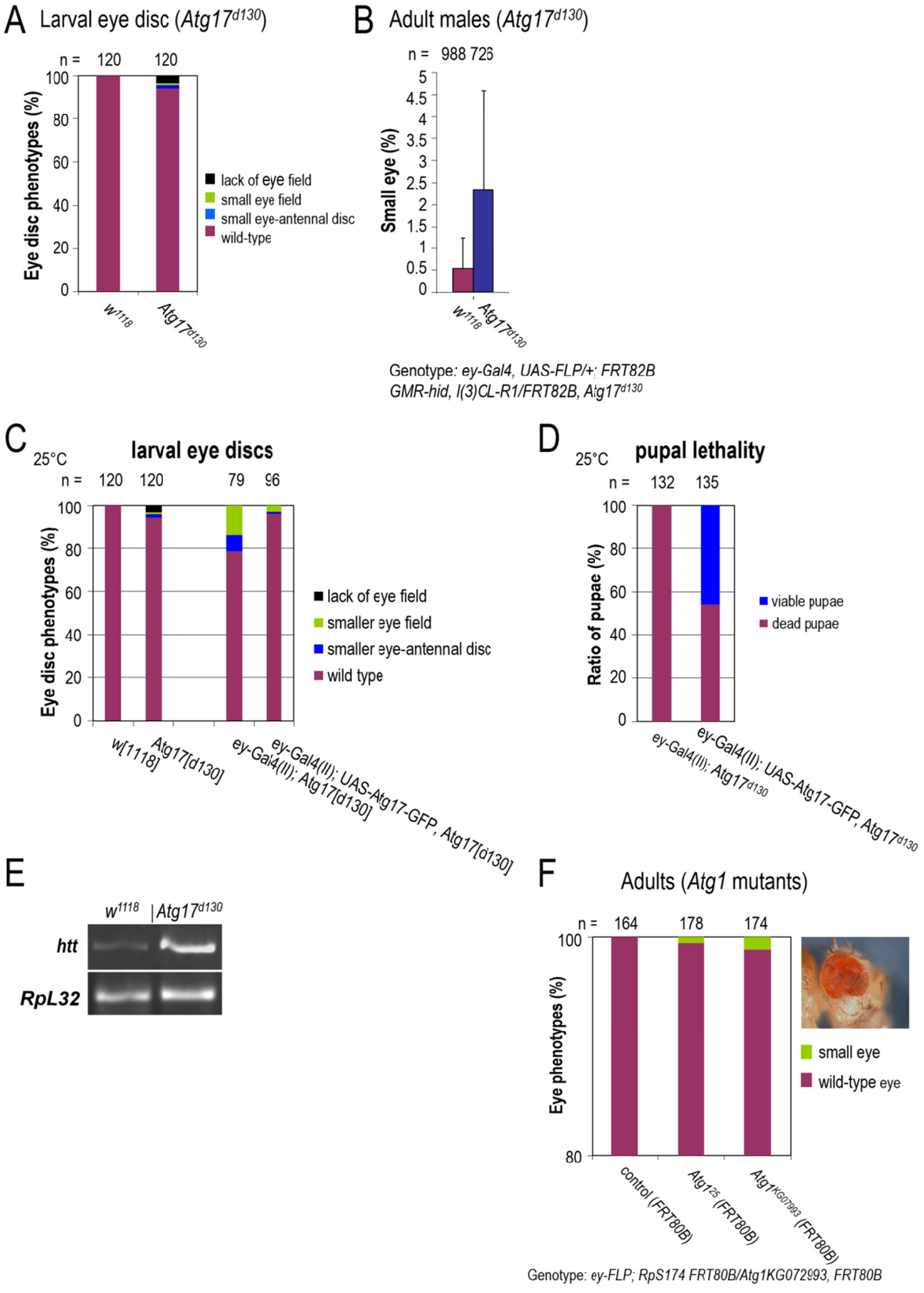
A Larval eye disc (Atg17d130)
n = 120 120
Eye disc phenotypes (%)
lack of eye field
small eye field
small eye-antennal disc
wild-type
w1118
Atg17d130
B Adult males (Atg17d130)
n = 988 726
Small eye (%)
Genotype: ey-Gal4, UAS-FLP/+; FRT82B GMR-hid, l(3)CL-R1/FRT82B, Atg17d130
C 25°C larval eye discs
n = 120 120 79 96
Eye disc phenotypes (%)
lack of eye field
smaller eye field
smaller eye-antennal disc
wild type
w[1118]
Atg17[d130]
ey-Gal4(II); Atg17[d130]
ey-Gal4(II); UAS-Atg17-GFP, Atg17[d130]
D 25°C pupal lethality
n = 132 135
Ratio of pupae (%)
viable pupae
dead pupae
ey-Gal4(II); Atg17d130
ey-Gal4(II); UAS-Atg17-GFP, Atg17d130
E
w1118
Atg17d130
htt
RpL32
F Adults (Atg1 mutants)
n = 164 178 174
Eye phenotypes (%)
small eye
wild-type eye
control (FRT80B)
Atg125 (FRT80B)
Atg1KG07993 (FRT80B)
Genotype: ey-FLP; RpS174 FRT80B/Atg1KG07293, FRT80B

Figure S17. Mutational inactivation of *Atg1* and *Atg17* can interfere with eye development. (**A**) Loss-of-function (lf) mutation in *Atg17* compromises eye development with only a low penetrance. Eye disc samples were prepared from L3W larvae. (**B**) Penetrance of the small eye phenotype in *Atg17* mutant adult males. Bars represent mean ±S.D., ***: $P<0.005$; two-sample Student *t* test. (**C**) The eye disc morphology phenotype of $Atg17^{d130}$ mutant larvae can be rescued by a transgene containing the wild-type copy of *Atg17*. (**D**) The same transgene (*Atg17-GFP*) significantly suppresses the lethality of $Atg17^{d130}$ mutant pupae. Nearly half of the transgenic animals remains alive. (**E**) In $Atg17^{d130}$ mutant animals, the *htt* (*huntingtin*) gene becomes overexpressed, as compared with the control background. *htt* encodes a scaffold protein for selective autophagy. Atg17 also acts as a scaffold to recruit other Atg proteins to the phagophore assembly site. *RpL32* was used as an internal control (**F**) Penetrance of the small eye phenotype in *Atg1* lf mutant adult animals. The image shows a small eye. In panels **A** to **F**, the number of samples assayed is indicated. Genotypes: control in panel (B): *w*; ey-Gal4, UAS-FLP/+; FRT82B, GMR-hid, l(3)CL-R^{1}/ FRT82B*. $Atg17^{d130}$ = *w*;ey-Gal4, UAS-FLP/+; FRT82B, GMR-hid, l(3)CL-R^{1}/ FRT82B, $Atg17^{d130}$*. Control in panels (**C** and **D**): *ey-Gal4(II); $Atg17^{d130}$ = ey-Gal4 (II)/+; FRT82B, $Atg17^{d130}$. ey-Gal4(II); $Atg17^{d130}$, UAS-Atg17-GFP = ey-Gal4 (II)/+; FRT82B, $Atg17^{d130}$/$Atg17^{d130}$, UAS-Atg17-GFP*. Control in panel (**F**): *ey-FLP; $RpS17^{4}$, w+, FRT80B/FRT80B*. $Atg1^{25}$ = *ey-FLP; $RpS17^{4}$, w+, FRT80B/$Atg1^{25}$, FRT80B*. $Atg1^{KG07993}$ = *ey-FLP; $RpS17^{4}$, w+, FRT80B/$Atg1^{KG07993}$, FRT80B*.

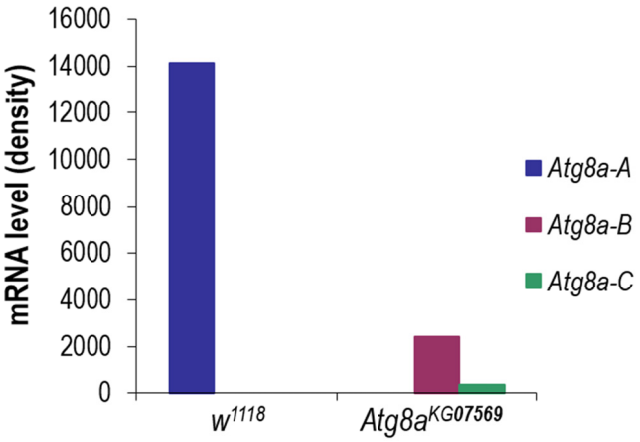

Figure S18. Relative amounts of the different *Atg8a* mRNA isoforms in wild-type (w^{1118}) versus an *Atg8a-A* mutant background. Quantification of band intensities shown in **Fig. 4A'** and **B**. In the control sample, only *Atg8a-A* (blue bar) is active. In the *Atg8a-A* mutant background, *Atg8a-A* transcript disappears, *Atg8a-B* mRNA (purple bar) becomes abundant, while *Atg8a-C* (green bar) is slightly activated. *Act5C* was used as an internal control.

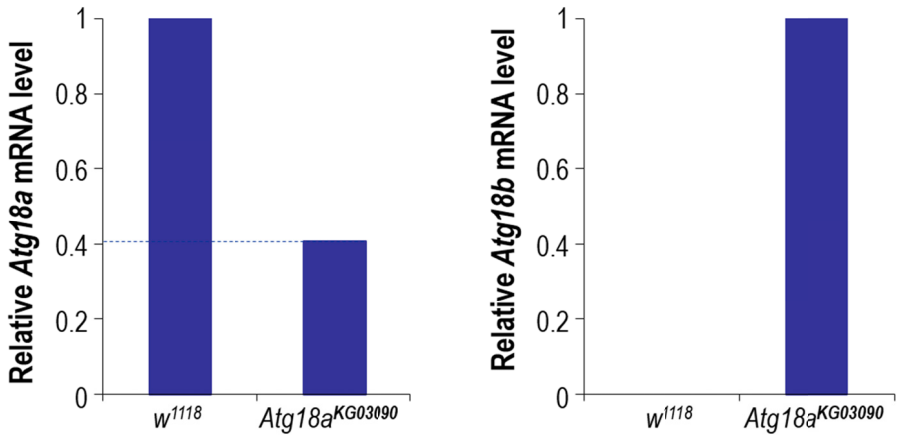

Figure S19. Relative amounts of *Atg18a* and *Atg18b* transcripts in wild-type (w^{1118}) versus an *Atg18a*-specific mutant background. Quantification of band intensities shown in **Fig. 4E**. Left panel: *Atg18a* mRNA levels are highly reduced in mutant samples, as compared with control (w^{1118}). Right panel: *Atg18b* mRNA is not detectable in control samples, but is readily visible in mutant samples. $Atg18a^{KG03090}$ = $Atg18a^{KG03090}$/*Atg18a Df(3L)Exel6112*. *Act5C* was used as an internal control.

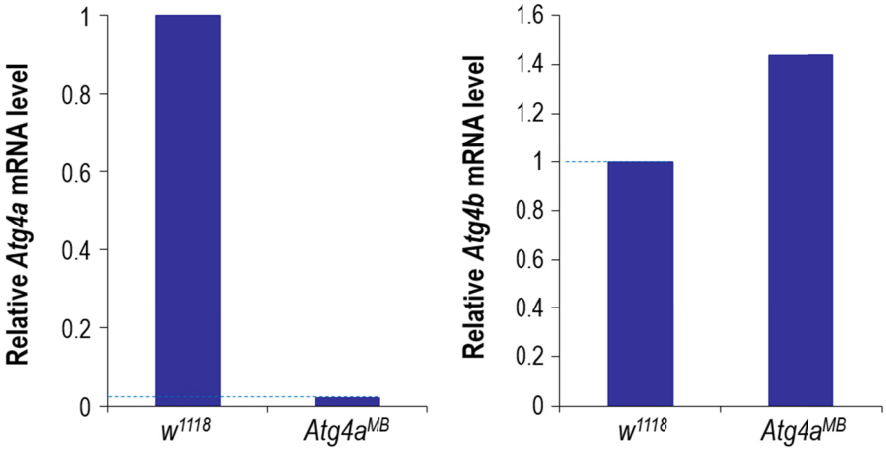

Figure S20. Relative amounts of *Atg4a* and *Atg4b* mRNAs in control versus an *Atg4a* lf mutant background. Quantification of band intensities shown in **Fig. 4F**. Left panel: *Atg4a* mRNA levels are highly reduced in mutant samples, as compared with controls. Right panel: *Atg4b* is expressed at higher levels in *Atg4a* mutant samples than in control ones. *Act5C* was used as an internal control. Control: w^{1118}. $Atg4a^{MB}$: $Atg4a^{MB03551}$.

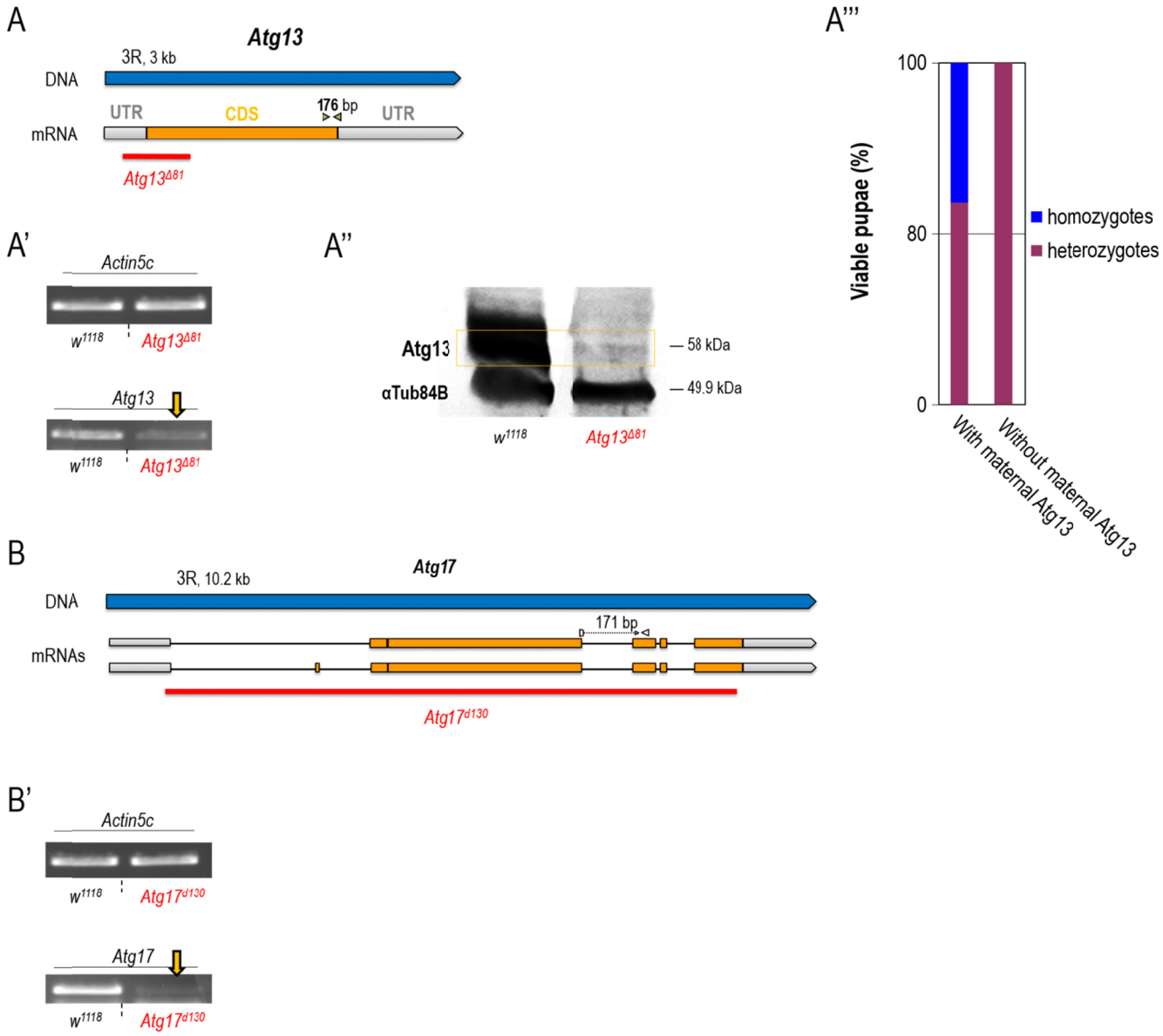

Figure S21. Presence of *Atg13*- and *Atg17*-specific transcripts and proteins in *Atg13* and *Atg17* mutant eye disc samples, respectively. (**A**) The structure of *Atg13* gene. (**A'**) Presence of *Atg13* transcripts in $Atg13^{\Delta 81}$ mutant samples (yellow arrow). (**A''**) Anti-Atg13 antibody staining reveals the presence of Atg13 proteins in $Atg13^{\Delta 81}$ mutant samples. (**A'''**) Without maternally contributed *Atg13*, homozygous mutants die prior to the L3W stage. ovo^{D1} mutation eliminates the maternal *Atg13* products (dominant female sterile technique). Left column shows the progeny of the following cross: *hsFLP; FRT82B,* $Atg13^{\Delta 81}$*/TM6B* x

FRT82B, Atg13$^{\Delta 81}$/TM6B. Right column displays progeny of the following cross: *hsFLP; FRT82B, Atg13$^{\Delta 81}$/FRT82B, ovo^{D1}* x *FRT82B, Atg13$^{\Delta 81}$/TM6B* heat shock (2 h, 2 times at 37°C during larval stages). (**B**) The structure of *Atg17* gene. In panels **A** and **B**, both coding region (DNA) and transcript (mRNA) are shown. Yellow boxes indicate coding exonic sequences, connecting lines correspond to introns, grey boxes refer to UTRs. Red lines show the extend of deletions examined, primers used for semi-quantitative RT-PCR are also indicated. (**B'**) The presence of *Atg17* transcripts (yellow arrow) in *Atg17* null mutant samples. In panels **A'** and **B'**, *Act5C* was used as an internal control. In panel **A''**, αTub84B was used as an internal control.

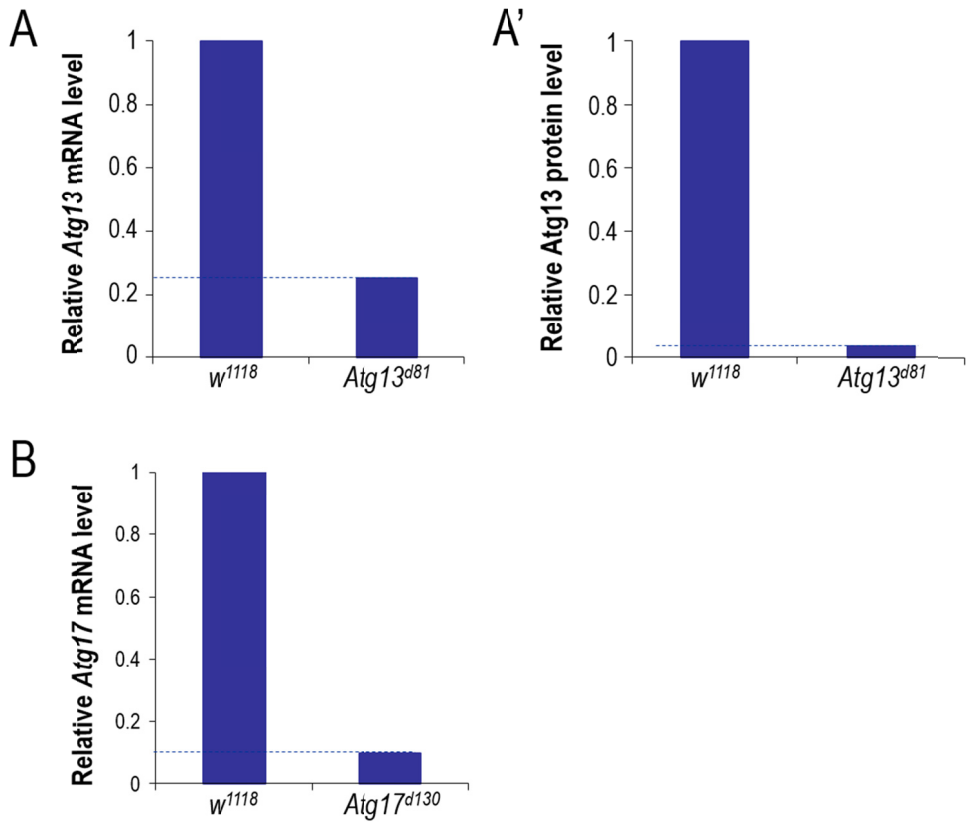

Figure S22. Relative amounts of *Atg13*- and *Atg17*-specific gene products in *Atg13* and *Atg17* mutant eye disc samples, respectively. Quantification of band intensities shown in **Fig. S21A'**, **A''**, **B'**. (**A**) *Atg13* transcript levels are lowered in *Atg13* lf mutant samples, as compared with controls. (**A'**) Low, but still detectable, amount of Atg13 proteins in *Atg13* lf mutant samples. (**B**) Relative *Atg17*-specific mRNA levels in control versus *Atg17* null mutant samples. *Act5C* was used as an internal control.

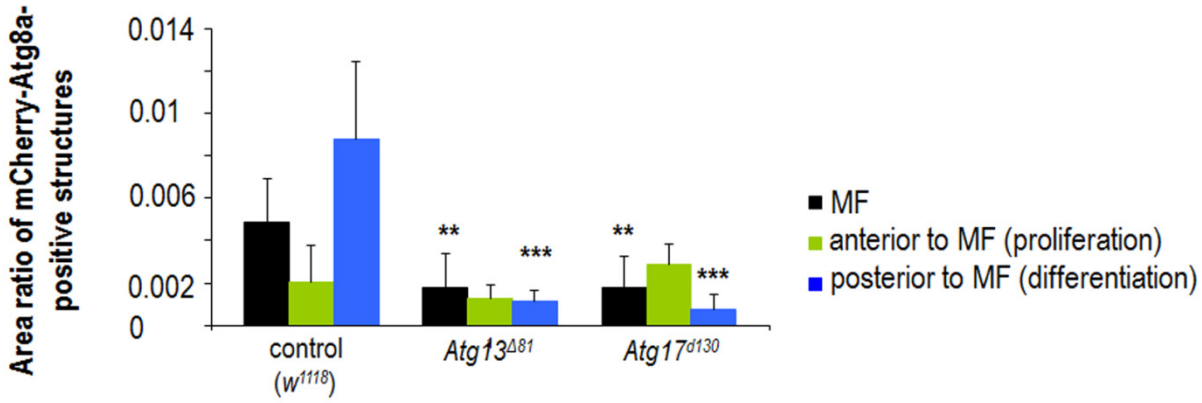

Figure S23. Relative amount of mCherry-Atg8a-positive autophagic structures in *Atg13* and *Atg17* mutant eye disc samples. The amount of autophagic structures decreased significantly, but was not eliminated completely, in the mutant samples. Bars represent mean ±S.D., **: $P<0.01$, **: $P<0.001$, two-sample Student t test or t test for unequal variances. The mutant alleles represent large deletions, thereby considered as genetic null mutations.

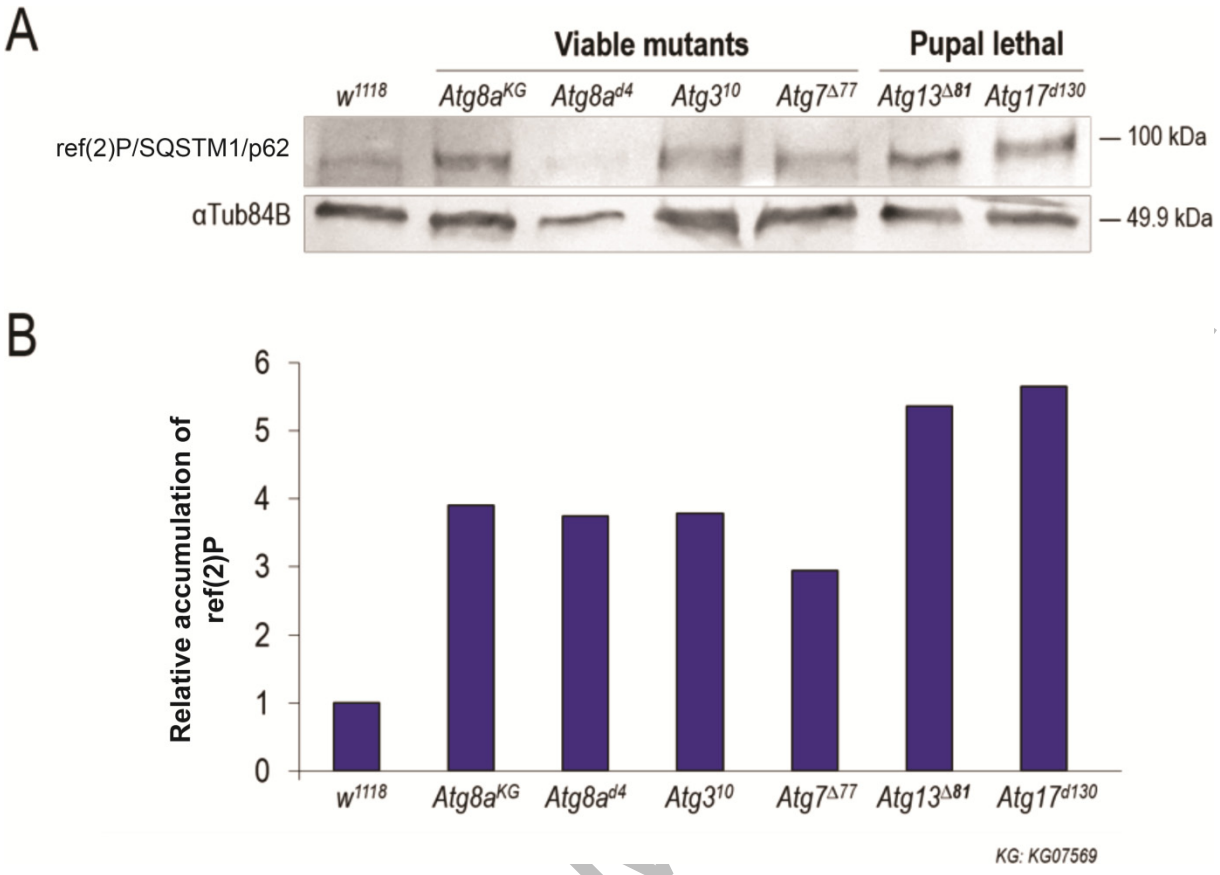

Figure S24. ref(2)P (also termed SQSTM1/p62 in mammals) protein levels vary among different *Atg* mutant eye disc samples. (**A**) Western blot analysis showing relative amounts of ref(2)P/SQSTM1/p62 proteins in *Atg* mutant samples. ref(2)P/SQSTM1/p62 served as a substrate for autophagy (*i.e.* its amount is inversely proportional with autophagic activity). αTub84B was used as an internal control. Control: w^{1118}. Pupal lethal homozygous mutants are derived from heterozygous parents. (**B**) Quantification of band intensities shown in panel **A**. The amount of ref(2)P/SQSTM1/p62 is highest in mutants exhibiting most severe phenotypic effects, $Atg13^{\Delta 81}$ and $Atg17^{d130}$ (pupal lethal). Thus, the other *Atg* mutants (viable) examined cannot be considered as complete autophagy-defective samples (they display residual activities).

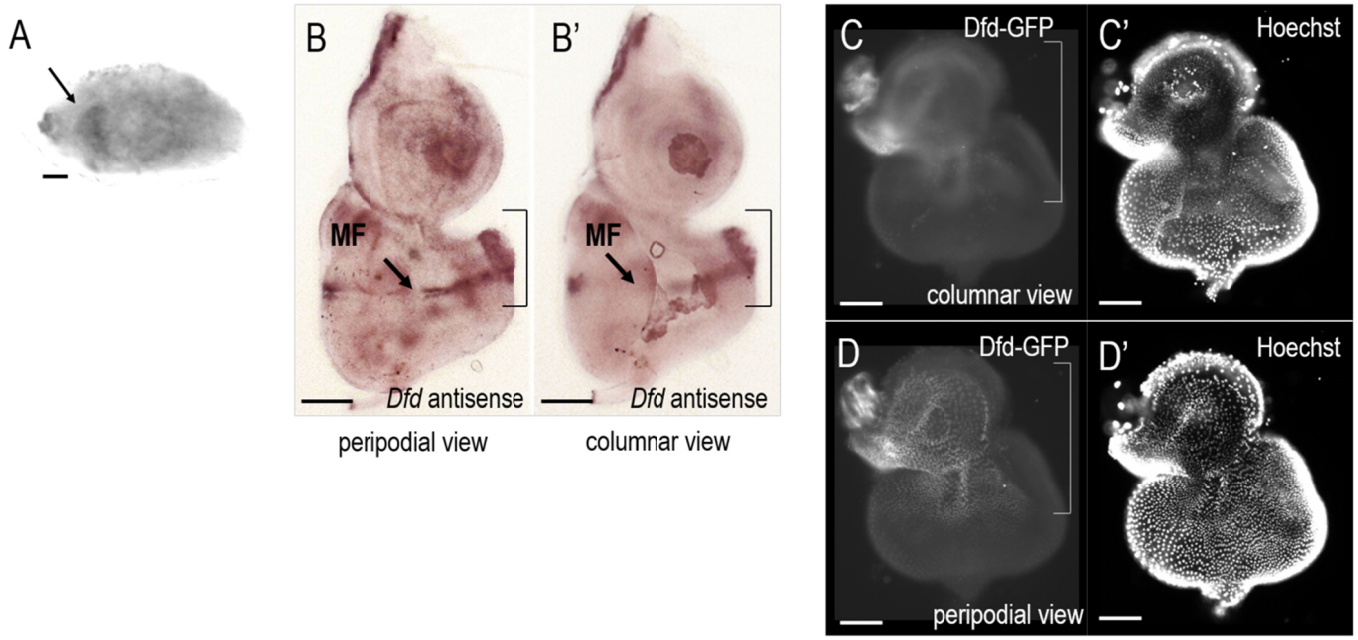

Figure S25. *Dfd* is expressed in the peripodial membrane. (**A)** *Dfd* expression in a 9-h embryo. The arrow points to the *Dfd*-positive area. (**B**, **B'**) Expression of *Dfd* in the eye disc. Brackets indicate the area where *Dfd* mRNA is detectable. (**C**, **D)** Dfd-GFP protein accumulates only in the peripodial membrane (sharp signs can only be seen in the nuclei of panel **D**). (**C'**, **D'**) Hoechst staining indicates nuclei, antenna part is up. Bars: 50 µm in each image. Genotype (**A**, **B**, **B'**): w^{1118}; (**C** to **D'**): *Dfd-GFP*.

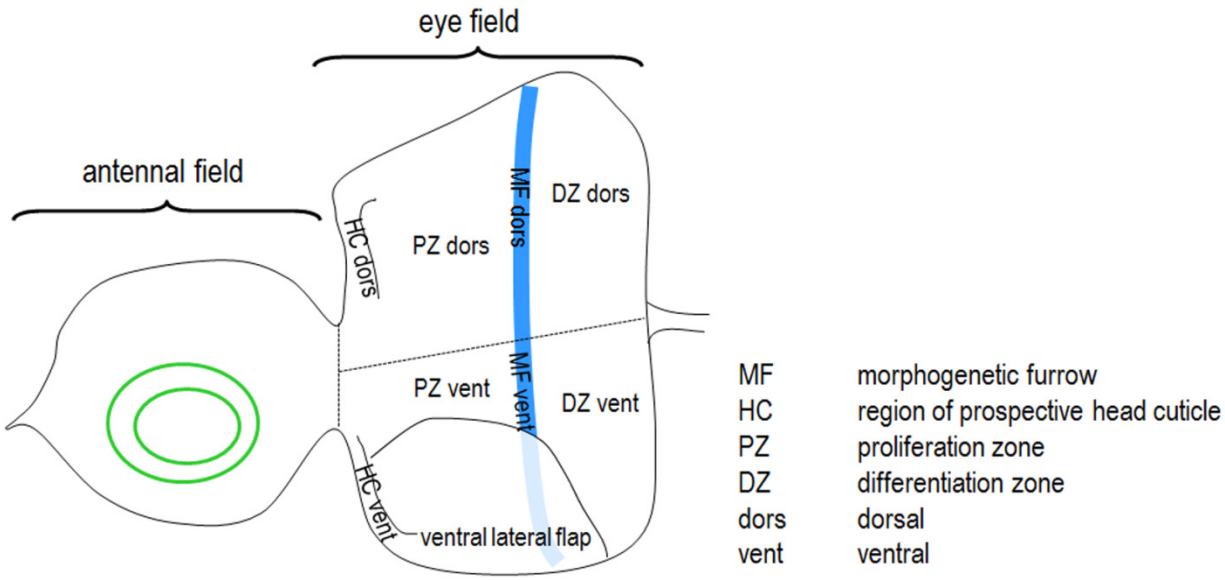

Figure S26. The eye field is divided into 9 parts (subfields) for analyzing the expression of *Atg8a-A* reporters (see on Fig. 6G'''). The following subregions were analyzed: 1, dorsal differentiation zone (DZ dors); 2, ventral differentiation zone (DZ vent); 3, dorsal morphogenetic furrow (MF dors.); 4, ventral morphogenetic furrow (MF vent); 5, dorsal proliferation zone (PZ dors); 6, ventral proliferation zone (PZ vent); 7, dorsal prospective head cuticle (HC dors); 8, ventral prospective head cuticle (HC vent); 9, ventral lateral flap.

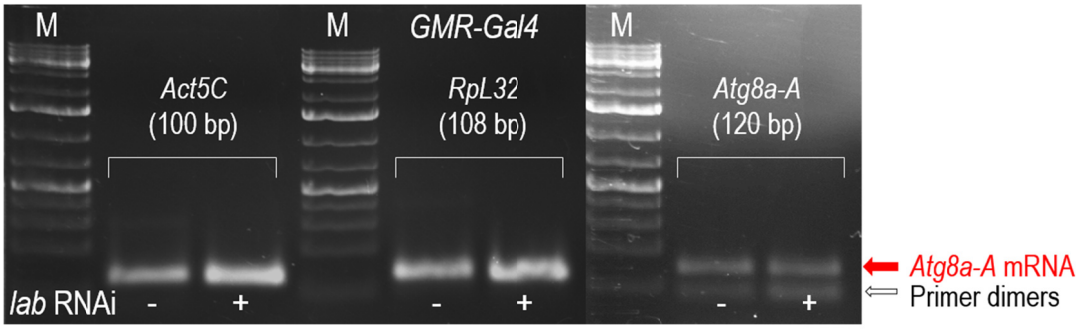

Figure S27. The lab (labial) protein does not influence *Atg8a-A* transcription in the differentiation zone. Semi-quantitative RT-PCR on control versus *lab* RNAi eye disc samples displays no significant difference between transcript levels. The construct is driven by *GMR-Gal4* that is active only in the DZ (also see **Fig. S4A**). *Act5C* and *RpL32* were used as internal controls. M, molecule size marker. Eye-antennal disc samples were dissected from L3W larvae. Control: *w*; GMR-Gal4/+, UAS-Dcr-2/+*. *lab* RNAi: *w*; GMR-Gal4/lab* RNAi*, UAS-Dcr-2/+*.

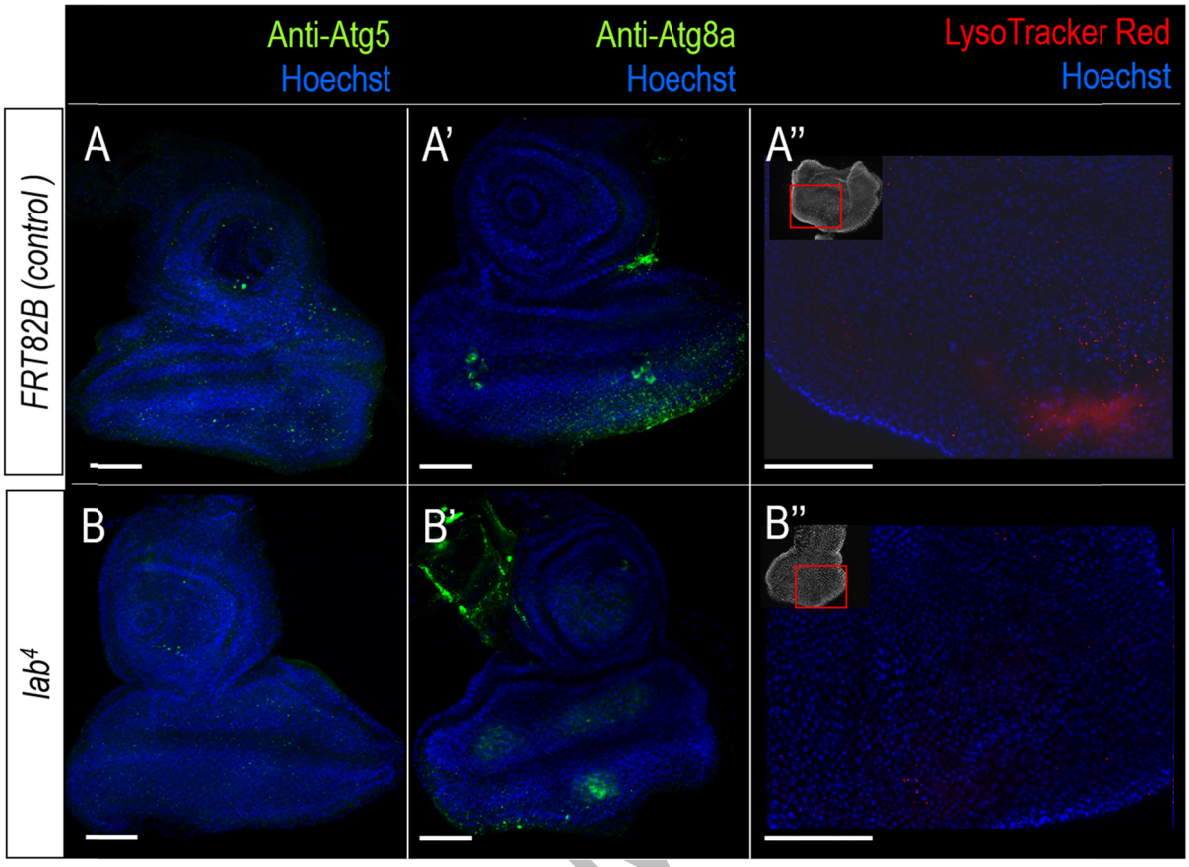

Figure S28. Mutational inactivation of *lab* leads to reduced autophagic activity in the differentiation zone. (**A**) Anti-Atg5 antibody labels early autophagic structures in the eye disc of a *FRT82B* control animal. (**A'**) Anti-Atg8a staining reveals autophagosomes and autolysosomes in the eye disc of a *FRT82B* animal. (**A''**) LysoTracker Red-positive autophagic structures accumulate mainly in the differentiation zone (DZ). (**B** to **B''**) In lab^4 mutant samples, the number of autophagic structures decreases significantly in the DZ, as compared with control samples. Quantification of data is shown in **Fig. 8F**. At the upper left corner in panels **A'''** and **B'''**, the entire eye-antenna imaginal disc is visible, and a red rectangle shows the enlarged area. Eye disc samples were dissected from L3W larvae; bars: 50 µm. FRT82B = *w*, ey-FLP*; *FRT82B, l(3)cl-*$R3^1$*/FRT82B*. lab^4 = *ey-FLP; FRT82B, l(3)cl-*$R3^1$*/FRT82B*, lab^4.

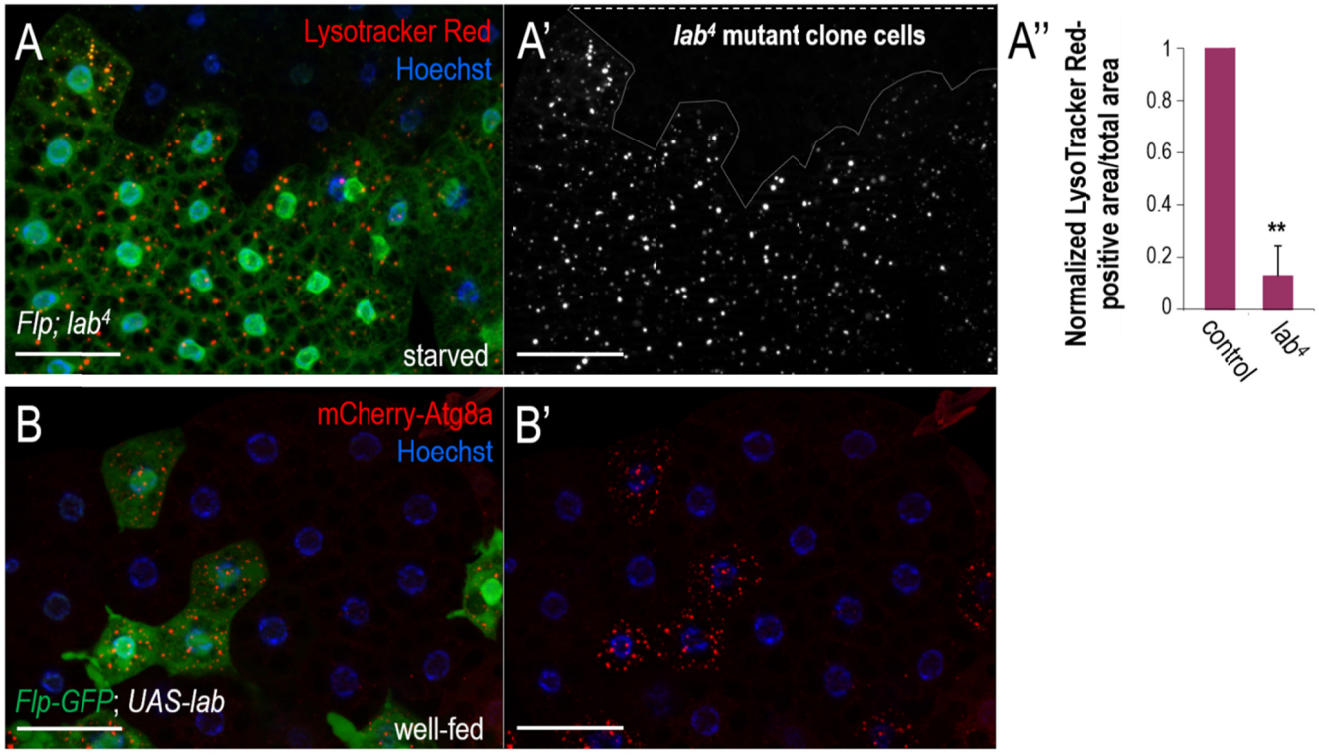

Figure S29. lab activates autophagy in the larval fat body. (**A**) Clonal inhibition of *lab* (non-green cells) causes elimination of autophagic (LysoTracker Red-positive) structures in the affected cells under conditions of starvation. Non-green cells are defective for *lab*. Green cells serve as controls. (**A'**) The corresponding uncolored figure. (**A''**) Quantification of autophagic structures in control versus lab^4 mutant fat body cells. Bars represent mean ±S.D., **: $P<0.01$, paired t test. (**B**, **B'**) Clonal hyperactivation of *lab* in the larval fat body induces the amount of mCherry-Atg8a-positve autophagic structures (red foci) in the affected cells under well-fed conditions. Hoechst staining indicates nuclei, bars: 50 µm. Fat body samples were prepared from 88 to 92-h L3F-stage larvae. Temperatures were 25°C. Genotypes: in panel (**A**): non-green cells: *w*, hsFLP; FRT82B,* lab^4. green, control cells: *w*, hsFLP; FRT82B, Ubi-GFP* or *w*, hsFLP; FRT82B, Ubi-GFP / FRT82B,* lab^4. In panel (B) green cells: *w*, hsFlp; UAS-lab/+; ActGal4, UAS-nlsGFP, r4-mCherry-Atg8a*. Non-green, control cells: *w*, hsFlp; UAS-lab/+; Act<CD2<Gal4, UAS-nlsGFP, r4-mCherry-Atg8a*.

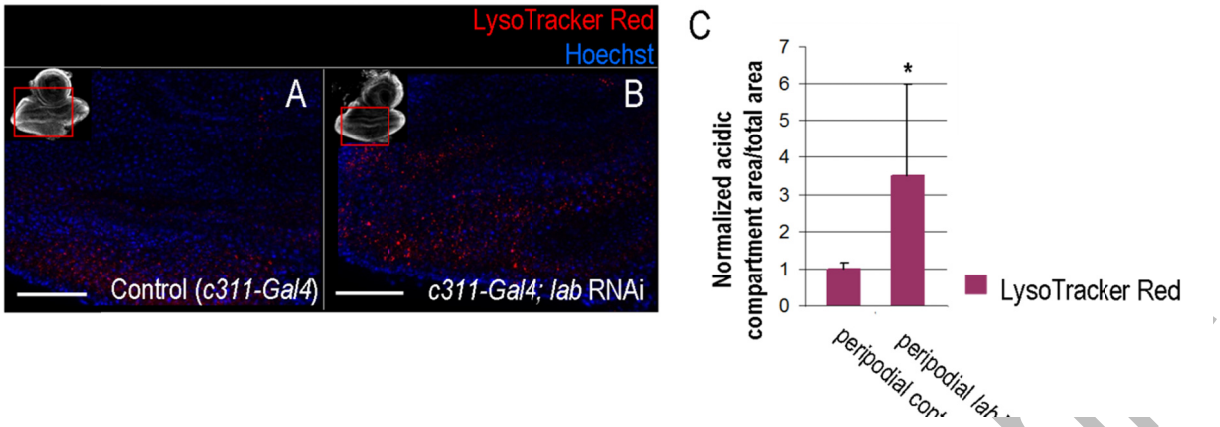

Figure S30. Depletion of *lab* in the peripodial membrane increases the amount of acidic compartments in the eye disc. (**A**) LysoTracker Red staining of a *c311-Gal4/UAS-Dcr-2* eye disc, serving as a control for *lab* RNAi. Red foci indicate lysosomes, autolysosomes and multivesicular bodies (acidic compartments). (**B**) LysoTracker Red staining of *lab* RNAi/+; *c311-Gal4/UAS-Dcr-2* eye disc shows an elevated amount of acidic compartments. In panels **A** and **B**, the antenna part is up. At the upper left corner, the entire eye-antenna imaginal disc is shown, and red rectangle indicates the enlarged area. Eye disc samples were dissected from L3W larvae; bars: 50 µm. (**C**) Quantification of autophagic structures in eye disc samples depleted for *lab* only in the peripodial membrane. The ratio of LysoTracker Red-positive structures and the entire eye disc is on average, data were normalized to controls. Bars represent mean ±S.D., *: $P<0.05$, t test for unequal variances.

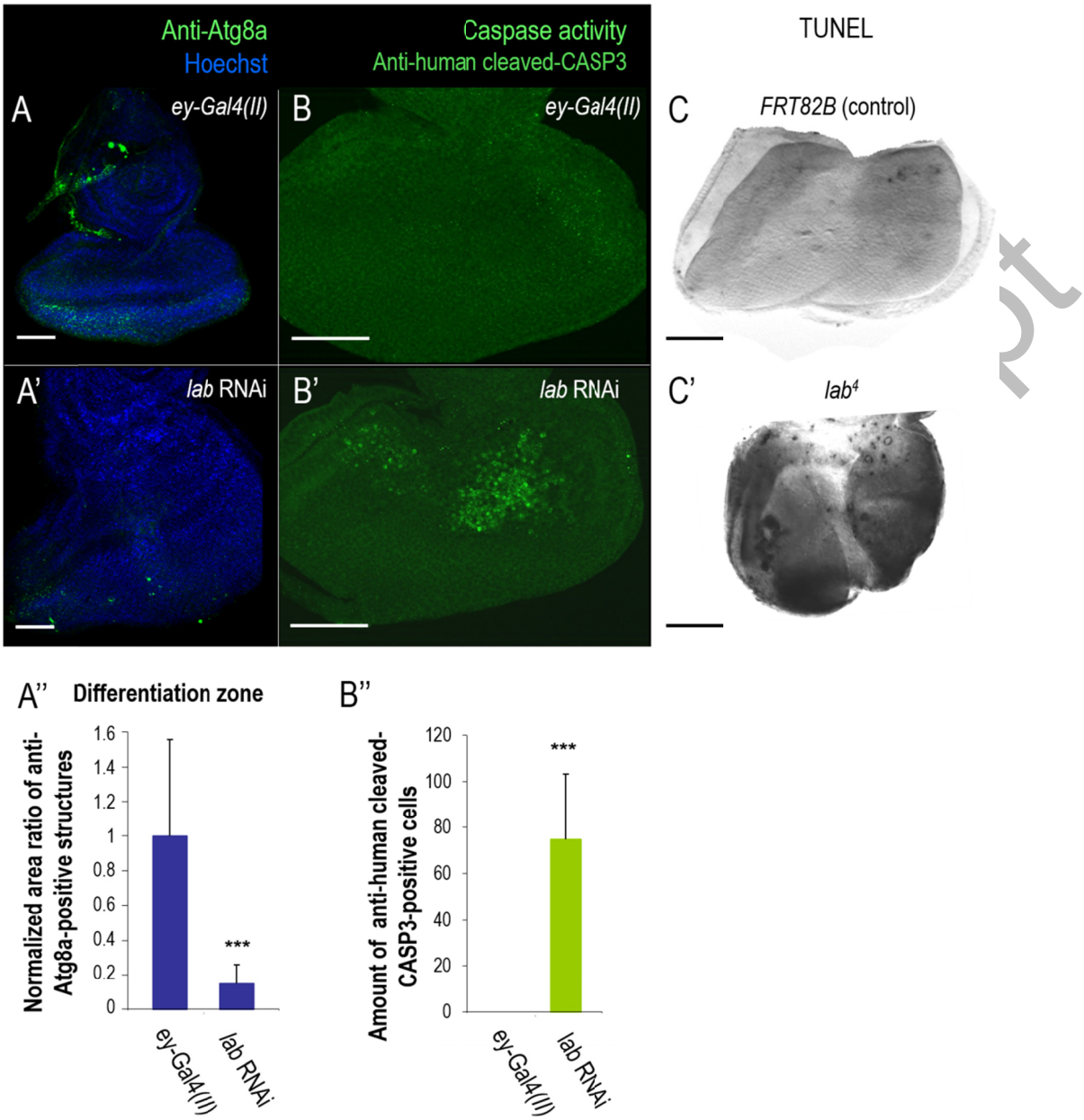

Figure S31. Lab deficiency in the eye disc decreases the amount of Atg8a-positive autophagic structures, and increases the number of cells with apoptotic features. (**A**, **A'**) Anti-Atg8a staining indicates autophagic structures (green foci) in control versus *lab* RNAi samples. *lab* RNAi construct is driven by *ey-Gal4(II), UAS-Dcr-2(II)* (**A''**) Quantification of autophagic structures in control [*ey-Gal4(II)*] versus *ey-Gal4(II); lab* RNAi samples. (**B**, **B'**) Human cleaved-CASP3 antibody staining in control and *lab* RNAi samples. Green foci indicate cells, which show increased caspase activity hence probably undergo apoptosis. (**B''**)

Quantification of cells which show increased caspase activity in samples indicated. (**C**, **C'**) TUNEL staining in control versus *lab* mutant samples. In panels **A''** and **B''**, bars represent mean ±S.D., ***: $P<0.005$; Mann-Whitney U-test. FRT82B = *w*, ey-FLP*; *FRT82B, l(3)cl-R3^{1}/FRT82B*. *lab^{4} = ey-FLP; FRT82B, l(3)cl-R3^{1}/FRT82B*, *lab^{4}*.